

First-principles and Continuum Modeling of  
Charge Transport in Li-O<sub>2</sub> Batteries

by

Maxwell D. Radin

A dissertation submitted in partial fulfillment  
of the requirements for the degree of  
Doctor of Philosophy  
(Physics)  
in the University of Michigan  
2014

Doctoral Committee:

Assistant Professor Donald J. Siegel, Co-Chair  
Professor Çagliyan Kurdak, Co-Chair  
Professor David W. Gidley  
Professor Sharon C. Glotzer  
Assistant Professor Charles W. Monroe

© Maxwell D. Radin 2014

In memory of my  
grandfather, Norman Radin.

## **Acknowledgements**

First, I am deeply grateful to my advisor, Don Siegel, for his invaluable mentorship in not just matters of science, but also how to be an effective scientist. I am also deeply grateful for Chuck Monroe's pedagogy and insights regarding transport theory, as well as the appreciation he has instilled in me for the elegant solutions to elegant problems and the meaning of the scientific method. I additionally thank Professors Çagliyan Kurdak, Dave Gidley, and Sharon Glotzer for their valuable advice and service on my committee. I have also been fortunate to receive mentorship from Drs. Brandon Wood and Tadashi Ogitsu, a partnership spawned through the 2012 Lawrence Livermore National Laboratory Computational Chemistry and Materials Science Summer Institute. I am deeply grateful for the support I received 'off the court' from Ian Tran, Qi Yang, Mona Wood, Lei Zhang, Dennis Larkin, and Bill Burnham, and last but certainly not least, my mother Ginny, father Lon, and brother Jesse.

This work was supported by Robert Bosch LLC through the Bosch Energy Research Network Grant no. 19.04.US11; the U.S. Department Energy's U.S.-China Clean Energy Research Center for Clean Vehicles, grant no. DE-PI0000012. P.; and the Joint Center for Energy Storage Research, an Energy Innovation Hub funded by the U.S. Department of Energy, Office of Science, Basic Energy Sciences.

# Table of Contents

<b>Dedication .....</b>	<b>ii</b>
<b>Acknowledgements .....</b>	<b>iii</b>
<b>List of Figures .....</b>	<b>vii</b>
<b>List of Tables .....</b>	<b>ix</b>
<b>List of Appendices .....</b>	<b>x</b>
<b>Abstract .....</b>	<b>xi</b>
<b>Chapter 1: Introduction .....</b>	<b>1</b>
1.1 Motivation .....	1
1.2 History of metal-oxygen batteries .....	3
1.3 Review of literature .....	6
1.3.1 State of the art .....	6
1.3.2 The discharge product .....	9
1.3.3 Discharge/recharge mechanisms .....	12
1.3.4 Challenges and failure modes .....	14
1.4 Goals of this study .....	18
<b>Chapter 2: Methodology .....</b>	<b>19</b>
2.1 Introduction .....	19
2.2 Electronic structure methods .....	21
2.2.1 Kohn-Sham density functional theory .....	21
2.2.2 Exchange-correlation functionals .....	24
2.2.3 GW methods .....	27
2.2.4 Computational tools: basis sets, pseudopotentials, and k-points .....	30
2.2.5 Implementation .....	32
2.3 Point defects .....	33
2.3.1 Thermodynamics .....	33

2.3.2	Kinetics .....	36
<b>Chapter 3:</b>	<b>Transport in intrinsic crystalline <math>\text{Li}_2\text{O}_2</math>.....</b>	<b>38</b>
3.1	<i>Introduction</i> .....	38
3.2	<i>Methods</i> .....	40
3.3	<i>Defect thermodynamics</i> .....	42
3.4	<i>Defect mobilities</i> .....	45
3.5	<i>Influence of the exchange-correlation functional</i> .....	49
3.6	<i>Discussion</i> .....	54
<b>Chapter 4:</b>	<b>Amorphous <math>\text{Li}_2\text{O}_2</math> .....</b>	<b>57</b>
4.1	<i>Introduction</i> .....	57
4.2	<i>Methods</i> .....	59
4.3	<i>Results</i> .....	62
4.3.1	Bulk properties .....	62
4.3.2	Defect chemistry .....	64
4.4	<i>Discussion</i> .....	72
<b>Chapter 5:</b>	<b>Doped <math>\text{Li}_2\text{O}_2</math> .....</b>	<b>73</b>
5.1	<i>Introduction</i> .....	73
5.2	<i>Methods</i> .....	76
5.3	<i>Defect chemistry</i> .....	79
5.4	<i>Transport model</i> .....	84
5.4.1	Governing equations .....	87
5.4.2	Constitutive laws .....	87
5.4.3	Boundary conditions .....	89
5.4.4	General remarks .....	90
5.4.5	Scenario I: Layer-by-layer stripping/deposition .....	91
5.4.6	Scenario II: Two-phase delithiation .....	94
5.5	<i>Discussion</i> .....	95
<b>Chapter 6:</b>	<b><math>\text{Li}_2\text{O}_2</math> surfaces .....</b>	<b>98</b>
6.1	<i>Introduction</i> .....	98
6.2	<i>Methods</i> .....	99
6.2.1	Surface formation energies .....	99
6.2.2	Surface reconstruction .....	100
6.2.3	Defect chemistry .....	103

6.3	<i>Surface thermodynamics and electronic structure</i> .....	105
6.4	<i>Surface defect chemistry</i> .....	110
6.5	<i>Discussion</i> .....	114
<b>Chapter 7: Space-charge effects in thin films</b> .....		<b>116</b>
7.1	<i>Introduction</i> .....	116
7.2	<i>Formulation of the model</i> .....	117
7.3	<i>Results</i> .....	120
7.4	<i>Discussion</i> .....	124
<b>Chapter 8: Conclusions</b> .....		<b>127</b>
<b>Appendices</b> .....		<b>130</b>
<b>References</b> .....		<b>141</b>

## List of Figures

Figure 1.1 Vergnes' 1860 Zn-air battery design .....	3
Figure 1.2 Schematic of a Li-O <sub>2</sub> cell .....	6
Figure 1.3 Reported capacities for galvanostatic discharge of Li-O <sub>2</sub> cells .....	8
Figure 1.4 Potential profile from a galvanostatic discharge/charge cycle of a parallel electrode aprotic Li-O <sub>2</sub> battery .....	9
Figure 1.5: Morphology of an Li <sub>2</sub> O <sub>2</sub> disk .....	10
Figure 3.1 Crystal structure of Li <sub>2</sub> O <sub>2</sub> .....	40
Figure 3.2 Formation energies of low-energy defects in Li <sub>2</sub> O <sub>2</sub> .....	43
Figure 3.3 Nearest neighbor hole polaron hopping paths .....	46
Figure 3.4 Energy profiles for hole polaron hopping .....	47
Figure 3.5 Energy levels associated with the band edges, polaron ground states, and transition states .....	50
Figure 3.6 Magnetization density isosurface of the hole polaron .....	52
Figure 3.7 Predicted electronic conductivity as a function of cell voltage .....	54
Figure 4.1 Temperature profile used for melt-and-quench AIMD .....	59
Figure 4.2 Structure of amorphous Li <sub>2</sub> O <sub>2</sub> .....	63
Figure 4.3 Density of states for c-Li <sub>2</sub> O <sub>2</sub> and a-Li <sub>2</sub> O <sub>2</sub> .....	64
Figure 4.4 Formation energies of point defects and polarons in a-Li <sub>2</sub> O <sub>2</sub> .....	65
Figure 4.5 Pathway used to estimate Li vacancy migration rate .....	67
Figure 4.6 Polaron hopping in amorphous Li <sub>2</sub> O <sub>2</sub> .....	70
Figure 5.1 Ternary Li-Co-O phase diagram .....	77
Figure 5.2 Calculated formation energies of Co impurities .....	79
Figure 5.3 Crystal field splittings for Co substitutions .....	83
Figure 5.4 Model for transport through a doped Li <sub>2</sub> O <sub>2</sub> film .....	85
Figure 5.5 Calculated potential drop as a function of current density for doped Li <sub>2</sub> O <sub>2</sub> films .....	92
Figure 5.6 Calculated defect concentrations and electrostatic potential for Scenario I .....	93
Figure 6.1 Conceptual illustration of surface compensating charge self-trapping .....	101
Figure 6.2 Comparison of GGA and HSE surface formation energies .....	105
Figure 6.3 Equilibrium crystallite shapes predicted from (a) PBE and (b) HSE surface energies. ....	106
Figure 6.4 Comparison of GGA and HSE surface band gaps .....	108
Figure 6.5 Alignment of the Li <sub>2</sub> O <sub>2</sub> valence band maximum .....	109
Figure 6.6 Defect formation energy plot for the {0001} stoichi-4 surface .....	110
Figure 6.7 Defect formation energy plot for the {1-100} stoichi-3 surface .....	111
Figure 6.8. Hole polaron hopping pathways on the {0001} stoichi-4 surface .....	112
Figure 6.9. Energy profiles for hole polaron hopping at the {0001} stoichi-4 surface .....	112

Figure 6.10 Hole polaron hopping pathways on the {1–100} stoichi-3 surface.....	113
Figure 6.11 Energy profiles for hole polaron hopping at the {1–100} stoichi-3 surface. ....	113
Figure 7.1: Schematic of transport model. ....	117
Figure 7.2 Simulated potential as a function of discharge capacity for uniform Li <sub>2</sub> O <sub>2</sub> deposition.....	123
Figure A.1 Convergence of the GGA+G <sub>0</sub> W <sub>0</sub> band edges and band gap with respect to the number of bands used in the calculation. ....	130
Figure A.2 Size convergence of the V <sub>Li</sub> <sup>-</sup> (Oct) PBE formation energy.....	131
Figure A.3 Size convergence of the hole polaron formation energy .....	132
Figure A.4 Size convergence of the surface V <sub>Li</sub> <sup>-</sup> formation energy.....	133
Figure C.5 Dimensionless concentration and electric field.....	140

## List of Tables

Table 1.1 Projected system-level energy densities for non-aqueous Li-O <sub>2</sub> batteries. ....	2
Table 1.2 Summary of metal-air and metal-oxygen chemistries reported to date. ....	4
Table 2.1. Summary of <i>GW</i> methods. ....	30
Table 3.1 Equilibrium defect formation energies (eV) and concentrations (cm <sup>-3</sup> ) in Li <sub>2</sub> O <sub>2</sub> . ....	43
Table 3.2 Migration barriers for V <sub>Li</sub> <sup>-</sup> migration ....	45
Table 4.1 Structural parameters and relative energies for five candidate models for amorphous Li <sub>2</sub> O <sub>2</sub> ....	62
Table 4.2 Comparison of formation energies of point defects and polarons in a-Li <sub>2</sub> O <sub>2</sub> ....	66
Table 4.3 Migration barriers between vacancy sites in amorphous Li <sub>2</sub> O <sub>2</sub> ....	67
Table 4.4 Hole polaron hopping barriers in amorphous Li <sub>2</sub> O <sub>2</sub> ....	71
Table 5.1 Gibb's free energies of formation for Li-Co-O compounds. ....	77
Table 5.2 Equilibrium formation energies and concentrations of Co substitutions and intrinsic defects. ....	80
Table 5.3 Cation-anion distances and lattice strain energies for Co substitutions ....	81
Table 6.1 Surface formation energies and surface band gaps ....	107
Table 7.1 Values of parameters used in the model and relevant values from the literature. ....	123
Table B.1 Parameters used to determine overpotential for a hypothetical Li-O <sub>2</sub> battery. ....	134

## **List of Appendices**

Appendix A: Convergence tests .....	130
Appendix B: Target conductivity estimate.....	134
Appendix C: Electroneutrality violations.....	135

## Abstract

Li-O<sub>2</sub> batteries are a very attractive energy storage technology due to their high theoretical specific energy density. However, several critical challenges impede the development of a practical Li-O<sub>2</sub> battery. One of these challenges is the sluggish transport of ions and/or electrons through the Li<sub>2</sub>O<sub>2</sub> discharge product. The purpose of this work is to develop a physics-based picture of transport phenomena within the Li-O<sub>2</sub> discharge product and to elucidate how different characteristics of the discharge product influence its apparent transport properties. To this end we employ density functional theory calculations in conjunction with continuum-scale transport models.

Our calculations indicate that charge transport in bulk Li<sub>2</sub>O<sub>2</sub> is mediated by hole polarons and Li-ion vacancies, and that a low concentration of these species results in poor intrinsic ionic and electronic conduction. However, structural disorder, the presence of impurities, and the formation of space-charge layers are predicted to significantly enhance charge transport. These results suggest several design strategies for improving Li-O<sub>2</sub> cell performance: promoting the formation of amorphous Li<sub>2</sub>O<sub>2</sub>, introducing impurities into the discharge product, controlling crystallite orientation in the discharge product, and increasing the operating temperature.

# Chapter 1: Introduction

## 1.1 Motivation

The world now rests on the threshold of an *energiewende* ('energy transition'): the shift towards renewable, efficient, and sustainable energy conversion and storage technologies.<sup>1,2</sup> One force driving this change is the growing awareness, within and beyond the scientific community, of the extent of the growing impact of modern civilization on the environment.<sup>3</sup> Geopolitical and economic challenges associated with fossil fuels also provide impetus for change.<sup>4</sup>

Energy storage is anticipated to play a major role in enabling an *energiewende*, in particular for grid storage and transportation.<sup>1,4,5</sup> Although Li-ion batteries are now widely used in portable electronic devices and electric vehicles, high costs and low gravimetric/volumetric energy densities have spurred the search for new energy storage systems.<sup>4,5</sup> Often referred to as 'beyond-lithium-ion' technologies, these speculative devices include reversible metal-air chemistries such as the Li-O<sub>2</sub> battery<sup>6-11</sup> which exhibits a high theoretical specific energy density of 3,505 Wh/kg (including the mass of oxygen).<sup>6</sup> The dominant positive electrode reaction within a non-aqueous Li-O<sub>2</sub> battery involves the reversible reaction of lithium with oxygen, yielding solid lithium peroxide, Li<sub>2</sub>O<sub>2</sub>, as the discharge product:<sup>12</sup>  $2\text{Li}^+ + \text{O}_2 + 2e^- \rightleftharpoons \text{Li}_2\text{O}_2$ .

Although Li-O<sub>2</sub> batteries have not been commercialized as of 2014, Table 1.1 shows several projections of how such a battery could perform at the system level with respect to gravimetric and volumetric energy densities. Although there is significant variation in the projected gravimetric and volumetric energy densities depending on the state of charge and system design, all of the projections are well above the system-level gravimetric and volumetric energy densities of state of the art Li-ion systems. The following sections discuss the main challenges must be

overcome before the projections in Table 1.1 can be achieved in a practical battery.

**Table 1.1** Projected system-level energy densities for non-aqueous Li-O<sub>2</sub> batteries.

<b>Battery chemistry</b>	<b>Institution</b>	<b>Gravimetric energy density (Wh/kg)</b>	<b>Volumetric energy density (Wh/L)</b>
Li-O <sub>2</sub> (projected)	JCESR <sup>13</sup>	220-530	310-450
	Bosch <sup>14</sup>	630-860	530-960
	Ford <sup>15</sup>	640	600
Li-ion (state-of-the-art)	JCESR <sup>13</sup>	60-130	80-220

## 1.2 History of metal-oxygen batteries

The long history of metal-oxygen batteries is often unappreciated. The earliest written description of a metal-oxygen battery we have been able to find is Vergnes' Zn-air battery from 1860.<sup>16</sup> Figure 1.1 shows Vergnes' design, containing a zinc metal anode and a porous platinized coke positive electrode. This design is in some respects remarkably similar to today's advanced metal-oxygen cells, which frequently employ porous carbon positive electrodes and noble-metal catalysts.<sup>17</sup> Zn-air batteries matured into a practical energy storage technology in the early 20<sup>th</sup> century,<sup>18</sup> and as of the early 21<sup>st</sup> century still remain the most prominent metal-oxygen chemistry. Industrially produced primary Zn-air cells are employed in a number of applications, such as hearing aids, due to their high energy density.<sup>19</sup>

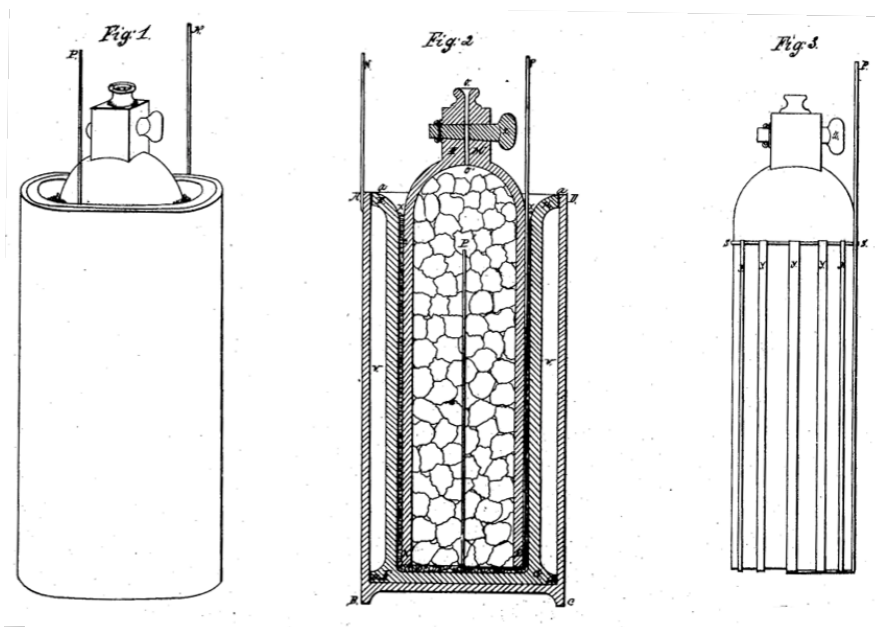


**Figure 1.1** Vergnes' 1860 Zn-air battery design.<sup>16</sup>

Over the years, many other metal-oxygen couples have also been considered. In Table 1.2, we enumerate all metals for which we were able to find reports of an

operating metal-oxygen cell. (We use the term ‘metal-oxygen’ to refer to cells that include O<sub>2</sub> as a reactant, regardless of whether the source is air, sea water, or an O<sub>2</sub> tank, and ‘metal-air’ to refer to cells which draw one or more reactants from the air.) The references cited in Table 1.2 are not intended to capture all of the work done on each metal-air couple, but rather to highlight review articles and representative experiments. While all of these chemistries can in principle be mechanically recharged (by replacing the metal anode), in Table 1.2 we denote only those that are electrochemically rechargeable as ‘secondary batteries’. Also related to metal-oxygen batteries but not listed in Table 1.2 are metal-hydride-oxygen batteries, which are characterized by reactions of the form  $4MH + O_2 \rightarrow 4M + 2H_2O$ .<sup>20</sup>

**Table 1.2** Summary of metal-air and metal-oxygen chemistries reported to date.

	<b>Aqueous</b>	<b>Non-aqueous</b>
Li	Secondary <sup>14</sup>	Secondary <sup>14,17,21</sup>
Na	Primary <sup>22</sup>	Secondary <sup>23</sup>
K		Secondary <sup>24</sup>
Mg	Primary <sup>19,25</sup>	Secondary <sup>26</sup>
Ca	Primary <sup>19</sup>	
V	Secondary <sup>27</sup>	
Mo	Primary <sup>28</sup> & secondary <sup>29</sup>	
W	Secondary <sup>30</sup>	
Fe	Secondary <sup>19</sup>	
Zn	Secondary <sup>19</sup>	
Cd	Secondary <sup>31</sup>	
Al	Primary <sup>19,25</sup> & secondary <sup>32</sup>	
Si	Primary <sup>33</sup>	Primary <sup>34</sup>
Sn	Primary <sup>35</sup>	

The birth of the modern non-aqueous Li-O<sub>2</sub> battery is generally considered to be the 1996 demonstration of a room-temperature secondary cell by Abraham and Jiang.<sup>36</sup> While this development was a major breakthrough, the history of earlier Li-O<sub>2</sub> batteries is often overlooked. The first investigation of the Li-O<sub>2</sub> couple, to the best of our knowledge, dates back to 1966.<sup>37</sup> Although this study employed non-aqueous electrolytes (including propylene carbonate, today’s preeminent Li-

ion solvent), the design pursued was a ‘moist’ Li-O<sub>2</sub> system: the air supply was saturated with water vapor. Interestingly, even this preliminary study identified some of the issues which remain critical for modern Li-O<sub>2</sub> cells, such as the formation of lithium carbonate and the role of impurities.<sup>37</sup>

Other Li-O<sub>2</sub> designs emerged later. Primary Li-O<sub>2</sub> cells with aqueous electrolytes received considerable attention in the 1970s,<sup>38</sup> and moisture-free high-temperature secondary cells were later developed in the 1980s.<sup>39</sup> However, Abraham and Jiang’s 1996 study is, to the best of our knowledge, the first demonstration of a moisture-free room temperature secondary Li-O<sub>2</sub> cell,<sup>36</sup> and represents the first modern non-aqueous Li-O<sub>2</sub> battery. A amusing historical note is that the development of this cell was not intentional, but a serendipitous discovery due to the leakage of oxygen from a syringe into a sealed lithium-graphite cell.<sup>40</sup>

Since 1996, research on non-aqueous Li-O<sub>2</sub> cells grown immensely. This has also led to the development of related chemistries, including true Li-air cells<sup>41</sup> (i.e., using ambient air rather than pure oxygen) and also reversible aqueous Li-O<sub>2</sub> cells.<sup>14</sup> It is not possible to summarize all of the studies performed to date. Instead, we strive to summarize and unify the key lessons, observations, and hypotheses that have been presented in the literature. For additional details beyond those presented here, the reader is encouraged to explore other reviews of the field.<sup>14,17,21</sup>

## 1.3 Review of literature

### 1.3.1 State of the art

Figure 1.2 shows a schematic of a typical non-aqueous Li-O<sub>2</sub> cell. During discharge, Li from the negative electrode and O<sub>2</sub> from either the atmosphere or an oxygen tank combine to form Li<sub>2</sub>O<sub>2</sub>, which precipitates out within a porous positive electrode. During recharge, the reaction is reversed, and the Li<sub>2</sub>O<sub>2</sub> decomposes and releases Li to the negative electrode and oxygen to the atmosphere or tank.

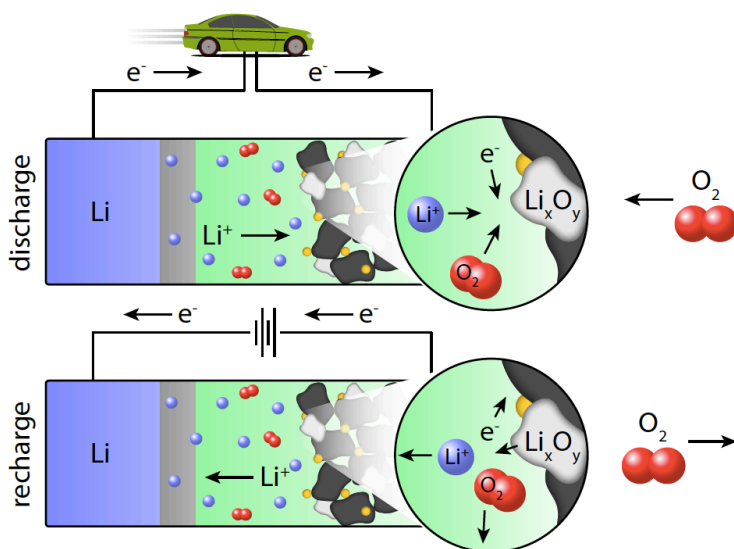


**Figure 1.2** Schematic of a Li-O<sub>2</sub> cell. Blue represents a Li metal negative electrode, gray the separator, green the organic liquid electrolyte, black a porous carbon positive electrode support, yellow a catalyst, and gray the discharge product.

Much of the research on non-aqueous Li-O<sub>2</sub> batteries has focused on improving four critical aspects of performance: rate capability, capacity, voltaic efficiency, and cycle life. Some state-of-the-art Li-O<sub>2</sub> cells have been demonstrated to perform adequately with regard to these measures individually, but none have performed satisfactorily in all four simultaneously. This is because

rate capability, capacity, voltaic efficiency, and cycle life are highly interdependent, often in surprising ways. Some interdependencies include:

1. Higher discharge rates reduce maximum capacity; this is discussed in more detail in Chapter 7.
2. Curtailing the discharge capacity increases cycle life and voltaic efficiency.
3. Higher discharge rates (at fixed capacity) may *improve* voltaic efficiency, as the discharge product morphologies produced at high currents can exhibit lower charging overpotentials than the morphologies produced at low currents.<sup>42</sup>

The tradeoff between current and capacity is illustrated in Figure 1.3, which shows the capacities and rates obtained in various Li-O<sub>2</sub> cells, normalized to the mass of the pristine (charged) electrode (including catalyst and binder, if present). (The mass of any substrate or current collector is not included). Additionally, the capacities (similarly normalized) assumed in several hypothetical designs for practical Li-O<sub>2</sub> batteries<sup>13-15</sup> are shown as horizontal lines. Several experiments have achieved target capacities of ~1000 mAh/g at reasonably high rates (~1 hour discharge). However, this comes at the cost of cycle life and voltaic efficiency.

Furthermore, a practical Li-O<sub>2</sub> battery requires that the electrode be fairly thick; otherwise, the mass and volume of the inactive components (e.g., separators, electrolyte, current collectors, packaging) will reduce the system-level energy and power density. While most experiments consider electrodes of thickness ~10 μm, proposed battery designs have assumed thicknesses of 150-300 μm.<sup>13-15</sup> Full utilization of thick electrodes is likely limited by oxygen transport, as discussed in Section 1.3.4. Thus the development of a practical Li-O<sub>2</sub> battery will require either a solution to the oxygen transport problem, or a battery pack design that achieves high system-level performance with thin electrodes.

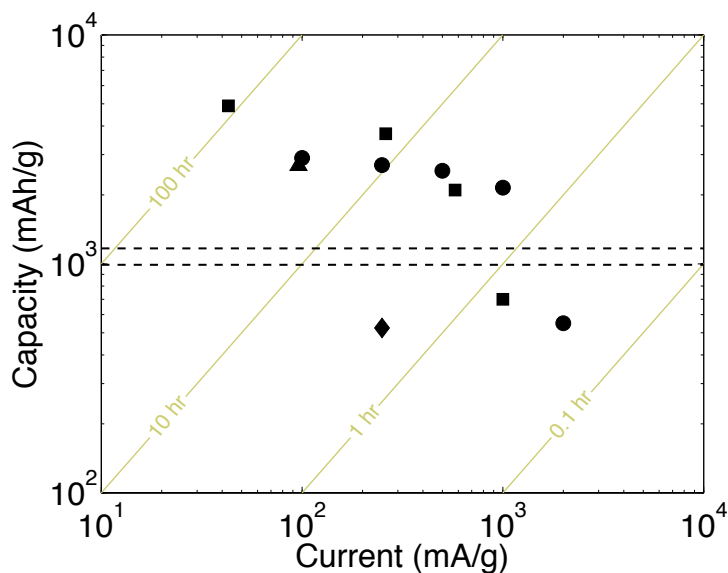


**Figure 1.3** Reported capacities for galvanostatic discharge of Li-O<sub>2</sub> cells taken from various experiments.<sup>43–46</sup> Capacities and currents are normalized to the mass of the support, binder, and catalyst in the positive electrode. Horizontal dashed lines are capacities assumed in hypothetical battery designs.<sup>13,15</sup>

Figure 1.4 shows the potential profile from a galvanostatic discharge/charge cycle of a typical non-aqueous Li-O<sub>2</sub> cell. The ‘sudden death’ behavior during discharge limits the capacity, and the high recharge overpotential  $\eta_{\text{chg}}$  results in a low voltaic efficiency. In the next section, we summarize the key observations and theories regarding the operating mechanisms and origins of these performance limitations. It is important to keep in mind that different mechanisms may dominate under different conditions. For example, it has been shown that the current density,<sup>42</sup> positive electrode material/architecture,<sup>47,48</sup> and system cleanliness<sup>49–51</sup> can play a significant role in the reaction mechanisms.

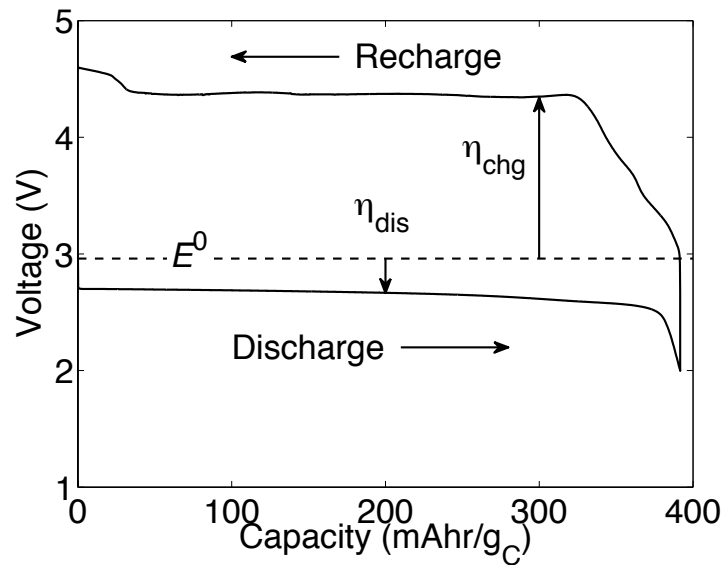


**Figure 1.4** Potential profile from a galvanostatic discharge/charge cycle of a parallel electrode aprotic Li-O<sub>2</sub> battery with a porous carbon positive electrode, Li metal anode, and LiTFSI/DME electrolyte at a current of 0.2 mA/cm<sup>2</sup>. Data courtesy of L. Griffith, Monroe research group.

### 1.3.2 The discharge product

The first step in understanding the performance of Li-O<sub>2</sub> batteries is understanding the discharge product. It is often presumed that the discharge product is bulk crystalline Li<sub>2</sub>O<sub>2</sub>; however, the discharge product can have a complex morphology, structure, and composition.

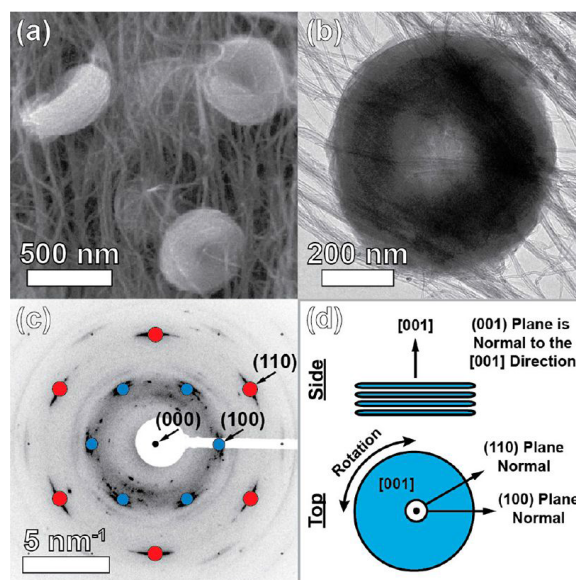


**Figure 1.5:** Morphology of an  $\text{Li}_2\text{O}_2$  disk. (a) SEM, (b) bright-field TEM, (c) electron diffraction pattern, (d) schematic of microstructure, taken from Mitchell et al.<sup>52</sup>

*Morphology.* A number of different discharge product morphologies have been reported, including disks,<sup>42,52</sup> films,<sup>52,53</sup> needles, and hollow spheres.<sup>54</sup> Biconcave disks (similar to red blood cells) are among the most commonly observed morphologies. (This morphology is often referred to as a ‘toroid’; however, these particles are not strictly speaking toroids because they lack a hole that runs through the center of the disk.) Figure 1.5 shows the basic structure of an  $\text{Li}_2\text{O}_2$  disk, which consists of a stack of flat crystallites. The disks are highly textured (i.e., the misorientation between crystallites is small), with the  $\{0001\}$  axis being aligned approximately with the central axis of the disk. In some cases the regions between the plates appear to be filled by the electrolyte,<sup>51</sup> but in others it has been suggested that the inter-plate regions contain a distinct phase or grain boundary region.<sup>55</sup> This second phase could be, for example, amorphous  $\text{Li}_2\text{O}_2$  or a lithium-deficient compound such as  $\text{Li}_{2-x}\text{O}_2$ .

The growth mechanism for  $\text{Li}_2\text{O}_2$  deposits is not well understood. It has been reported that low current densities and high water concentrations (hundreds to thousands of ppm) both promote the growth of biconcave disks.<sup>42,51,52,56</sup> It is interesting to note that similar biconcave disks have also been observed in the precipitation of silicates<sup>57</sup> and corn starch<sup>58</sup>, suggesting that there may be a

common growth mechanism. It has also been reported that the size of deposit particles decreases with increasing current densities, and that at sufficiently high rates, the deposit forms a conformal film rather than discrete particles.<sup>42,51,52,56</sup> A continuum-scale growth model has been proposed to explain this transition from particle to film.<sup>59</sup> It has also been suggested that the putative conformal films produced at high currents are in fact carpets of nano-scale needles.<sup>60</sup> Note that it can be the case that multiple distinct morphologies appear concurrently in the positive electrode of a single cell; for example, disks and thin films have been observed together.<sup>52</sup>

*Crystallinity.* A growing number of experiments have suggested that the discharge that amorphous  $\text{Li}_2\text{O}_2$  can be present in the discharge product.<sup>42,47,48,54</sup> The formation of an amorphous deposit is consistent with Ostwald's rule, which states that unstable phases tend to precipitate before stable phases.<sup>61-63</sup> It has been reported that higher discharge rates<sup>42</sup>, as well as certain catalysts, can promote the formation of amorphous  $\text{Li}_2\text{O}_2$ .<sup>47,48</sup>

Several experimental<sup>42,47,48</sup> and computational<sup>47,64</sup> studies have suggested that amorphous  $\text{Li}_2\text{O}_2$  is easier to recharge than crystalline  $\text{Li}_2\text{O}_2$ , perhaps due to improved electron or Li-ion transport properties. This is discussed in greater detail in Chapter 4. If correct, this would suggest that Li- $\text{O}_2$  electrode designs (or operating conditions) which promote the formation of amorphous  $\text{Li}_2\text{O}_2$  may yield superior performance.

*Superoxide components.* Another recurring theme is the observation of superoxide ions,  $\text{O}_2^-$ , in the discharge product.<sup>65</sup> The presence of a superoxide component perhaps should not be a surprise, given that it is known that other alkali metals form mixed peroxide-superoxide phases.<sup>66</sup> It remains unclear where exactly the superoxide component resides in the discharge product. It has been suggested to represent a surface species,<sup>67,68</sup> an oxygen-rich phase located in the inter-plate regions,<sup>55</sup> or to represent a hole polaron.<sup>69,70</sup> The role of superoxide is revisited in the concluding remarks in Chapter 8.

*Side reaction products.* It has been recognized that Li-O compounds are not the only phases present in the discharge product. Side reactions (i.e., decomposition of the salt, solvent, or positive electrode) have been observed to produce other compounds, such as lithium carbonate, lithium acetate, lithium formate, and lithium fluoride.<sup>71,72</sup> These side reaction products can comprise a substantial fraction of the discharge product; one experiment found that in a typical Li-O<sub>2</sub> cell with an ether solvent, the yield of Li<sub>2</sub>O<sub>2</sub> was only 91% of the theoretical amount expected from coulometry.<sup>71</sup> It is important to note that in addition to the precipitated side reaction products, there may be additional soluble side reaction products.

### ***1.3.3 Discharge/recharge mechanisms***

A number of different discharge mechanisms have been proposed, which we summarize here. It is important to keep in mind that different mechanisms may dominate depending on the experimental conditions (e.g., rate, electrolyte, electrode/catalyst, temperature, depth of discharge, and cleanliness).

*Layer-by-layer electrodeposition/electrostripping.* In some cases, it has been suggested that the growth/dissolution of a film occurs via the layer-by-layer electrochemical deposition/stripping of Li<sub>2</sub>O<sub>2</sub>. In such a mechanism, electron transport presumably would occur through the growing deposit. It has been suggested that this could occur via electron tunneling<sup>53,73</sup> or hole polaron hopping,<sup>69,70,74</sup> as discussed later in this work. Flat-electrode experiments have been used to probe layer-by-layer growth, and find that after a thickness of ~5 nm, the electrode is passivated during discharge.<sup>53,73</sup> This ‘sudden-death’ behavior and the mechanisms for charge transport in Li<sub>2</sub>O<sub>2</sub> thin films are discussed in greater detail in Chapter 7.

*Solution-mediated precipitation/dissolution.* The growth of large particles has been proposed to occur via a solution-mediated precipitation process, which allows charge-transport limitations through the particles to be bypassed.<sup>11,42</sup> For

example, one proposed discharge mechanism is that  $O_2$  is reduced on the positive electrode surface to form  $LiO_2$ :  $Li^+ + O_2 + e^- \rightarrow LiO_2$ . The  $LiO_2$  could then diffuse in the electrolyte (or perhaps along the positive electrode surface), and then precipitate out via a disproportionation reaction:  $2LiO_2 \rightarrow Li_2O_2 + O_2$ . Such a mechanism requires that there be an intermediate species (be it  $LiO_2$  or something else) which is either at least sparingly soluble or capable of rapid surface diffusion.

A solution-mediated process (such as the reverse of the above reactions) could also occur during recharge. For example, it has been proposed that impurities present as contaminants or by-products of electrolyte decomposition may serve as the soluble intermediate species.<sup>50</sup> These impurities in effect function as redox mediators, or perhaps transform  $Li_2O_2$  into a more soluble species. For example, a small amount of protons has been suggested to enable a recharge mechanism that begins with the transformation of  $Li_2O_2$  into  $H_2O_2$  via a single-displacement reaction,  $Li_2O_2 + 2H^+ \rightarrow H_2O_2 + 2Li^+$ .<sup>50</sup>  $H_2O_2$ , being more soluble than  $Li_2O_2$ , could then diffuse to the electrode and be electrochemically oxidized via the reaction  $H_2O_2 \rightarrow 2H^+ + O_2 + 2e^-$ , yielding a net reaction of  $Li_2O_2 \rightarrow 2Li^+ + O_2 + 2e^-$ .

*Topotactic delithiation.* The partial delithiation of the discharge product has been suggested to be the first step of recharge.<sup>75</sup> This could occur as a two-phase reaction:  $Li_2O_2 \rightarrow Li_{2-x}O_2 + xLi^+ + xe^-$ . The equilibrium potential for this reaction when  $x = 1$  has been calculated from first-principles methods to be 0.3-0.4 V above the equilibrium potential for the oxidation of  $Li_2O_2$  to  $Li$  and  $O_2$ .<sup>75</sup> Delithiation via a solid solution pathway is discussed further in Chapter 3. Even if phase separation to  $Li_2O_2$  and  $Li_{2-x}O_2$  is thermodynamically preferable, it is known for other Li-ion insertion materials that interfacial energies and transport limitations can prevent phase separation from occurring.<sup>76</sup> It is important to note that even if a delithiation process occurs, the intermediate lithium-deficient phase may not be readily observable if recharge occurs one particle at a time (i.e., via a ‘domino cascade’ mechanism).<sup>76</sup>

### 1.3.4 Challenges and failure modes

*Charge transport within the discharge product.* Charge transport through the discharge product has been thought to limit the performance of Li-O<sub>2</sub> cells in many circumstances.<sup>53,77–80</sup> The presence of a passivating layer on the positive electrode would shut down electrochemical activity, potentially leading to limitations in capacity, voltaic efficiency, and rate capability. Although the charge-transport mechanism(s) at play are not well understood, several mechanisms have been proposed:

1. *Electron tunneling.* In thin films (< 5 nm), electron tunneling has been suggested to be the dominant charge-transport mechanism.<sup>53,73</sup>
2. *Hole polaron hopping.* Experiments and first-principles modeling (see Chapter 3) have found that hole polarons are the dominant electronic charge carrier in Li<sub>2</sub>O<sub>2</sub>.<sup>69,70,81</sup>
3. *Li-ion vacancy diffusion.* Experiments and first-principles modeling (see Chapter 3) have found that Li-ion vacancies are the dominant Li defect in Li<sub>2</sub>O<sub>2</sub>.<sup>70,81</sup> The role of Li-ion vacancies is different from that of electronic charge carriers because ionic defects cannot readily cross the interface between the discharge product and electrode support. That is, at the Li-O<sub>2</sub> equilibrium potential, the amount of Li which can be inserted into (or deinserted from) the positive electrode support typically represents only a small fraction of the amount of Li in the discharge product. Thus the support can be thought of as an ion-blocking electrode.
4. *Conduction via extended defects.* Some studies have speculated that charge transport in Li<sub>2</sub>O<sub>2</sub> could be enhanced at extended defects, such as surfaces,<sup>67,68,82</sup> grain boundaries,<sup>83</sup> amorphous regions,<sup>47,64</sup> or interfaces.<sup>84</sup> Transport in amorphous Li<sub>2</sub>O<sub>2</sub> is discussed in Chapter 4, while transport at Li<sub>2</sub>O<sub>2</sub> surfaces is discussed in Chapter 6.

*Oxygen transport in the electrolyte.* It has been recognized that in many cell designs, oxygen transport can limit discharge capacity.<sup>77,85–88</sup> This can be a result

of pore-clogging, i.e., the obstruction of oxygen-diffusion pathways by the discharge product.<sup>87</sup> Even in the absence of pore clogging, the smallness of the solubility and diffusion coefficient of oxygen in the electrolyte can limit performance.<sup>88</sup> Oxygen transport limitations can lead to a sudden drop in voltage during a galvanostatic discharge (sudden death).<sup>87,88</sup>

*Kinetics.* A number of studies have examined the kinetics of Li-O<sub>2</sub> cells. Systematic experiments have found that both the discharge and recharge kinetics are facile.<sup>80</sup> Several computational studies have explored mechanisms for the layer-by-layer deposition/stripping of Li<sub>2</sub>O<sub>2</sub>. The ‘thermodynamic overpotentials’ associated with layer-by-layer deposition/stripping were found to be small (< 0.2 V), and it was suggested on this basis that kinetics would be fast.<sup>89</sup> (Note, however, that thermodynamic overpotentials can only be compared qualitatively to the overpotentials observed in experiments; for example, the thermodynamic overpotentials do not account for the density of reactive sites (e.g., step edges or kinks) or the exchange currents associated with different reaction steps.) A few other first-principles studies concluded that the kinetics of layer-by-layering deposition/stripping was slow, and would limit cell performance.<sup>90,91</sup> The differences among conclusions in the literature result primarily not from differences among atomistic calculations, but rather from differing interpretations of the computational results – that is, how the energies for various reaction steps relate to the current-voltage relationship.

*Degradation.* Most experiments on Li-O<sub>2</sub> systems prior to 2010 used electrolytes developed for Li-ion batteries, employing carbonate solvents such as propylene carbonate (PC), ethylene carbonate (EC), and dimethyl carbonate (DMC). These solvents were natural choices, as they had been widely successful for Li-ion batteries; some even refer to PC as ‘the new water’ due to its widespread use for Li-ion electrochemistry.<sup>92</sup> In 2010 the Li-O<sub>2</sub> community began to show that carbonates solvents are in fact highly unstable in Li-O<sub>2</sub> cells.<sup>93–95</sup> Most of the studies prior to 2010 must be regarded with caution, since electrolyte degradation,

rather than Li-O electrochemistry, is thought to dominate carbonate-containing Li-O<sub>2</sub> cells.

It is now recognized that solvent stability is a critical issue for Li-O<sub>2</sub> batteries,<sup>14,17</sup> and furthermore it has been observed the salt<sup>96-98</sup> and positive electrode<sup>99</sup> can also react irreversibly. Much work presently is being done to design stable Li-O<sub>2</sub> cells. Carbonate solvents have been abandoned in favor of ethers, sulfoxides, ionic liquids, and other solvent classes. Although an improvement over carbonates, even these solvents exhibit substantial degradation.<sup>71,72</sup> For example, a typical ethereal electrolyte with a carbon positive electrode was found to exhibit an Li<sub>2</sub>O<sub>2</sub> yield of at most 91%.<sup>71</sup> Improved stability has been reported for certain combinations, such as LiClO<sub>4</sub>/DMSO with a nanoporous gold positive electrode.<sup>100</sup> Since the number of possible salt/solvent/electrode combinations is large, a mechanistic understanding of degradation processes may be important for identifying combinations with high stability. Here we summarize some of the solvent degradation processes that have been proposed. (Less effort has been invested in a mechanistic understanding of salt<sup>97,101</sup> and positive electrode stability, although these are clearly critical issues.)

1. *Chemical attack by electrochemical intermediates.* It is thought that chemical attack by intermediates of the oxygen reduction reaction during discharge can cause substantial degradation in some solvents. In particular, attack by superoxide (O<sub>2</sub><sup>-</sup>) radicals is thought to be the main source of decomposition in carbonate solvents.<sup>102</sup> Some have also suggested that during recharge, oxidation intermediates could also lead to solvent degradation.<sup>103</sup> In particular, ‘nascent’ oxygen evolved during recharge has been speculated to attack the solvent. This term refers to oxygen released in a highly reactive form, such as atomic oxygen or O<sub>2</sub> molecules in the singlet state.
2. *Auto-oxidation.* Organic solvents can undergo auto-oxidation (chemical reaction with molecular O<sub>2</sub>). This has been hypothesized to contribute to solvent degradation in L-O<sub>2</sub> cells.<sup>104,105</sup>

3. *Chemical attack by the discharge product.* Another solvent degradation mechanism is the chemical reaction between the solvent and the discharge product. A few experiments have sought to probe this,<sup>98,106</sup> and atomistic studies have examined solvent degradation on  $\text{Li}_2\text{O}_2$  clusters<sup>107</sup> and surfaces.<sup>108</sup>
4. *Electrochemical oxidation.* In addition to the chemical degradation processes listed above, electrochemical processes can also lead to solvent degradation. Many common solvents exhibit minimal oxidation up to  $\sim 4$  V vs.  $\text{Li}/\text{Li}^+$  on carbon electrodes. However, it has been suggested that solvent oxidation is enhanced by  $\text{Li}_2\text{O}_2$ .<sup>106</sup> Additionally, some oxygen-reduction catalysts used in  $\text{Li}-\text{O}_2$  cells also catalyze solvent oxidation.<sup>109,110</sup>

## 1.4 Goals of this study

Charge transport through the  $\text{Li}_2\text{O}_2$  discharge product is thought to be one of the key limitations in Li- $\text{O}_2$  cells. Although pure bulk  $\text{Li}_2\text{O}_2$  is known to be a poor conductor (as discussed in Chapter 3), the discharge products observed in real cells are in fact more complex, as discussed above in Section 1.3.2.<sup>42,52</sup> The primary aim of this work is to identify structural, morphological, or chemical features of the Li- $\text{O}_2$  discharge product that facilitate facile charge transport. The broader goal is to provide guidelines for designing improved Li- $\text{O}_2$  electrodes: if a specific feature can be shown to facilitate charge transport, then one may be able to improve cell performance by tailoring an electrode to promote the formation of that feature.

This work begins by exploring transport mechanisms in pure bulk crystalline  $\text{Li}_2\text{O}_2$ , and then considers the influence of four features:

1. Poor crystallinity
2. Dopants
3.  $\text{Li}_2\text{O}_2$  surfaces
4. Space-charge effects

To explore the effect of the above items on transport, we combine first-principles atomistic modeling and continuum scale transport theory, as discussed in Chapter 2.

## Chapter 2: Methodology

### 2.1 Introduction

At a microscopic scale, most chemical phenomena are well-described by non-relativistic quantum mechanics, i.e., the time-dependent Schrödinger equation:

$$(2.1) \quad i\hbar \frac{d\Psi}{dt} = \hat{H}\Psi$$

where  $\Psi$  is the many-body wavefunction,  $\hbar$  is the reduced Planck constant, and  $\hat{H}$  is the Hamiltonian operator. We make two simplifications, suitable for the context of this work:

1. The Born-Oppenheimer approximation assumes that the atomic nuclei can be treated classically, and is justified by the large masses of nuclei relative to electrons.
2. Electrons are assumed to be in their ground state, which is justified by the smallness of the thermal energy at ambient temperatures ( $\sim 25$  meV) relative to the typical energy for electronic bonding (on the order of 1 eV).

The electronic ground state for a given configuration of nuclei positions is the lowest energy solution the time-independent Schrödinger equation for the electronic wavefunction,

$$(2.2) \quad \hat{H}\Psi_{\text{electrons}} = E\Psi_{\text{electrons}}$$

Section 2.2 discusses the methods used in the present work for solving this so-called electronic structure problem, while Section 2.3 introduces the statistical physics models which connect microscopic quantities obtained from atomistic simulations to macroscopic quantities used in continuum models.

## 2.2 Electronic structure methods

### 2.2.1 Kohn-Sham density functional theory

Direct numerical solution of Eq. (2.2) is infeasible, even for small systems. For a system of  $N$  electrons, the wavefunction is a complex function of  $3N$  variables:

$$(2.3) \quad \Psi(\mathbf{r}_1, \mathbf{r}_2 \dots \mathbf{r}_N).$$

If this function is to be represented on a grid with  $M$  divisions along each spatial dimension, then a total of  $2M^{3N}$  floating point variables are required. For even modestly sized systems, the amount of memory required is well beyond that available on modern computers. For example, storing the wavefunction of an  $\text{O}_2$  molecule (16 electrons) with 10 divisions of the grid would require  $2 \times 10^{48}$  floating point variables. This value is on par with the number of atoms in Earth; any calculation requiring this much data will be impossible for the foreseeable future.

The power of Kohn-Sham density functional theory (DFT) is to reduce the complexity of the problem by mapping a system of interacting electrons on to a system of non-interacting electrons.

$$(2.4) \quad \Psi(\mathbf{r}_1, \mathbf{r}_2 \dots \mathbf{r}_N) \rightarrow \{\Psi_1(\mathbf{r}), \Psi_1(\mathbf{r}) \dots \Psi_N(\mathbf{r})\}$$

The non-interacting wavefunction, requiring only  $2NM^3$  floating point variables, is vastly easier to handle than the interacting system. The non-interacting wavefunction of an  $\text{O}_2$  molecule could be described with 32,000 floating point numbers, an amount of memory which could easily be stored on a modern computer.

The first Hohenberg-Kohn theorem<sup>111</sup> states that the external potential is uniquely determined (to within a constant) by the ground state charge density. The second Hohenberg-Kohn theorem<sup>111</sup> states that there exists an energy functional of the charge density  $F[n(\mathbf{r})]$  such that for all external potentials  $V_{\text{ext}}(\mathbf{r})$ , the Hohenberg-Kohn functional

$$(2.5) \quad E_{\text{HK}}[n(\mathbf{r})] = \int n(\mathbf{r})v_{\text{ext}}(\mathbf{r})d^3\mathbf{r} + F[n(\mathbf{r})]$$

is minimized over all  $n(\mathbf{r})$  satisfying the normalization condition  $\int n(\mathbf{r})d\mathbf{r} = N$  by the ground state charge density of  $N$  electrons in the potential  $V_{\text{ext}}(\mathbf{r})$ .

The Hohenberg-Kohn theorems form the foundation of density functional theory. Within the Kohn-Sham formalism, Eq. (2.5) is expressed in the form of a system of fictitious non-interacting electrons. To do this, we introduce the exchange-correlation energy:

$$(2.6) \quad E_{\text{XC}}[n] = F[n] - T_0[n] - E_{\text{H}}[n]$$

where

$$(2.7) \quad E_{\text{H}}[n] = \frac{1}{2} \int \frac{n(\mathbf{r})n(\mathbf{r}')}{|\mathbf{r} - \mathbf{r}'|} d\mathbf{r} d\mathbf{r}'$$

is the Hartree energy, representing the classical electrostatic energy, and  $T_0[n]$  is the minimum possible kinetic energy associated with  $N$  electrons whose charge density is  $n(\mathbf{r})$ . Now Eq. (2.5) can be written as

$$(2.8) \quad E_{\text{HK}}[n] = \int n(\mathbf{r})v_{\text{ext}}(\mathbf{r})d\mathbf{r} + E_{\text{H}}[n] + T_0[n] + E_{\text{XC}}[n]$$

Next, we rewrite the charge density in terms of a system of non-interacting electrons:

$$(2.9) \quad n(\mathbf{r}) = \sum_{i=1}^N \psi_i^*(\mathbf{r}) \psi_i(\mathbf{r}),$$

where the wavefunctions obey the orthonormality constraint

$$(2.10) \quad \int \psi_i^*(\mathbf{r}) \psi_j(\mathbf{r}) d\mathbf{r} = \delta_{ij}.$$

Now consider the modified Hohenberg-Kohn functional

$$(2.11) \quad E'_{\text{HK}}\{\psi_i\} = \int n(\mathbf{r}) v_{\text{ext}}(\mathbf{r}) d\mathbf{r} + E_{\text{H}}[n] + T\{\psi_i\} + E_{\text{xc}}[n],$$

where

$$(2.12) \quad T\{\psi_i\} = \sum_{i=1}^N -\frac{\hbar^2}{2m} \psi_i^* \nabla^2 \psi_i$$

is the kinetic energy of the non-interacting electrons. From the definition of  $T_0[n]$ , for fixed  $n$  the minimum of  $E'_{\text{HK}}\{\psi_i\}$  is equal to the minimum of  $E_{\text{HK}}[n]$ . Thus, from the second Hohenberg-Kohn theorem, if one varies  $\{\psi_i\}$ , the minimum value of  $E'_{\text{HK}}\{\psi_i\}$  occurs when  $n$  is the ground-state charge density. The minimum can be found by setting the functional derivatives of  $E'_{\text{HK}}\{\psi_i\}$  to zero, with Lagrange multipliers to account for the orthonormality constraint. This yields the Kohn-Sham equation

$$(2.13) \quad \left\{ -\frac{\hbar^2}{2m} \nabla^2 + V_{\text{ext}}(\mathbf{r}) + V_{\text{H}}[n](\mathbf{r}) + V_{\text{xc}}[n](\mathbf{r}) \right\} \psi_i = \epsilon_i \psi_i,$$

where

$$(2.14) \quad V_{\text{H}}[n](\mathbf{r}) = \frac{\delta E_{\text{H}}[n]}{\delta n(\mathbf{r})} = \frac{1}{2} \int \frac{n(\mathbf{r}')}{|\mathbf{r} - \mathbf{r}'|} d\mathbf{r}' .$$

Eq. (2.13) has the same form as the time-independent Schrödinger equation (Eq. (2.2)) for non-interacting electrons in an effective local potential

$$(2.15) \quad V_{\text{eff}}(\mathbf{r}) = V_{\text{ext}}(\mathbf{r}) + V_{\text{H}}[n](\mathbf{r}) + V_{\text{xc}}[n](\mathbf{r}) .$$

The solution of the Kohn-Sham equation relies on making an approximation for the exchange-correlation functional  $E_{\text{xc}}[n]$ , as discussed in Section 2.2.2. The related *GW* family of methods is discussed in 2.2.3, while Section 2.2.4 discusses key components in the numerical solution of electronic-structure problems.

### 2.2.2 Exchange-correlation functionals

*LDAs.* Among the conceptually simplest class of exchange-correlation functionals are the local-density approximations (LDAs), in which the contribution to the exchange-correlation energy from each point in space depends only on the density at that point:

$$(2.16) \quad E_{\text{xc}}^{\text{LDA}}[n] = \int d^3r n(\mathbf{r}) \varepsilon_{\text{xc}}^{\text{LDA}}(n(\mathbf{r})) .$$

Here  $\varepsilon_{\text{xc}}^{\text{LDA}}(n(\mathbf{r}))$  is the LDA energy density per electron of a homogeneous electron gas (HEG) of density  $n(\mathbf{r})$ . Typically this quantity is fit to match HEG energies obtained from higher levels of theory, such as quantum Monte Carlo methods.<sup>112</sup> Note that for simplicity, here and in subsequent discussions we consider only non-spin-polarized functionals. Generalizations to spin-polarized and non-collinear cases are possible.<sup>113</sup>

GGAs. Allowing for a dependence on the gradient of the electron density can further improve LDAs. These so-called generalized gradient approximations (GGAs) take the form

$$(2.17) \quad E_{xc}^{\text{GGA}}[n] = \int d^3r n(\mathbf{r}) \epsilon_{xc}^{\text{GGA}}\left(n(\mathbf{r}), |\vec{\nabla}n(\mathbf{r})|\right).$$

The parameterization of  $\epsilon_{xc}^{\text{GGA}}$  is typically done by augmenting an LDA exchange-correlation energy function with various analytic expressions to satisfy different limiting cases and bounds.<sup>114,115</sup> In GGAs, the presence of a gradient generally increases the exchange energy and relieves, to some degree, the overbinding of homogeneous systems relative to inhomogeneous ones in LDAs. GGAs and further extensions including higher-order derivatives of the density (meta-GGAs) are collectively referred to as semi-local functionals because the contribution to the exchange-correlation energy from each point in space depends only on the value and derivatives of the density at that point.

Although semilocal functionals provide remarkably good predictions of many chemical properties, there are certain situations which are known to be poorly described by semilocal functionals. Some phenomena known to be particularly problematic are:

1. Van der Waals dispersion interactions<sup>116</sup>
2. Strongly correlated materials<sup>113</sup>
3. Delocalization/self-interaction errors<sup>117,118</sup>

Dispersion interactions, are in principle a form of electron correlation, and a number of corrections to account for these effects have been developed.<sup>116</sup> The phrase ‘strongly correlated materials’ typically refers to transition-metal compounds where the electron-electron interactions associated with d and f orbitals result in significant correlation. Delocalization error refers to the tendency

of semilocal functionals to overbind configurations with fractionally occupied molecular orbitals, and is a consequence of the fact that the exchange-correlation energy arising from semilocal functionals is generally a smooth function of electron occupancy.<sup>117,118</sup> A canonical example of a system prone to delocalization errors is the stretched  $\text{H}_2^+$  ion.<sup>118</sup> The challenges associated with strongly correlated materials and delocalization errors can be mitigated by employing orbital-dependent methods, such as DFT+ $U$ , hybrid functionals (discussed below), and  $GW$  calculations (Section 2.2.3).

*Hybrid functionals.* Some of the errors of GGAs can be mitigated through the incorporation of exact exchange (i.e., Hartree-Fock energy). For example, the Heyd-Scuseria-Ernzerhof (HSE) functional takes the form<sup>119,120</sup>

$$(2.18) \quad E_{xc}^{\text{HSE}} = \alpha E_x^{\text{SR}}(\mu) + (1 - \alpha) E_x^{\text{PBE,SR}} + E_x^{\text{PBE,LR}}(\mu) + E_c^{\text{PBE}}.$$

Here  $E_x^{\text{SR}}$  is the short-range exact exchange energy,  $E_x^{\text{PBE,SR}}$  and  $E_x^{\text{PBE,LR}}$  are the short- and long-range contributions to exchange energy from the Perdew-Burke-Ernzerhof (PBE) GGA functional,<sup>121</sup> and  $E_c^{\text{PBE}}$  is the PBE correlation energy. The HSE functional family has two parameters: a screening parameter  $\mu$  which sets the length scale for separating short- and long-range interactions, and the mixing parameter  $\alpha$  which determines the fraction of short-range exact exchange incorporated.

A screening parameter of  $\mu = 0.2 \text{ \AA}^{-1}$  has been found to give a good description of solids.<sup>119,120</sup> At least two strategies for choosing the mixing parameter  $\alpha$  are widely used. One is to arbitrarily set  $\alpha = 0.25$ .<sup>119,122</sup> However, in many cases this does not yield an accurate description of defect states and band edge energies. A second strategy is to fit the mixing parameter to reproduce the fundamental energy gap of the material.<sup>122–124</sup> This approach is motivated by the fact that in order to correctly describe defect states, one must have a correct description of delocalized electrons and hence the band edge positions.

For most of the calculations in this work, we employ an HSE functional with a mixing parameter of  $\alpha = 0.48$ , obtained by fitting to the band gap of bulk  $\text{Li}_2\text{O}_2$ . Since there has been no experimental measurement of the bandgap, we fit the mixing parameter  $\alpha$  to the average of the GGA+ $G_0W_0$  and GGA+scGW band gaps (calculated at the  $\alpha = 0.25$  geometry); this choice is motivated by the fact that GGA+ $G_0W_0$  is known to underestimate gaps, while GGA+scGW (in the absence of vertex corrections) overestimates gaps.<sup>125,126</sup> We found that a mixing parameter of  $\alpha = 0.48$  reproduces the reference gap of 6.62 eV. Given the uncertainty in the true band gap, there is some uncertainty in the optimal value of  $\alpha$  and therefore quantities that are sensitive to its value. (Additionally the value of  $\alpha$  that reproduces the true band gap may not exactly reproduce the true band edges nor the hopping barrier.<sup>123</sup>) See Chapter 3 for additional discussion.

### 2.2.3 GW methods

There are three distinct energy gaps associated with a crystal:

1. The fundamental gap
2. The optical gap
3. The Kohn-Sham gap

The *fundamental gap* of a solid is the amount of energy required to excite an electron from the valence band to the conduction band, and can be expressed as:

$$(2.19) \quad \Delta_{\text{fundamental}} = E(N+1) + E(N-1) - 2E(N)$$

where  $E(N)$  is the ground state energy of the system with  $N$  electrons. This expression can be interpreted as follows: we start with two neutral systems, and move an electron from one system to the other. The *optical gap* is the lowest energy photon which the system can absorb, and in general can be smaller than the fundamental gap, for example due to excitonic effects.<sup>127</sup> Lastly, the *Kohn-Sham gap* refers to the difference between the eigenvalues of the lowest

unoccupied and highest unoccupied Kohn-Sham orbitals. The value of the Kohn-Sham gap will vary depending on the exchange-correlation functional used. However, it is important to note that the Kohn-Sham gap of the exact exchange-correlation functional is not the same as the fundamental or optical gaps.

The Kohn-Sham gaps calculated from DFT are in general much smaller than the fundamental gap. In some cases, such as crystalline germanium, semilocal functionals predict semiconductors to have no Kohn-Sham gaps.<sup>113</sup> Part of this discrepancy is due to the fact that the Kohn-Sham gap, even for the exact exchange-correlation functional, is not the same as the fundamental gap. However, the fundamental gap *can* be calculated directly in DFT. (Eq. (2.19) can be computed by finding the ground state energies  $E(N+1)$ ,  $E(N-1)$ , and  $E(N)$  of a large supercell with the appropriate number of electrons.) In practice, such calculations are rarely necessary: for most of the widely-used exchange-correlation functionals (LDA, GGA, and hybrid functionals), the fundamental gap is the same as the Kohn-Sham gap because these functionals do not contain a discontinuity in the potential with respect to occupation.<sup>128</sup>

The key point is that the underestimate of the fundamental gap by an exchange-correlation functional reflects a problem with that functional. Thus it is common practice to adjust parameters in functionals (such as the mixing parameter in hybrid functionals or Hubbard on-site Coulomb interaction<sup>113</sup>) to reproduce the correct fundamental gap. Since the fundamental gap is equivalent to the Kohn-Sham gap for these functionals, in practice one will typically fit the Kohn-Sham gap because it requires fewer calculations.

Such a fitting process requires an accurate reference value for the fundamental gap. Often, this reference band gap is taken from experimental data. But for many materials, experimental measurements of the band gap are not available. In these cases, one can fit the parameters to reproduce the fundamental gap predicted using a higher level of theory. *GW* methods are well-suited for this purpose. These methods are based on many-body theory and are related to, but not the same as DFT.

Underlying *GW* methods is the quasiparticle equation,<sup>129,130</sup>

$$(2.20) \quad \left\{ -\frac{\hbar^2}{2m} \nabla^2 + V_{\text{ext}}(\mathbf{r}) + V_{\text{H}}[n](\mathbf{r}) + \int \Sigma(\mathbf{r}, \mathbf{r}'; \varepsilon_i) d\mathbf{r}' \right\} \psi_i = \varepsilon_i \psi_i,$$

where  $\Sigma(\mathbf{r}, \mathbf{r}'; \varepsilon_i)$  is the self-energy operator. The eigenvalues of the quasiparticle equation physically represent energies for electron addition or removal, and hence the fundamental gap can be computed as a difference in quasiparticle energies. Note that Eq. (2.20), like the Kohn-Sham equation, is of the same form as the Schrödinger equation; however, the exchange-correlation potential  $V_{\text{xc}}$  has been replaced with the self-energy operator. Unlike the exchange-correlation potential, the self-energy operator is non-local and energy-dependent. This makes the quasiparticle equation substantially more complicated than the Kohn-Sham equation.

The quasiparticle equation is generally solved by using a suitable approximation for  $\Sigma(\mathbf{r}, \mathbf{r}'; \varepsilon_i)$ . Within the *GW* approximation, one can express the self-energy operator in terms of the single-particle Green's function  $G$  and the dynamically screened interaction  $W$ :<sup>129</sup>

$$(2.21) \quad \Sigma(\mathbf{r}, \mathbf{r}'; \varepsilon) \approx iG(\mathbf{r}, \mathbf{r}'; \varepsilon)W(\mathbf{r}, \mathbf{r}'; \varepsilon).$$

The task now is to determine  $G$  and  $W$ . These quantities can be expressed in terms of the quasiparticle wavefunctions, and so the problem is one of self-consistency. In the simplest approach ( $G_0W_0$ ), the DFT wavefunctions and eigenvalues are used to calculate  $G$  and  $W$  and the self-energy operator is considered as a perturbation to the Kohn-Sham potential. Further refinements can be made by using the wavefunctions and eigenvalues of the quasiparticle equation to make further updates to  $G$  and/or  $W$ . Following the notation of the Vienna ab initio Software Package,<sup>131</sup> several possible strategies are listed in Table 2.1.

**Table 2.1.** Summary of *GW* methods.

Name	Meaning
$G_0W_0$ ('single-shot' <i>GW</i> )	Neither $G$ nor $W$ is updated. <sup>131</sup>
$GW_0$	Eigenvalues are used to update $G$ . <sup>125,132</sup>
$GW$	Eigenvalues are used to update $G$ and $W$ . <sup>125,132</sup>
sc <i>GW</i> /QPsc <i>GW</i>	Eigenvalues and wavefunctions are used to update $G$ and $W$ . <sup>126</sup>

### 2.2.4 Computational tools: basis sets, pseudopotentials, and $k$ -points

*k*-points. For most of this work, we are concerned with the properties of infinite crystals. In principle such a system has an infinite number of electrons. However, by employing Bloch's theorem, one can make such problems tractable. Bloch's theorem<sup>133</sup> says that the eigenfunctions of a periodic Hamiltonian can be expressed as products of cell-periodic wavefunctions with plane waves:  $\psi(\mathbf{r}) = u(\mathbf{r})e^{i\mathbf{k}\cdot\mathbf{r}}$ . Here  $u(\mathbf{r} + \mathbf{R}) = u(\mathbf{r})$  for all integer combinations of lattice vectors  $\mathbf{R}$  and the wavevector  $\mathbf{k}$  lies in the Brillouin zone. Thus sums over wavefunctions can be expressed as integrals over the Brillouin zone. Such integrals can be numerically estimated by sampling the Brillouin zone at a finite number of  $k$ -points. A number of efficient methods exist for this purpose, such as Blöchl's tetrahedron method<sup>134</sup> or Gaussian smearing.

*Basis sets.* To represent the cell-periodic part of the wavefunction  $u$  numerically, one can expand  $u$  in terms of some set of basis functions  $\{\phi_j\}$ ,

$$(2.22) \quad u(\mathbf{r}) = \sum_{j=1}^M c_j \phi_j(\mathbf{r}).$$

Popular choices for the basis functions include localized functions derived from atomic orbitals and plane waves, although other methods, including finite-difference and finite-element methods, are also used.<sup>113</sup> In this work, plane-wave

basis sets are used, as these are particularly convenient for periodic systems. In this formalism, the basis functions are  $\phi_j(\mathbf{r}) = \exp(i\mathbf{g}_j \cdot \mathbf{r})$ .

Because  $u$  is periodic in the unit cell, we are concerned only with the countably infinite set of wavevectors  $\{\mathbf{g}_j\}$  that are also periodic in the unit cell. To reduce our basis set to a finite size, we include only the plane waves whose kinetic energy is less than a specified cutoff  $E_{\text{cut}}$ . That is, we restrict  $\mathbf{g}_j$  such that  $|\mathbf{g}_j + \mathbf{k}| < G_{\text{cut}}$ , where  $E_{\text{cut}} = \hbar^2 G_{\text{cut}}^2 / 2m_e$ . The planewave cutoff energy  $E_{\text{cut}}$  provides a measure of the quality of the basis set, with  $E_{\text{cut}} \rightarrow \infty$  corresponding to a complete basis set. Note that in this approach, the number of plane waves is different at each k-point.

*Pseudopotentials.* The direct solution of the Kohn-Sham equations using a plane-wave basis set is highly inefficient because a large basis set is needed to capture the rapid oscillations of the wavefunctions near the ions. The pseudopotential formalism provides a solution to this problem.<sup>113</sup> The local potential in a region near an ion core is replaced with a non-local potential, referred to as a pseudopotential. The Kohn-Sham equations are solved using this new Hamiltonian to obtain the pseudowavefunction. The magic of this method lies in the fact that there are many degrees of freedom in designing the pseudopotential, and so it is possible to construct a pseudopotential that yields the same scattering properties and the true potential, but produces a much smoother wavefunction. Consequently, the number of plane waves required is reduced.

The pseudopotential formalism can also be used to eliminate the degrees of freedom associated with the core electrons, as these typically do not play a major role in bonding. In this case, the pseudopotential represents the contribution of both the nucleus and core electrons to the Kohn-Sham potential.

Several classes of pseudopotentials have been developed, including norm-conserving,<sup>135</sup> ultrasoft,<sup>136</sup> and projector-augmented wave pseudopotentials.<sup>137</sup> As an illustrative example, we discuss briefly the case of norm-conserving

pseudopotentials. In the semilocal form, norm-conserving pseudopotentials can be written as

$$(2.23) \quad \hat{V}_{\text{SL}} = V_{\text{local}}(\mathbf{r}) + \sum_{lm} |Y_{lm}\rangle V_l(\mathbf{r}) \langle Y_{lm}|.$$

Clearly,  $\hat{V}_{\text{SL}}$  is a non-local operator. That is,  $\langle \psi_1 | \hat{V}_{\text{SL}} | \psi_2 \rangle$  can be non-zero even when  $|\psi_1\rangle$  and  $|\psi_2\rangle$  do not overlap in space. One can show that a  $\hat{V}_{\text{SL}}$  can be constructed to reproduce both the eigenvalues of the all-electron potential, as well as the scattering phase-shifts, if the norm-conservation condition holds:<sup>113,135</sup>

$$(2.24) \quad \int_{r < r_c} |\psi_{\text{PS}}(r)|^2 d\mathbf{r} = \int_{r < r_c} |\psi_{\text{AE}}(r)|^2 d\mathbf{r}.$$

Here  $\psi_{\text{PS}}$  is the eigenfunction of the pseudopotential,  $\psi_{\text{PS}}$  is the eigenstate of the all-electron potential, and  $r_c$  is the cutoff radius which defines the region in which the pseudopotential and all-electron potential differ.

### 2.2.5 Implementation

First-principles calculations were performed using the Vienna *ab initio* simulation package (VASP).<sup>138–141</sup> Occupancies were determined by a Gaussian smearing of width 0.1 eV, and the Brillouin zone was sampled with Monkhorst-Pack grids.<sup>142</sup> Projector-augmented wave (PAW) pseudopotentials were employed,<sup>137</sup> using a plane-wave basis set with a 400 eV cutoff for fixed-volume calculations and a 600 eV cutoff for relaxed-volume calculations. Ball-and-stick models were generated using VESTA.<sup>143</sup>

## 2.3 Point defects

### 2.3.1 Thermodynamics

Point defects are known to play a significant role in many important solid-state phenomena, including mass transport, charge transport, and nucleation.<sup>144–146</sup> In this section we discuss the statistical physics of point defects in solids. The principle goal is to relate macroscopic quantities (equilibrium concentrations and diffusion coefficients) to microscopic quantities that can be calculated from atomistic simulations.

We denote a defect as  $X_S^z$ , where  $X$  is the identity of the species,  $S$  is the site, and  $z$  is the equivalent charge. In the cases of substitutions and interstitials,  $X$  is the chemical symbol of the element. For vacancies and polarons, ‘V’ and ‘p’ are used. For vacancies and substitutions,  $S$  is the chemical symbol of the species which normally occupies the site. In the case of an interstitial the site is denoted by ‘i’, and for polarons, no site is denoted. The charge  $z$  represents the net charge of the defect, which is not necessarily the same as the charge state of the ion in a defect. Thus, for example,  $V_{Li}^-$  represents a negative lithium vacancy, i.e., the species formed by the removal of a  $Li^+$  ion.

Like all things in life, point defects are a balance between energy and entropy. The equilibrium defect concentration reflects a balance between the entropy gain associated with imperfections in the crystal lattice and the energy cost of introducing those imperfections. In the dilute limit, where the concentrations of defects is small compared to the concentration of lattice sites, the concentration of a defect  $X$  follows a Boltzmann distribution:

$$(2.25) \quad c_k^0 = M_k \exp[-E_k^0/k_B T].$$

Here the formation energy,  $E_k^0$  is the amount of free energy required to create a single defect of type  $k$ . In general, we calculate formation energies as

$$(2.26) \quad E_k^0 = E_k^{\text{DFT}} - E_{\text{bulk}}^{\text{DFT}} - \sum_i n_i \mu_i + z_k \varepsilon_F + \Delta E .$$

Here  $E_k^{\text{DFT}}$  and  $E_{\text{bulk}}^{\text{DFT}}$  are the ground-state DFT energies of supercells with and without a defect, respectively. The third term accounts for the addition/removal of atoms;  $n_i$  is the number of atoms of species  $i$  associated with the defect, and  $\mu_i$  is the chemical potential of that species. The fourth term accounts for the addition/removal of electrons;  $z_k$  is the equivalent charge associated with the defect and  $\varepsilon_F$  is the Fermi level (i.e., the chemical potential of electrons). The final term  $\Delta E$  represents a finite-size correction, in order to accelerate convergence of the formation energy with respect to supercell size. A number of finite-size corrections have been proposed.<sup>147–149</sup> In this work, we employ the Makov-Payne monopole correction.<sup>147</sup> This correction amounts to the electrostatic interaction energy of an infinite array of point charges embedded in a homogeneous compensating background.

The chemical potentials of the species are determined by the thermodynamic boundary conditions, i.e., which phases the host material is equilibrated with. The Fermi level (chemical potential of electrons), in principle, can lie anywhere between the host material's conduction and valence bands. If the size of the system is sufficiently large for any electric fields to be screened by mobile defects, then the Fermi level will be fixed by the electroneutrality constraint:

$$(2.27) \quad \sum_k z_k c_k^0 = 0 .$$

In general, this summation includes holes in the valence band and electrons in the conduction band. However, in wide-gap systems, the concentrations of these

species are often so low as to be negligible in comparison to other defects because the Fermi level is far from the band edges.

Note that in the above formalism, we have made no assumptions about the dimensionality of the system. Consequently Eqs. (2.25) and (2.26) apply both to defects in solids and defects at surfaces, except that the concentrations have dimensions of length<sup>-3</sup> in the case solids and length<sup>-2</sup> in the case of surfaces.

Although most of our calculations are applied to the solid state, we must consider gaseous O<sub>2</sub> to establish thermodynamic equilibrium. In an Li-O<sub>2</sub> electrode, we assume the chemical potential of oxygen to be one half the free energy of gaseous O<sub>2</sub> at 300 K and 0.1 MPa; this condition captures a scenario under which the electrode and the electrolyte (including dissolved oxygen) are in equilibrium with oxygen in the air or tank at an the same partial pressure. We calculate the free energy of oxygen as

$$(2.28) \quad G_{\text{O}_2} = E_{\text{O}_2}^{\text{DFT,corr}} + k_{\text{B}}T - TS_{\text{O}_2}^{\text{expt}},$$

where the  $k_{\text{B}}T$  term accounts for the  $pV$  contribution to free energy, and  $S_{\text{O}_2}^{\text{expt}}$  is the experimental entropy.<sup>12</sup> We have intentionally neglected the small contributions to the free energy due to the translational, rotational, and vibrational degrees of freedom because we are not including these terms in the bulk phases; this choice is intended to maintain some degree of error cancellation.

$E_{\text{O}_2}^{\text{DFT,corr}}$  represents the corrected ground-state energy of the O<sub>2</sub> molecule. Because DFT systematically overbinds gas-phase O<sub>2</sub> relative to solid oxides,<sup>89,150,151</sup> we correct the ground-state energy of the O<sub>2</sub> molecule using the experimental formation enthalpy of Li<sub>2</sub>O<sub>2</sub>. For defect calculations, we apply a correction to the energy of O<sub>2</sub> based on the experimental formation enthalpy of Li<sub>2</sub>O<sub>2</sub> at 300 K,  $\Delta H_{\text{f}}(\text{Li}_2\text{O}_2) = -6.57 \text{ eV}$ .<sup>12</sup>

$$(2.29) \quad E_0^{\text{DFT,corr}}(\text{O}_2) = E_0^{\text{DFT}}(\text{Li}_2\text{O}_2) - 2E_0^{\text{DFT}}(\text{Li}) - \Delta H_{\text{f}}(\text{Li}_2\text{O}_2).$$

This increases the energy of O<sub>2</sub> molecule by 0.78, 0.68, and 0.58 eV for the HSE functional with  $\alpha = 0$  (corresponding to the PBE GGA), 0.25, and 0.48. We note that prior studies have found that the error in formation energy varies to some degree between different alkali and alkaline-earth metal oxides, peroxides, and superoxides.<sup>89</sup> This indicates that in addition to errors in the ground state energy of the O<sub>2</sub> molecule, there is some error associated with the solid phases. However, we note that our results are not greatly sensitive to the choice of correction: for example, a 0.1 eV change in the O<sub>2</sub> correction changes the equilibrium hole polaron formation energy in crystalline Li<sub>2</sub>O<sub>2</sub> (see Chapter 3) by only 0.025 eV.

### 2.3.2 Kinetics

One of the main goals of this work is to connect microscopic simulations to macroscopic properties, i.e., transport characteristics. To this end, we use first-principles models to parameterize continuum-scale transport models. Central among these parameters are the diffusion coefficients and mobilities of defects. Transition-state theory allows one to estimate defect mobilities in terms of microscopic quantities. In the case of a dilute species in isotropic media, the diffusion coefficient can be expressed as<sup>145</sup>

$$(2.30) \quad D_k = \gamma a^2 \nu \exp(-E_a/k_B T),$$

where  $\gamma$  is a geometric factor relating to the lattice,  $\nu$  is the attempt rate, and  $E_a$  is the activation energy for defect motion between sites. The attempt rate, which represents the characteristic ionic vibrational frequencies, can be computed from the vibrational spectra of the transition state.<sup>152</sup> However, the fractional variation in  $\nu$  from system to system is generally small compared to the variation in the exponential term; thus the attempt rate is often assumed to be  $\sim 10^{13}$  Hz.<sup>145,152</sup>

Although the activation energy is in principle a free energy, entropic contributions represent only a small fraction in solids. Consequently we use the ground-state energy at the transition state as the activation energy. Standard geometry optimization algorithms are not helpful for finding the transition state

because it is a saddle point on the potential energy landscape. Other algorithms can be employed for finding the transition state, such as the nudged elastic band (NEB) method.<sup>153</sup>

Intimately related to the diffusion coefficients are defect mobilities. The defect diffusion coefficient  $D_k$  describes the Fickian diffusion of the defect, and in the dilute limit is related to the electrical mobility  $u_k$  by the Einstein relation,  $u_k = D_k/k_B T$ . Furthermore, the conductivity associated with a type of defect is related to the mobility as  $\sigma_k = e^2 z_k^2 u_k c_k$ .

It is important to distinguish between the different types of diffusion coefficients:<sup>144–146</sup>

1. *Defect diffusion coefficient.* The defect diffusion coefficient  $D_k$ , as defined in (2.30), describes the diffusion of defects of type  $k$ . For example,  $D_{\text{V}_\text{Li}}$  represents the defect diffusion coefficient of Li-ion vacancies.
2. *Self-diffusion coefficient.* The self-diffusion coefficient  $D_i^{\text{self}}$  describes the diffusion of chemical species  $i$ . For example  $D_{\text{Li}}^{\text{self}}$  represents the self-diffusion coefficient of lithium.
3. *Tracer diffusion coefficient.* Isotope diffusion experiments measure the tracer diffusion coefficient  $D_i^{\text{tracer}} = f D_i^{\text{self}}$ , where  $f$  is a correlation factor which accounts for the tendency for the direction of consecutive migrations to be correlated. This occurs, for example, in vacancy mediated diffusion.
4. *Chemical diffusion coefficient.* Ambipolar diffusion (the simultaneous diffusion of positive and negative species coupled via electrostatic interactions) is characterized by the chemical diffusion coefficient  $\tilde{D}$ , which is related to the defect diffusion coefficients of the positive and negative species.

## Chapter 3: Transport in intrinsic crystalline $\text{Li}_2\text{O}_2$

### 3.1 Introduction

As discussed in Section 1.3, charge transport through the  $\text{Li}_2\text{O}_2$  discharge product is anticipated to play a critical role in Li- $\text{O}_2$  batteries. In this chapter, we explore the mechanisms for electron and ion transport in bulk crystalline  $\text{Li}_2\text{O}_2$ . Although the defect chemistry of oxides has been extensively studied, peroxides have received much less scrutiny;<sup>69,70,74,81,154–157</sup> the limited availability of experimental data for these compounds motivates our use of first-principles methods for calculating these properties.

First-principles calculations by Hummelshøj et al. predicted that a high concentration of lithium vacancies in  $\text{Li}_2\text{O}_2$  will yield *p*-type conductivity associated with a depletion of electrons from the valence band.<sup>158</sup> Other studies have predicted that both holes and electrons will become self-trapped in  $\text{Li}_2\text{O}_2$ , forming small hole<sup>69</sup> and small electron<sup>156</sup> polarons. Although hole polarons were at first predicted to have very low hopping barriers,<sup>69</sup> a recent study examining the mobilities of these species in more detail has challenged this notion.<sup>74</sup>

As a step towards elucidating the impact and mechanism of charge transport in Li- $\text{O}_2$  cells, here we employ first-principles calculations to predict the conductivity of crystalline  $\text{Li}_2\text{O}_2$ . More specifically, we systematically predict the concentrations of different possible point defects and assess the mobilities of the dominant charge carriers. To obtain an accurate description of the electronic structure, hybrid functionals<sup>119,120</sup> and many-body perturbation theory (*GW*) methods<sup>126,131</sup> are employed. Our calculations indicate that charge transport in  $\text{Li}_2\text{O}_2$  is mediated by both the migration of negative lithium vacancies,  $V_{\text{Li}}^-$ , corresponding to missing  $\text{Li}^+$ , and the hopping of hole polarons,  $p^+$ . For ionic

transport, the barrier for  $V_{Li}^-$  migration, 0.33-0.39 eV, yields an ionic conductivity of  $\sim 4 \times 10^{-19}$  S/cm. The hopping of hole polarons was found to have in-plane and out-of-plane barriers of 0.42 and 0.71 eV, which are comparable to recent DFT+ $U$  calculations,<sup>74</sup> yet are much larger than those suggested by previous HSE06 calculations.<sup>69</sup> We predict an intrinsic electronic conductivity of  $\sim 5 \times 10^{-20}$  S/cm, which would classify  $Li_2O_2$  as an insulator. During charging, the partial delithiation of  $Li_2O_2$  is expected to increase the conductivity, with each overpotential increment of  $\sim 0.1$  V increasing the conductivity by an order of magnitude. Such an enhancement may explain why Li- $O_2$  electrodes that have been loaded with purchased  $Li_2O_2$  can be recharged at high overpotentials despite the low conductivity of  $Li_2O_2$ .<sup>110,159-161</sup> Our results suggest that recharge may occur via a two-stage process, with thin deposits decomposing at low potentials via electron tunneling, and thick deposits decomposing at moderately high potentials via polaron hopping. Therefore, strategies for enhancing bulk transport – or avoiding altogether it in place of transport via other pathways such as surfaces, grain boundaries, amorphous regions, *etc.* – should be explored. More generally, we discuss how the capability for electronic charge transport in metal-air discharge phases can be tied to the presence of a species that can change valence state, such as the  $O_2$  dimers in  $Li_2O_2$ . The presence or absence of such a species could explain why some non-aqueous metal-air chemistries are rechargeable, while others are not.

## 3.2 Methods

The crystal structure of  $\text{Li}_2\text{O}_2$ , shown in Figure 3.1, consists of alternating layers of trigonal prisms and octahedra/tetrahedra, with oxygen sites lying on the vertices of the polyhedra. One notable feature of the structure is the presence of covalently bonded  $\text{O}_2$  dimers. As we will describe later, the ability of these dimers to change charge state plays an important role in the defect chemistry and conductivity of  $\text{Li}_2\text{O}_2$ . All of the octahedra (Oct) and half of the trigonal prisms (TP) are occupied by lithium atoms.

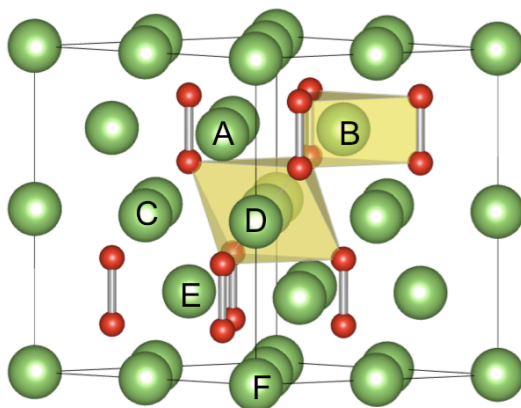


**Figure 3.1** Crystal structure of  $\text{Li}_2\text{O}_2$ , illustrated using a  $2 \times 2 \times 1$  expansion of the unit cell. Large green atoms are lithium, and small red atoms are oxygen. Polyhedra indicate the trigonal prismatic and octahedral coordination of the two unique Li sites.

Point defect formation energies were calculated for 23 unique species, including vacancies, divacancies, interstitials, and polarons. First principles calculations were performed with a  $3 \times 3 \times 2$  (144-atom) supercell. See Section 2.3 for details. Given that self-interaction errors inherent to semilocal functionals (e.g., GGAs) can lead to qualitatively incorrect descriptions of certain

defects,<sup>122,123,162</sup> our calculations employ the HSE hybrid functional<sup>119,120</sup> with a mixing parameter  $\alpha$  of 0.48, as discussed in Section 2.2.2. As discussed below, we also investigated the sensitivity of our results to the choice of mixing parameter. The chemical potential of oxygen was assumed to be fixed by equilibrium with oxygen in the atmosphere, while that of lithium was set by ion exchange with the anode,<sup>158</sup>  $\mu_{\text{Li}} = G(\text{BCC Li}) - eE$ , where  $E$  is the cell voltage and  $e$  the elementary charge. Note that the equilibrium potential for the Li-O<sub>2</sub> redox couple corresponds to the same thermodynamic boundary condition as isolated Li<sub>2</sub>O<sub>2</sub>,

$$(3.1) \quad \mu_{\text{Li}}^0 = \frac{1}{2} [G(\text{Li}_2\text{O}_2) - 2\mu_{\text{O}}].$$

### 3.3 Defect thermodynamics

Figure 3.2 shows the formation energies for the low-energy defects as a function of the Fermi level for isolated  $\text{Li}_2\text{O}_2$  (or equivalently, a cell whose potential is at the equilibrium Li-O<sub>2</sub> potential). Table 3.1 summarizes the equilibrium formation energies and concentrations for all defects examined. As shown in Figure 3.2, the dominant (i.e., lowest energy) positively charged species is the hole polaron,  $p^+$ . The hole polaron consists of a hole that is self-trapped at an oxygen dimer, reducing the formal charge on a peroxide ( $\text{O}_2^{2-}$ ) dimer by one to yield a superoxide ( $\text{O}_2^-$ ) dimer and an associated contraction of the covalent O-O bond.<sup>69,74</sup> The dominant negative defect species is the Li-ion vacancy (i.e., absence of a  $\text{Li}^+$  ion). As shown in Table 1, Li-ion vacancies at the two symmetry-distinct Li sites have similar energies, with  $V_{\text{Li}}^-$  (TP) being only 20 meV more stable than  $V_{\text{Li}}^-$  (Oct). The concentrations of the dominant charge carriers,  $p^+$  and  $V_{\text{Li}}^-$ , established by charge neutrality condition (Eq. (2.27)) have values of  $1 \times 10^7 \text{ cm}^{-3}$ , which is approximately three orders of magnitude less than the intrinsic carrier concentration in silicon at 300 K ( $\sim 10^{10} \text{ cm}^{-3}$ ).<sup>163</sup> To quantify the influence of the mixing parameter, we also performed calculations using the ‘standard’  $\alpha$  value of 0.25 (i.e., the HSE06 functional); this altered the equilibrium defect formation energies by only  $\sim 0.1$  eV or less. The influence of the mixing parameter is discussed in more detail below.

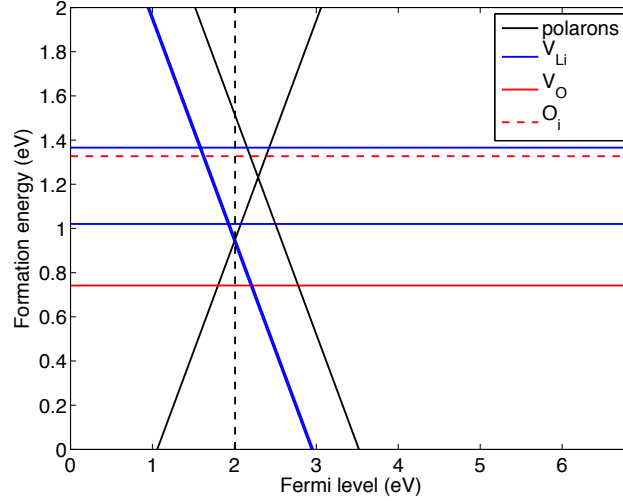


**Figure 3.2** Formation energies of low-energy defects in  $\text{Li}_2\text{O}_2$ . Positive defects have an upwards slope while negative defects have a downwards slope. The vertical dashed line indicates the position of the Fermi level that satisfies charge neutrality.

**Table 3.1** Equilibrium defect formation energies (eV) and concentrations ( $\text{cm}^{-3}$ ) in  $\text{Li}_2\text{O}_2$ .

$\text{p}^{2-}$	$3.12 (1 \times 10^{-30})$	$\text{V}_{\text{O}_2}^-$	$2.47 (1 \times 10^{-19})$
$\text{p}^-$	$1.51 (1 \times 10^{-3})$	$\text{V}_{\text{O}_2}^0$	$4.71 (2 \times 10^{-57})$
$\text{p}^+$	$0.95 (1 \times 10^7)$	$\text{V}_{\text{O}_2}^+$	$4.32 (1 \times 10^{-50})$
$\text{V}_{\text{Li}}^- (\text{O})$	$0.95 (3 \times 10^6)$	$\text{V}_{\text{O}_2}^{2+}$	$3.24 (9 \times 10^{-33})$
$\text{V}_{\text{Li}}^- (\text{TP})$	$0.93 (7 \times 10^6)$	$\text{O}_i^{2-}$	$4.55 (4 \times 10^{-54})$
$\text{V}_{\text{Li}}^0 (\text{O})$	$1.37 (4 \times 10^{-1})$	$\text{O}_i^-$	$4.34 (1 \times 10^{-50})$
$\text{V}_{\text{Li}}^0 (\text{TP})$	$1.02 (2 \times 10^5)$	$\text{O}_i^0$	$1.33 (5 \times 10^0)$
$\text{V}_{\text{Li}}^+ (\text{O})$	$2.05 (1 \times 10^{-12})$	$\text{O}_i^+$	$2.22 (5 \times 10^{-15})$
$\text{V}_{\text{Li}}^+ (\text{TP})$	$1.45 (1 \times 10^{-2})$	$\text{Li}_i^-$	$3.80 (1 \times 10^{-41})$
$\text{V}_{\text{O}}^-$	$3.58 (4 \times 10^{-38})$	$\text{Li}_i^0$	$2.51 (6 \times 10^{-20})$
$\text{V}_{\text{O}}^0$	$0.74 (2 \times 10^{10})$	$\text{Li}_i^+$	$1.69 (1 \times 10^{-6})$
$\text{V}_{\text{O}}^+$	$1.66 (9 \times 10^{-6})$		

Figure 3.2 also shows that the neutral oxygen vacancy is the most stable uncharged defect, with a formation energy of 0.74 eV. At first glance such a low formation energy may seem surprising because the creation of an oxygen vacancy requires the cleavage of an oxygen-oxygen bond. However, this cleavage results in the reduction of the remaining oxygen ion to a  $-2$  charge state, which is

energetically favorable. The second lowest energy neutral defect is the neutral lithium vacancy,  $V_{\text{Li}}^0$  ( $E_{V_{\text{Li}}^0} = 1.02$  &  $1.37$  eV for the two Li sites), which consists of a  $p^+ - V_{\text{Li}}^-$  bound pair. The binding energy  $\Delta E = E_{p^+}^0 + E_{V_{\text{Li}}^-}^0 - E_{V_{\text{Li}}^0}^0$  is  $0.53$  and  $0.86$  eV at the O and TP sites. A previous study<sup>69</sup> suggested that a hole polarons in  $\text{Li}_2\text{O}_2$  would be bound to lithium vacancies on the basis that the  $p^+ - V_{\text{Li}}^-$  binding is fairly strong. However, as can be seen from Table 3.1, the equilibrium concentrations of unbound  $p^+$  and  $V_{\text{Li}}^-$  are in fact higher than that of  $V_{\text{Li}}^0$  due to the entropy gain associated with dissociation.<sup>164</sup>

### 3.4 Defect mobilities

Conductivity in  $\text{Li}_2\text{O}_2$  can in principle arise from the migration of charged defects (ionic conductivity) and/or hopping of small polarons (electronic conductivity). The defect diffusion coefficient is calculated from Eq. (2.30), where we have assumed a geometric factor of  $\gamma = 1$ . We first consider the ionic conductivity associated with  $V_{\text{Li}}^-$  migration. Energy barriers calculated for five migration pathways calculated using the NEB method<sup>153</sup> are shown in Table 3.2.

**Table 3.2** Migration barriers for  $V_{\text{Li}}^-$  migration calculated using the NEB method at the GGA level of theory. Sites are labeled as in Figure 3.1.

Path	Barrier (eV)	Description
A→B	1.00	In-plane between TP sites.
C→D	1.06	In-plane between Oct sites.
A→E	2.34	Out-of-plane between TP sites.
D→F	1.60	Out-of-plane between Oct sites.
A→D	0.39/0.33	Between TP and Oct sites.

Because these calculations are computationally expensive, we optimized the migration pathway using the PBE GGA functional and report the barrier obtained at this level of theory;<sup>121</sup> this choice is justified by the fact that the unrelaxed barriers obtained with PBE were essentially the same as the unrelaxed barriers obtained with HSE, indicating that there is little sensitivity to the choice of functional. The lowest energy pathway corresponds to migration between adjacent octahedral and trigonal prismatic sites, with a barrier of 0.33 eV relative to the octahedral site and 0.39 eV relative to the trigonal prism site. Similar values have been found in prior calculations.<sup>158,165</sup> Setting  $E_a$  to the average of these two values yields an ionic conductivity of  $9 \times 10^{-19}$  S/cm and a defect diffusion coefficient of

$6 \times 10^{-9}$  cm<sup>2</sup>/s. Because this pathway allows for both in-plane and out-of-plane transport, the ionic conductivity is expected to be more or less isotropic.

Next we consider the electronic conductivity associated with hole polarons. In this case we evaluate the energy barrier associated with nearest neighbor hole polaron hopping. While previous studies treated all in-plane (i.e., within a basal plane) hopping paths as symmetry equivalent and all out-of-plane paths as symmetry equivalent,<sup>69,74</sup> a Jahn-Teller distortion due to the degeneracy of  $\pi_x^*$  and  $\pi_y^*$  molecular orbitals breaks this symmetry. This distortion lowers the polaron's symmetry from  $D_{3h}$  to  $C_{2v}$  and lowers the ground state energy by 22 meV. As a result of this symmetry breaking there are six symmetry inequivalent in-plane and four symmetry inequivalent out-of-plane paths, as well as a trivial in-place rotation. The adiabatic barriers for these paths based on a chain of linearly interpolated images<sup>69,156</sup> are shown in Figure 3.3.

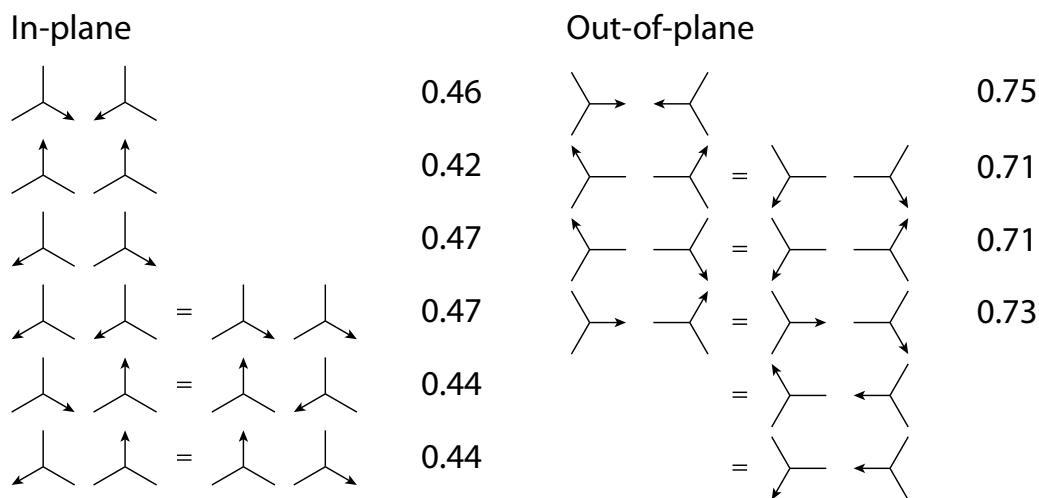


**Figure 3.3** Nearest neighbor hole polaron hopping paths. Each path is depicted by two glyphs which represent the initial and final polaron states. The three lines represent the directions of three nearest trigonal prismatic Li sites. The arrow indicates the direction of the Jahn-Teller distortion (i.e., which of the three O-Li bonds is contracted). The hopping direction is left to right, and symmetry equivalent paths are indicated by an equals sign. Hopping barriers calculated from a linear interpolation of images are given in eV.

All of the in-plane paths had similar barriers, and all of the out-of-plane paths had similar barriers. Additionally, there is a trivial in-place rotation path, for which we find an barrier of 5 meV. Attempts to optimize the geometry with the

NEB method did not lead to significant changes in the barrier height: after 189 optimization steps, the barrier height of the lowest energy in-plane path was reduced by only 0.04 eV.

Figure 3.4 compares the energy profiles for the lowest energy in-plane and lowest energy out-of-plane hopping paths, for which we find barriers of 0.42 and 0.71 eV, respectively. These values correspond to conductivities of  $5 \times 10^{-20}$  and  $1 \times 10^{-24}$  S/cm for in-plane and out-of-plane transport. To place the calculated conductivities in context, we note that the conductivity of other battery materials can be orders of magnitude higher: for example, in  $\text{LiFePO}_4$   $\sigma \sim 10^{-9}$  S/cm,<sup>166</sup> while the conductivity of a good insulator such as fused silica is similar to our predicted value for  $\text{Li}_2\text{O}_2$ .<sup>167</sup>

Regarding experiments, a recent study measuring the ionic and electronic conductivities of  $\text{Li}_2\text{O}_2$  arrived independently at qualitatively the same picture presented here: electronic conduction is mediated by hole polarons, and ionic conduction is mediated by negative lithium vacancies.<sup>81</sup> However, because the experimental sample was in the extrinsic regime – where defect concentrations are controlled by the presence of impurities – the measured electronic and ionic conductivities (at 100 °C) of  $10^{-12}$ - $10^{-11}$  S/cm and  $10^{-10}$ - $10^{-9}$  were significantly larger than those predicted here. Consequently, a direct comparison between experimental values and our calculations is not possible.

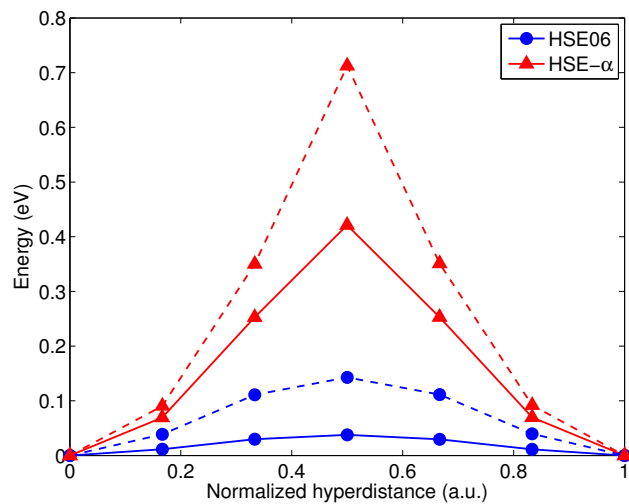


**Figure 3.4** Energy profiles for hole polaron hopping. Solid and dashed lines show in-plane and out-of-plane hopping.

A different study has estimated the conductivity of the discharge product in Li-O<sub>2</sub> cells to be 10<sup>-12</sup>-10<sup>-13</sup> S/cm based on electrochemical discharge/charge curves.<sup>79</sup> However, caution should be exercised in directly comparing these measurements to our calculations on crystalline Li<sub>2</sub>O<sub>2</sub>. First, the experiments were carried out at low capacities nominally resulting in Li<sub>2</sub>O<sub>2</sub> deposits thin enough (< 5 nm<sup>53,79</sup>) to support electron tunneling.<sup>53</sup> Second, it is well known that side reactions<sup>7,96,168,169</sup> can alter the composition (and presumably the conductivity) of the experimental discharge product, and also contribute to the observed current density.<sup>99,106</sup> Finally, morphological features in the experimental deposits (surfaces, grain boundaries, interfaces, amorphous regions, *etc.*<sup>42,68,84</sup>) may participate in transport, and these effects are not included in the present study.

### 3.5 Influence of the exchange-correlation functional

A recent DFT+ $U$  study ( $U = 6$  eV) also reported hopping barriers comparable to the present values (0.39 to 0.48 eV), and noted that the barrier values were sensitive to the choice of  $U$ .<sup>74</sup> As the mixing parameter  $\alpha$  in hybrid functionals is somewhat analogous to the  $U$  parameter in DFT+ $U$ , we likewise expect that the hopping barrier will also depend upon the choice of  $\alpha$ . This is demonstrated in Figure 3.4, which compares the energy profiles obtained with the two values of the mixing parameter explored:  $\alpha = 0.25$  (i.e., the HSE06 functional<sup>119,120</sup>) and 0.48. The HSE06 calculation yields much smaller barriers of 38 and 143 meV, in good agreement with Ong et al., who found barriers of 68 and 152 meV using the same functional.<sup>69</sup> To test geometry effects, we also calculated the  $\alpha = 0.48$  barrier using the  $\alpha = 0.25$  geometry. This lowered the in-plane and out-of-plane barriers by only 78 and 88 meV, indicating that the difference in barrier height between functionals is largely due to electronic structure effects.

As previously described, our predictions for the concentrations and hopping barriers for charge carriers in  $\text{Li}_2\text{O}_2$  are based on an optimized choice for the fraction of exact change,  $\alpha$ . Since other choices for  $\alpha$  are possible, it is important to examine the influence of the mixing parameter upon polaron energy levels and their (hopping) transition states. Figure 3.5 shows the energy levels (dashed lines) of the hole and electron polaron states, as determined from their formation energies referenced to the average electrostatic potential.<sup>123,170</sup> Three different values of  $\alpha$ , corresponding to increasing amounts of exact exchange, are considered: 0, 0.25, and 0.48. [The  $\alpha = 0$  case corresponds to the semilocal PBE GGA functional (i.e., no exact exchange),  $\alpha = 0.25$  corresponds to the HSE06 functional, and  $\alpha = 0.48$  corresponds to the functional that reproduces the average  $\text{Li}_2\text{O}_2$  bandgap predicted  $G_0W_0$  and self-consistent  $GW$  calculations (see Section 2.2.2).] In systems where the atomic geometry and wavefunction do not change

with  $\alpha$ , the functional form of the HSE family<sup>119,170</sup> dictates that the energy will vary linearly with  $\alpha$ . [Deviations from linearity indicate the degree to which the wavefunction (and geometry, if the atom coordinates are relaxed) is changing.] If the wavefunction and geometry are fixed, increasing amounts of exact exchange will increasingly penalize partially occupied orbitals;<sup>117</sup> that is, configurations with partially occupied orbitals should become higher<sup>118</sup> in energy with increasing  $\alpha$ . If the ‘correct’ value of  $\alpha$  is chosen, the penalty on partially occupied orbitals will exactly compensate for the self-interaction error from the semilocal exchange contribution.

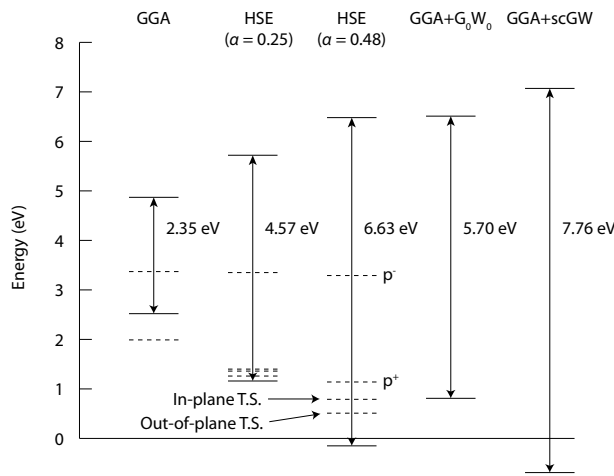


**Figure 3.5** Energy levels associated with the band edges, polaron ground states, and transition states for polaron hopping in  $\text{Li}_2\text{O}_2$  as a function of calculation method. Energies are referenced to the average electrostatic potential, which is assigned a value of zero. All energies were calculated using the  $\alpha = 0.25$  geometries, and finite-size corrections were not included. Transition states are not shown for the PBE functional.

The band edges for the three functionals, as well as those obtained with  $GW$  methods<sup>126,131</sup> are shown as solid lines in Figure 3.5. Given that  $G_0W_0$  and sc $GW$  band gaps typically bound the experimental band gap,<sup>125,126</sup> we expect that the positions of the  $G_0W_0$  and sc $GW$  band edges likewise bound the positions of the experimental band edges. (Extra effort was taken to ensure convergence of the  $GW$  band edge positions, as these typically converge more slowly than the band gap;<sup>123</sup> see Appendix.) Figure 3.5 shows that the valence band edge falls while the conduction band edge rises as  $\alpha$  increases. This is expected given that the valence

and conduction states involve the partial depletion/filling of molecular orbitals.<sup>117</sup> Note that this variation is essentially linear in  $\alpha$ , indicating that the valence and conduction band wavefunctions do not depend upon the choice of mixing parameter. The fact that the HSE06 valence band edge lies outside the range bounded by the *GW* edges suggests that a mixing parameter of  $\alpha = 0.25$  is not sufficient to compensate the self-interaction error in  $\text{Li}_2\text{O}_2$ . On the other hand, a mixing parameter of  $\alpha = 0.48$  places the valence band edge in better agreement with the *GW* calculations, indicating that this value gives a more realistic description of the electronic structure of  $\text{Li}_2\text{O}_2$ .

The data presented in Figure 3.5 illustrates a fundamental difference regarding the stability of hole polarons in  $\text{Li}_2\text{O}_2$  as described by the semi-local PBE ( $\alpha = 0$ ) vs. hybrid functionals ( $\alpha = 0.25, 0.48$ ). In both hybrid functionals the position of the valence band maximum (VBM) lies below the hole polaron level. In contrast, the hole polaron level lies above the VBM in PBE. Consequently, charge depletion in PBE generates delocalized holes in the top of the valence band, whereas localized holes (polarons) are predicted by the hybrid functionals. (In order to make an apples-to-apples comparison, the energy levels in Figure 3.5 were determined using single-point energy calculations performed on the  $\alpha = 0.25$  geometries. Releasing this constraint in PBE results in delocalization of the hole throughout the cell.) By comparing the PBE band edges to the *GW* band edges we can see that this instability is an artifact of self-interaction error.<sup>117,122,123</sup> This behavior is consistent with that of defects in other systems where semilocal functionals predict delocalized electrons, in contradiction to experimental measurements.<sup>122,162</sup>

Although PBE favors delocalized holes over hole polarons, Figure 3.5 shows that the hole polaron is actually more stable in PBE than in the hybrid functionals when referenced to the average electrostatic potential. This is because as the mixing parameter is reduced the hole polaron begins to spread out and hybridize with the valence band, resulting in partial occupancies of the oxygen p states and consequently a ground state energy that is too negative, as can be seen in Figure 3.6.

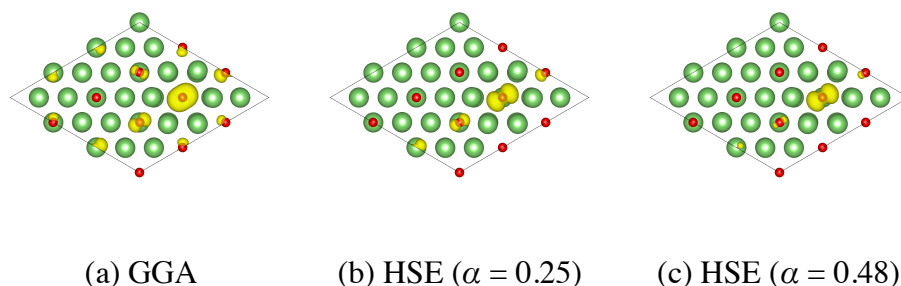


**Figure 3.6** Magnetization density isosurface of the hole polaron calculated with (a) PBE, (b) HSE ( $\alpha = 0.25$ ), and (c) HSE ( $\alpha = 0.48$ ). All three calculations shown here were performed at the  $\alpha = 0.25$  geometry. The polaron is viewed from along the  $c$  axis.

Although the energy levels in Figure 3.5 show that HSE06 ( $\alpha = 0.25$ ) favors hole polarons over delocalized holes, the difference in energy between these two may be smaller than errors associated with finite-size effects and numerical convergence (see Figure A.3); this raises some doubt as to the relative stability of delocalized holes and hole polarons in HSE06.<sup>69</sup>

As an aside, we note that the self-interaction errors inherent to GGAs are not limited to charged defects. Consider the neutral lithium vacancy,  $V_{\text{Li}}^0$ . The hybrid functionals predict this to consist of a  $p^+ - V_{\text{Li}}^-$  bound pair, whereas PBE instead delocalizes the hole over several nearby oxygen sites. The resulting partial occupancy of oxygen  $p$  states and concomitant self-interaction error causes PBE to overbind this defect by as much as 1 eV relative to the hybrid functionals (see Supplementary Information). Indeed, a prior study using a GGA functional found a formation energy for  $V_{\text{Li}}^0$  of 2.85 eV (referenced to bulk metallic Li), while a subsequent study using HSE06 found higher formation energies of 3.8 and 4.1 eV (TP and Oct sites, respectively). Our  $\alpha = 0.48$  calculations yield similar values when referenced to metallic Li (3.98 and 4.33 eV).

Regarding the energy barriers for polaron hopping, we note that these transition states exhibit partial occupancy because the polaron is split between two different sites. Consequently, the energy levels of the transition states are sensitive to the choice of mixing parameter. Figure 3.5 illustrates the energy levels of the transition states for the in-plane and out-of-plane hopping pathways

given in Figure 3.4. This analysis also explains the variation of the hopping barrier with the choice of  $U$ , which also penalizes partially occupied orbitals.<sup>74</sup> As discussed above, the HSE06 mixing parameter of 0.25 is not large enough to compensate for self-interaction errors in  $\text{Li}_2\text{O}_2$ . The agreement with DFT+ $U$  hopping barrier<sup>74</sup> (over the optimal range of  $U$  values based on experimental data) lends additional support to our choice of mixing parameter,  $\alpha = 0.48$ .

### 3.6 Discussion

It is important to consider how the predicted conductivity could impact the performance of a Li-O<sub>2</sub> cell. To this end, we compare against performance targets for Li-O<sub>2</sub> cells suggested in the literature.<sup>15</sup> We assume parameters based on the hypothetical bipolar plate-type Li-O<sub>2</sub> battery described by Karulkar and Adams,<sup>15</sup> with the additional assumption that the discharge product grows as a uniform film on a porous positive electrode with a specific surface area of 100 m<sup>2</sup>/g. Based on these assumptions, the discharge product should have a conductivity of  $\sim 2 \times 10^{-11}$  S/cm in order to achieve an  $iR$  drop of less than 0.1 V (see Appendix B). This target value is several orders of magnitude larger than the predicted intrinsic electronic conductivity ( $5 \times 10^{-20}$  S/cm), suggesting that charge transport through bulk (crystalline) Li<sub>2</sub>O<sub>2</sub> can be a performance-limiting factor. We note that the migration of negative lithium vacancies cannot sustain charge transport over long time periods because the positive electrode materials used in Li-O<sub>2</sub> cells (typically porous carbon) are effectively ion blocking.<sup>144</sup> For this reason we focus on the electronic conductivity provided by hole polaron hopping.

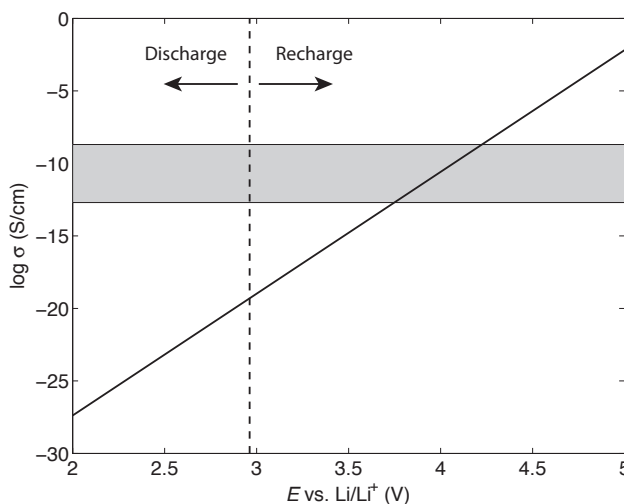


**Figure 3.7** Predicted electronic conductivity as a function of cell voltage. The dashed line indicates the equilibrium Li-O<sub>2</sub> potential. The gray shaded region indicates the target conductivity needed to meet performance requirements, as discussed in the text.

As the predicted conductivity of isolated  $\text{Li}_2\text{O}_2$  is much smaller than that of other battery materials<sup>166</sup> it is tempting to conclude that charge transport through bulk  $\text{Li}_2\text{O}_2$  is too small to play a meaningful role in a real cell. However, the conductivity is in principle not a fixed quantity, but can vary during discharge and charge because the cell potential impacts defect concentrations through variations in the lithium chemical potential. Figure 3.7 shows the predicted electronic conductivity as a function of cell voltage  $E$ . The conductivity increases exponentially with  $E$  because higher potentials favor delithiation (i.e., the creation of negative lithium vacancies, which are charge compensated by hole polarons). Under discharge conditions ( $E < E^0$ ) the bulk electronic conductivity is far below the target value, and therefore unable to supply significant charge transport. The fact that fairly high capacities and discharge product sizes are obtained in experiments<sup>11,171</sup> suggests two possibilities: (i.) morphological features may locally enhance the conductivity of the discharge product; (ii.) the oxygen reduction reaction (ORR) is not occurring at the  $\text{Li}_2\text{O}_2$  surface, but rather at the carbon support or catalyst.

Turning our attention to recharge, Figure 3.7 demonstrates that recharge conditions are more conducive to charge transport compared to discharge. That is, for each 119 mV of charging overpotential the conductivity increases by one order of magnitude, such that a 0.5 V recharge overpotential would enhance the conductivity by  $2 \times 10^4$ , and a 1 V overpotential would enhance it by a factor of  $3 \times 10^8$ , bringing the intrinsic electronic conductivity close to the targeted values (grey region in Figure 3.7). This effect results from an increase in the concentration of  $p^+$  and  $V_{\text{Li}}^-$  charge carriers at higher potentials. These results suggest that hole polaron hopping may be rapid enough to account for the observed rechargeability of bulk  $\text{Li}_2\text{O}_2$  particles at moderately high potentials.

Our prediction that fairly large overpotentials are needed to activate charge transport is in qualitative agreement with the high (3.5 to 4.2 V), yet relatively flat potential profiles obtained upon the charging of electrodes packed with purchased  $\text{Li}_2\text{O}_2$  powders.<sup>110,159–161</sup> On the other hand, much lower potentials have been

observed upon the initial charging of cells with thin films of  $\text{Li}_2\text{O}_2$ ;<sup>80</sup> in this case charge transport may be facilitated by electron tunneling<sup>53,80</sup> or the presence of a space-charge layer. (We note that impurities in the reference  $\text{Li}_2\text{O}_2$  samples could also influence charging behavior.<sup>110</sup>) Recent experiments have demonstrated that  $\text{Li-O}_2$  cells can concurrently form both thin *and* thick deposits.<sup>42,52</sup> By combining the electron tunneling narrative with our prediction of enhanced polaronic conductivity at higher potentials we arrive at the following two-stage process linking charge transport, particle morphology, and overpotentials during recharge. Charging will initiate at low potentials due to the dissolution of thin  $\text{Li}_2\text{O}_2$  deposits or decomposition at/near the  $\text{Li}_2\text{O}_2$ /electrolyte/carbon three-phase boundary. Charging will then conclude at high potentials where thick deposits decompose via polaron hopping. Side reactions involving the electrolyte or carbon support may of course introduce further complications.<sup>7,168,169</sup>

## Chapter 4: Amorphous $\text{Li}_2\text{O}_2$

### 4.1 Introduction

Although electrochemically formed  $\text{Li}_2\text{O}_2$  is often presumed to be crystalline, recent experiments have suggested the presence of an amorphous phase following battery discharge.<sup>42,47,48,54</sup> For example, Jung et al. identified amorphous  $\text{Li}_2\text{O}_2$  in the discharge product using selected area electron diffraction (SAED);<sup>54</sup> more recent X-ray diffraction (XRD) measurements have found evidence for the formation of ‘quasi-amorphous’  $\text{Li}_2\text{O}_2$  films at relatively high current densities.<sup>42</sup> Additionally, certain promoters/catalysts have also been reported to facilitate the formation of noncrystalline<sup>48</sup> or nanocrystalline<sup>47</sup>  $\text{Li}_2\text{O}_2$ . The formation of amorphous  $\text{Li}_2\text{O}_2$  in  $\text{Li}-\text{O}_2$  cells should not come as a surprise, as amorphous solids are often observed during the precipitation of solids.<sup>61,62</sup> This phenomenon has been interpreted on the basis of Ostwald's rule, which states that less stable phases tend to form before more stable phases during precipitation.<sup>63</sup>

The aforementioned reports of a- $\text{Li}_2\text{O}_2$  are noteworthy because the degree of crystallinity of the discharge product could have important implications for cell performance. In particular, prior studies have proposed that an amorphous phase having enhanced transport properties<sup>47,48</sup> could make for a desirable discharge product, given that the low conductivity of crystalline  $\text{Li}_2\text{O}_2$  (see Chapter 3) is expected to limit capacity and/or rate capability.<sup>53,68–70,73,81,82,84,156</sup> Prior density functional theory calculations predicted that amorphous  $\text{Li}_2\text{O}_2$  may be electronically conductive, and a conductive network of amorphous grain boundaries in the discharge product was suggested to account for the low overpotentials observed during the cycling of a novel  $\text{Li}-\text{O}_2$  cell.<sup>47</sup>

Taken together, these observations motivate the question: ‘What are the properties of amorphous  $\text{Li}_2\text{O}_2$ ?’ We address this question here using first-principles calculations. A series of amorphous  $\text{Li}_2\text{O}_2$  structures were generated

using melt-and-quench *ab initio* molecular dynamics, and the defect chemistry of a model at the energetically preferred density was subsequently characterized. In contrast to earlier studies,<sup>47</sup> we find that amorphous  $\text{Li}_2\text{O}_2$ , like crystalline  $\text{Li}_2\text{O}_2$ , is a wide band-gap insulator. Nevertheless, amorphous  $\text{Li}_2\text{O}_2$  exhibits a substantial increase in the mobility and concentration of lithium vacancies, and a more modest but still appreciable increase in the electronic conductivity. We speculate that the improved transport properties may make a- $\text{Li}_2\text{O}_2$  a more desirable discharge product than c- $\text{Li}_2\text{O}_2$ , due to its potential to reduce charging overpotentials and increase voltaic efficiency.<sup>42,47,48</sup>

## 4.2 Methods

Melt-and-quench *ab initio* molecular dynamics (AIMD)<sup>172</sup> using the temperature schedule depicted in Figure 4.1 were performed to generate amorphous structures of  $\text{Li}_2\text{O}_2$ . The procedure begins with crystalline  $\text{Li}_2\text{O}_2$  at  $T = 300$  K, followed by step-wise increases in temperature to a maximum of 3000 K. The temperature is then reduced following a similar schedule, ending at 300K with an amorphous structure. Each temperature increment was run for 1.8 ps under isothermal (NVT) conditions using the PBE GGA functional. The entire procedure consisted of 15 stages with a total simulation time of 27 ps. An MD step time of 3 fs was used for temperatures of 300-1500 K, and was reduced to 2 fs for the higher temperatures steps (2000-3000 K). The Nosé thermostat<sup>173</sup> was employed with a mass of  $\sim 50$  amu  $\cdot \text{\AA}^2$  (SMASS = 0.30).

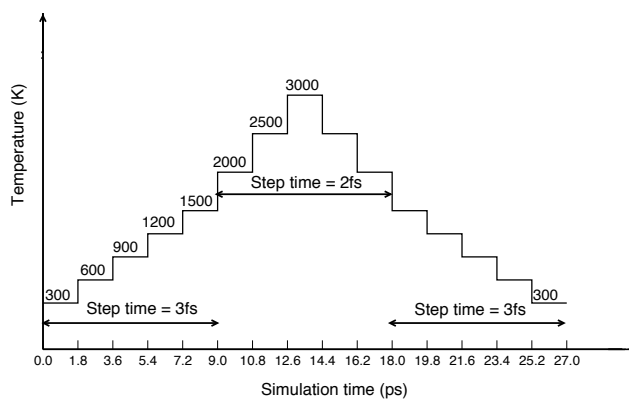


**Figure 4.1** Temperature profile used for melt-and-quench AIMD. The number on each step indicates the temperature used for that portion of the run. The MD time step is set at 2 fs for 300-1500 K and at 3 fs for 2000-3000 K.

As  $\text{Li}_2\text{O}_2$  has been observed to thermally decompose to  $\text{Li}_2\text{O}$  (solid) +  $\text{O}_2$  (gas) in the range of 468 – 621 K,<sup>12,174</sup> it is conceivable that the melt-and-quench procedure (even with the short simulation times used here) could yield a mixed valence phase consisting of amorphous  $\text{Li}_2\text{O}_2$ ,  $\text{Li}_2\text{O}$ , and  $\text{O}_2$  (or  $\text{LiO}_2$ ), rather than the desired amorphous peroxide. In fact, preliminary AIMD runs confirmed that

the O-O bond within the peroxide dimers dissociates at temperatures as low as 900K. To prevent this, the O-O bond distance was constrained during the first 14 stages in the melt-and-quench procedure. (The structures used as starting points for the melt-and-quench procedure were optimized and, depending on the lattice constants (see below), the relaxed O-O bond lengths were between 1.56-1.58 Å.) This constraint did not prevent rigid translation or rotation of the dimers, and was released during the final annealing stage at  $T = 300$  K. Constraining the O-O bond length is essential to obtaining an amorphous phase in which oxygen remains in the desired peroxide-like charge state of  $O_2^{2-}$ , as discussed in more detail below.

The density of a- $Li_2O_2$  was determined by repeating the melt-and-quench procedure on five simulation supercells with different densities. These models were based on a  $4 \times 4 \times 2$  supercell of c- $Li_2O_2$  with lattice constants expanded by 0%, 2%, 4%, 7%, and 11%, relative to the original cell size ( $a = 12.56$  Å,  $c = 15.33$  Å). The cell shape and volume was held constant during the MD runs. The resulting a- $Li_2O_2$  structures were subsequently optimized (including atom positions, cell shape, and cell volume) using an energy cutoff of 600 eV at the GGA level of theory. An additional a- $Li_2O_2$  structure was generated for studying intrinsic defects. This structure had an initial lattice constant expansion of 2%, which as described below yields a minimum in the energy-volume curve. This model was prepared using the procedure outlined above, except that the O-O bond constraints were released during the final two temperature segments of the melt-and-quench MD. The lattice constants for this model were subsequently optimized with the HSE functional.

In order to determine the concentrations of point defects, we perform calculations on several sites in the simulation cell for each type of defect considered (e.g.,  $V_{Li}^-$ ). We assume that the distribution of formation energies sampled by this approach is representative of the distribution for all sites in an amorphous phase. Thus we estimate the equilibrium concentrations of defects of type  $k$  as:

$$(4.1) \quad c_k^0 = \frac{1}{V} \frac{N_k}{N'_k} \sum_j \exp[-E_{k,j}^0 / k_B T],$$

where  $V$  is the simulation cell volume,  $N_k$  is the total number of available defect sites in the cell,  $N'_k$  is the number of defect sites sampled,  $E_{k,j}^0$  is the formation energy of a defect of type  $k$  at site  $j$  (Eq.(2.26)), and the sum runs over all defect sites sampled.

Activation energies for vacancy migration and polaron hopping were calculated using 5 images between defect sites. For vacancy migration, the images were relaxed using the nudged elastic band (NEB) method<sup>153</sup> for 30 iterations using the PBE GGA level of theory. For this calculation the optimized PBE GGA lattice constants and geometries were used. The use of PBE GGA here is justified by our previous calculations on crystalline  $\text{Li}_2\text{O}_2$ , where we found that PBE GGA and HSE yielded very close vacancy migration barriers.<sup>70</sup> Furthermore, as shown in the Supporting Information, the relative stabilities of the vacancy sites in PBE GGA and HSE are in good agreement. For hole polaron hopping, we performed single-point calculations on geometries that were linearly interpolated; this is motivated by our calculations on crystalline  $\text{Li}_2\text{O}_2$ ,<sup>70</sup> which showed that relaxation had little effect on the hole polaron hopping barrier but that the use of a hybrid functional was necessary.

## 4.3 Results

### 4.3.1 Bulk properties

The structural and energetic properties of the five candidate a-Li<sub>2</sub>O<sub>2</sub> models are summarized in Table 4.1. Overall, the total energy does not strongly depend upon the density: only ~50 meV per formula unit separate the models having the highest and lowest densities. The most stable structure identified is the one with an initial 2% increase in the lattice constants. This structure is illustrated in Figure 4.2, which shows the random distribution of O-O dimers and Li cations. The density of this a-Li<sub>2</sub>O<sub>2</sub> model is 2.119 g/cm<sup>3</sup>, which is 8.9% less than the calculated density of c-Li<sub>2</sub>O<sub>2</sub>. (The density of c-Li<sub>2</sub>O<sub>2</sub> is calculated to be 2.327 g/cm<sup>3</sup>, in good agreement with the experimental value of 2.371 g/cm<sup>3</sup>.<sup>175</sup>) The O-O bond in the most stable a-Li<sub>2</sub>O<sub>2</sub> model is 1.53 ± 0.02 Å, which is almost the same as in c-Li<sub>2</sub>O<sub>2</sub> (1.55 Å).

**Table 4.1** Structural parameters and relative energies for five candidate models for amorphous Li<sub>2</sub>O<sub>2</sub>.  $V_i$  refers to the volume of the amorphous cell before melt-and-quench *ab initio* MD (MQMD), and  $V_f$  refers to the volume after the completion of MQMD and subsequent relaxations.  $\Delta E$  is the PBE GGA energy per formula unit relative to c-Li<sub>2</sub>O<sub>2</sub>.

Initial increase in lattice constants	$V_i$ (Å <sup>3</sup> )	$V_f$ (Å <sup>3</sup> )	$\rho_f$ (g/cm <sup>3</sup> )	$\Delta E$ (eV per Li <sub>2</sub> O <sub>2</sub> f.u.)
0%	2095	2297	2.122	0.290
2%	2228	2301	2.119	0.274
4%	2362	2366	2.061	0.301
7%	2572	2452	1.988	0.318
11%	2871	2608	1.870	0.326

The energy of this most stable a-Li<sub>2</sub>O<sub>2</sub> model is 0.27 eV per formula unit higher than crystalline Li<sub>2</sub>O<sub>2</sub>. This energy difference would therefore result in an equilibrium voltage for a-Li<sub>2</sub>O<sub>2</sub> that is 0.14 V lower than for c-Li<sub>2</sub>O<sub>2</sub>,<sup>12</sup> 2.96 V vs. Li/Li<sup>+</sup>. Considering that the discharge potentials in most Li-O<sub>2</sub> cells are typically

several tenths of an eV below the equilibrium potential for c-Li<sub>2</sub>O<sub>2</sub>, formation of a-Li<sub>2</sub>O<sub>2</sub> appears to be thermodynamically plausible.

Structural analysis on the low-energy a-Li<sub>2</sub>O<sub>2</sub> model was performed by calculating the pair correlation function (Figure 4.2) during the last 1.8 ps of the melt-and-quench procedure ( $T = 300$  K). The distribution of Li-O nearest-neighbor distances reaches a maximum at 1.91 Å, followed by a valley at 2.51 Å. Integrating the area between 0 to 2.51 Å, we arrive at an average Li-O coordination number (CN) of 5.5. (Since the number of Li and O atoms is the same, the average coordination number of Li by O equals the average coordination number of O by Li.) This value is slightly lower than the coordination number in crystalline Li<sub>2</sub>O<sub>2</sub> of six, indicating that some Li and O sites are on average slightly undercoordinated in the amorphous phase.

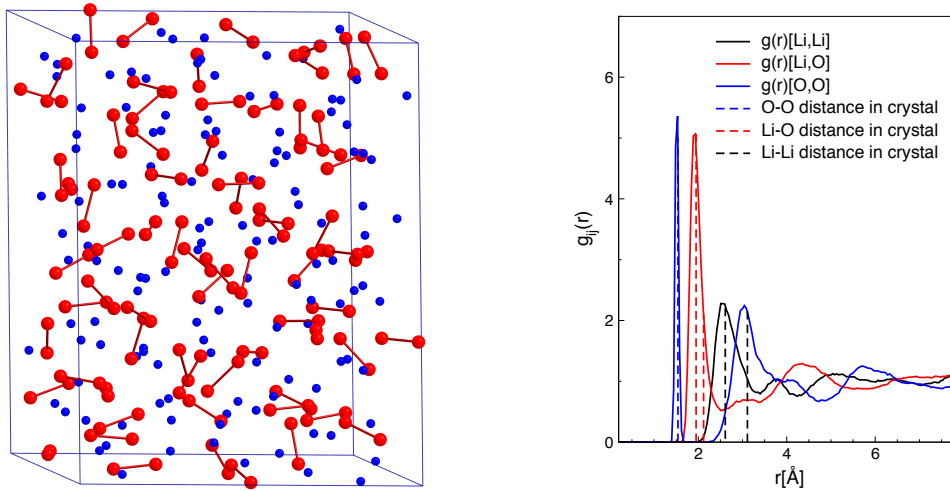


**Figure 4.2** Structure of amorphous Li<sub>2</sub>O<sub>2</sub>. Left: Ball-and-stick model of amorphous Li<sub>2</sub>O<sub>2</sub>. Blue and red spheres represent Li and O atoms, respectively. Right: Pair correlation function for the lowest-energy amorphous Li<sub>2</sub>O<sub>2</sub> structure. Dashed lines mark the inter-atomic distances in crystalline Li<sub>2</sub>O<sub>2</sub> at 0 K.

Figure 4.3 compares the density of states for the lowest-energy amorphous model and crystalline Li<sub>2</sub>O<sub>2</sub> at the HSE level of theory ( $\alpha = 0.48$ ). The HSE band gap for our a-Li<sub>2</sub>O<sub>2</sub> model was calculated to be 4.70 eV, essentially the same as for c-Li<sub>2</sub>O<sub>2</sub>. These results differ from those of Lu et al.,<sup>47</sup> wherein a model of amorphous Li<sub>2</sub>O<sub>2</sub> was found to be metallic. We attribute this difference to the fact that Lu et al. did not constrain O-O bonds during annealing. Consequently, some of the O-O bonds broke and a mixed-valence Li<sub>2</sub>O<sub>2</sub>/Li<sub>2</sub>O/LiO<sub>2</sub> phase was formed,

presumably containing a mixture of  $\text{O}_2^-$ ,  $\text{O}_2^{2-}$ , and  $\text{O}^{2-}$  anions. In contrast, in our model dissociation of oxygen dimers is prohibited due to constraints applied to the O-O bond. Consequently, our model represents a true peroxide, containing only one anionic species,  $\text{O}_2^{2-}$ . Recent isotopic-labeling experiments found that more than 98% of the O-O bonds remain undissociated during a discharge/charge cycle,<sup>176</sup> suggesting that our choice to constrain the O-O bonds will yield a model that better represents the Li-O<sub>2</sub> discharge product. (Additionally, the small portion of oxygen which has been dissociated may reside in lithium carbonate or other side reaction products, and not in the peroxide itself.) Also we note that the predictions of metallic behavior in Lu et al.<sup>47</sup> were based on PBE GGA calculations, which in some cases erroneously predict metallic behavior in semiconductors due to the ‘band gap problem’.<sup>113</sup> For example, our own calculations find that the PBE GGA predicts LiO<sub>2</sub> (PNNM space group) to be metallic, whereas hybrid functional calculations using the HSE functional predict semiconducting behavior.

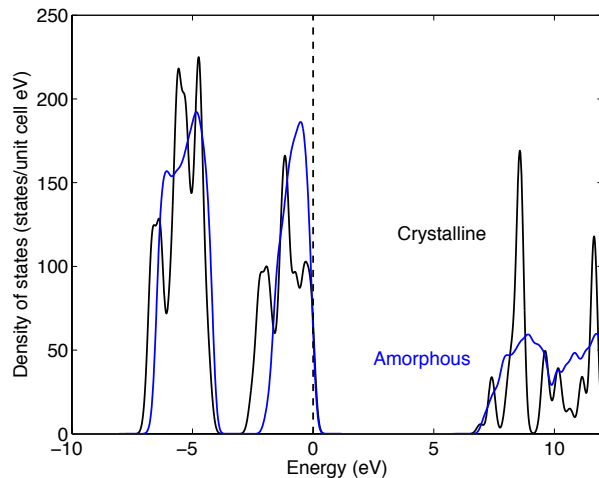


**Figure 4.3** Density of states for c-Li<sub>2</sub>O<sub>2</sub> and a-Li<sub>2</sub>O<sub>2</sub> calculated by HSE ( $\alpha = 0.48$ ). The energy scale is relative to the valence band maximum.

### 4.3.2 Defect chemistry

In order to estimate the conductivity of the amorphous phase, we have calculated the formation energies and mobilities for several intrinsic defects in one of our a-Li<sub>2</sub>O<sub>2</sub> models using the HSE hybrid functional, following the methods outlined in Section 2.3. Figure 4.4 shows the formation energies of hole polarons ( $\text{p}^+$ ),

negative lithium vacancies ( $V_{\text{Li}}^-$ ), and neutral oxygen vacancies ( $V_{\text{O}}^0$ ). These species represent the dominant positive, negative, and neutral defects in c- $\text{Li}_2\text{O}_2$ , as discussed in Chapter 3.<sup>70,81</sup> In the present work we restrict ourselves to  $p^+$ ,  $V_{\text{Li}}^-$ , and  $V_{\text{O}}^0$  because our previous calculations on crystalline  $\text{Li}_2\text{O}_2$  showed that the other defects generally have much higher formation energies.

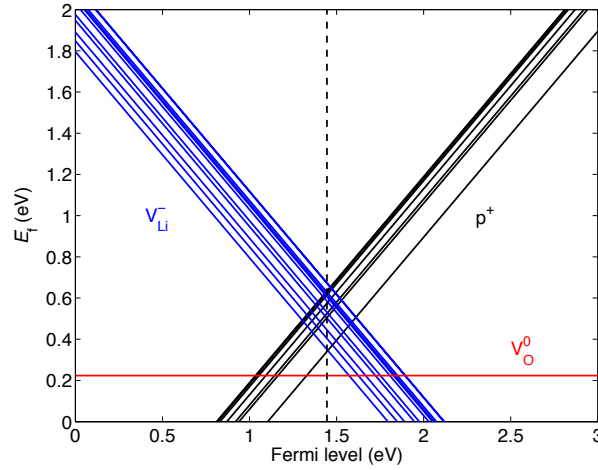


**Figure 4.4** Formation energies of point defects and polarons in a- $\text{Li}_2\text{O}_2$  as a function of the Fermi level, relative to the valence band maximum. A dashed vertical line indicates the Fermi level position that satisfies the charge neutrality condition.

Table 4.2 shows the calculated equilibrium formation energies for defects in amorphous and crystalline  $\text{Li}_2\text{O}_2$ . Our crystalline phase defect formation energies are in good agreement with those we reported previously, and the small differences can be attributed to the larger (256-atom) supercell used in the present work. The formation energies of the three types of defects considered are substantially lower in the amorphous phase than in the crystalline phase.  $V_{\text{O}}^0$  defects are predicted to be the lowest energy defect in both amorphous and crystalline  $\text{Li}_2\text{O}_2$ . The equilibrium concentration of  $V_{\text{O}}^0$  in a- $\text{Li}_2\text{O}_2$  is  $1 \times 10^{19} \text{ cm}^{-3}$ , while in c- $\text{Li}_2\text{O}_2$  it is only  $5 \times 10^9 \text{ cm}^{-3}$ . As previously mentioned, these defects are electrically neutral, and should not play a significant role in charge transport; therefore we focus on  $p^+$  and  $V_{\text{Li}}^-$  for the remainder of this study.

**Table 4.2** Comparison of formation energies of point defects and polarons in a-Li<sub>2</sub>O<sub>2</sub> with those in c-Li<sub>2</sub>O<sub>2</sub>. Calculations were performed at the HSE level of theory ( $\alpha = 0.48$ ).

Defect type	Formation energy in c-Li <sub>2</sub> O <sub>2</sub> (eV)	Formation energy in a-Li <sub>2</sub> O <sub>2</sub> (eV)
V <sub>Li</sub> <sup>-</sup>	1.04 (octahedral)	0.58, 0.63, 0.40, 0.67, 0.67, 0.61,
	0.98 (trigonal prismatic)	0.53, 0.35, 0.45, 0.50, 0.61
p <sup>+</sup>	1.00	0.34, 0.58, 0.63, 0.61, 0.51,
		0.53, 0.63
V <sub>O</sub> <sup>0</sup>	0.78	0.22

We find the equilibrium concentration of p<sup>+</sup> and V<sub>Li</sub><sup>-</sup> in a-Li<sub>2</sub>O<sub>2</sub> to be  $8 \times 10^{15} \text{ cm}^{-3}$ , while in c-Li<sub>2</sub>O<sub>2</sub> it is only  $2 \times 10^6 \text{ cm}^{-3}$ . This enhancement in the defect concentrations in a-Li<sub>2</sub>O<sub>2</sub> suggests that transport properties may differ significantly from the crystalline phase, depending on the defect mobility. The variation in formation energy across different V<sub>Li</sub><sup>-</sup> and p<sup>+</sup> sites is about 0.3 eV. This variation presumably arises from differences in the local environment of the sites; however, our analysis of the formation energies of different V<sub>Li</sub><sup>-</sup> sites suggests only a weak connection to coordination number.

To estimate the conductivity we have calculated migration barriers for lithium vacancies and the adiabatic hopping barriers for hole polarons. The lithium migration barriers were calculated using the NEB method.<sup>153</sup> Our previous calculations on c-Li<sub>2</sub>O<sub>2</sub> revealed that the use of a hybrid functional had little impact on the V<sub>Li</sub><sup>-</sup> migration barriers compared to semi-local functionals.<sup>70</sup> On the other hand, for polaron hopping the use of hybrid functionals was determined to be necessary. Consistent with these earlier studies, here we employ the PBE GGA functional to estimate barriers for vacancy migration and HSE for polaron hopping.

Figure 4.5 shows the vacancy diffusion path considered, which consists of 10 migrations between 11 adjacent Li sites that traverse the a-Li<sub>2</sub>O<sub>2</sub> cell. The specific pathway examined here is not intended to represent an actual diffusion path. Rather it is employed to sample the ensemble of possible migration barriers

typical of diffusion within an amorphous system. The energy barriers for these steps are summarized in Table 4.3. A fairly wide range of migration barriers were found, from 0 to 0.51 eV. The  $V_{\text{Li}}^-$  migration barriers in c- $\text{Li}_2\text{O}_2$  (0.3-0.4 eV)<sup>70</sup> fall within this range. However, many of the barriers in a- $\text{Li}_2\text{O}_2$  are significantly lower than those in the crystalline phase; as discussed below, this leads to an enhancement in ionic conductivity. We found little correlation between migration barrier height and the migration distances.

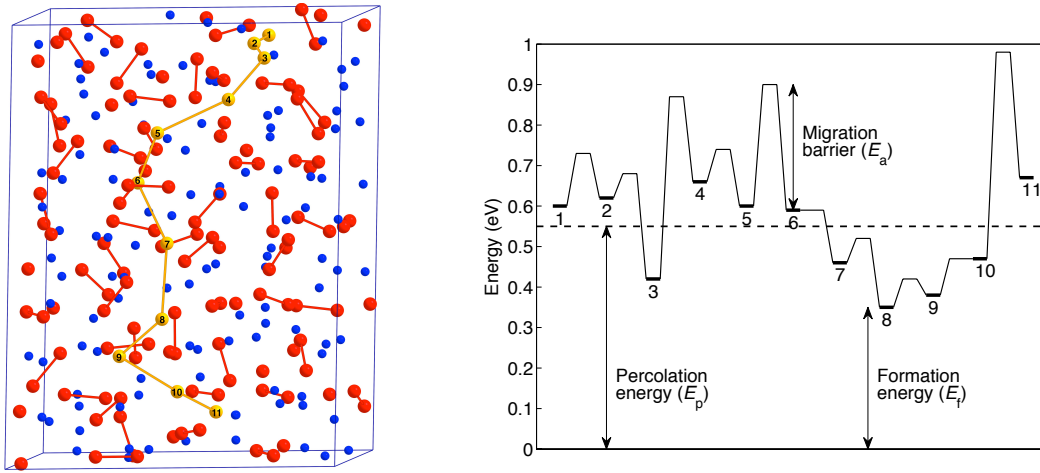


**Figure 4.5** Pathway used to estimate Li vacancy migration rate. Left: Ball-and-stick model showing migration pathway in yellow. Right: Energy profile for  $V_{\text{Li}}^-$  migration along the above pathway, with energies in eV. Thick lines show the formation energies for vacancy sites and thin lines show the transition state energies along migration pathways. The horizontal dashed line shows the percolation energy. The Li sites are numbered according to the order of their appearance in Table 4.2.

**Table 4.3** Migration barriers between vacancy sites in amorphous  $\text{Li}_2\text{O}_2$ .  $E_a^+$  and  $E_a^-$  represent the forward and backward barriers for vacancy migration, respectively.

Path	$E_a^+ / E_a^-$ (eV)	Path	$E_a^+ / E_a^-$ (eV)
1-2	0.13/0.11	6-7	0.00/0.13
2-3	0.06/0.26	7-8	0.06/0.18
3-4	0.45/0.21	8-9	0.07/0.03
4-5	0.08/0.14	9-10	0.09/0.00
5-6	0.30/0.31	10-11	0.51/0.30

We would like to relate the microscopic quantities from our model (formation and migration energies) to macroscopic quantities (conductivity). Calculating the conductivity of an amorphous phase is not a straightforward task because

different defect sites may have distinct formation energies and migration barriers.<sup>177,178</sup> We derive an estimate of the conductivity of our model of a-Li<sub>2</sub>O<sub>2</sub> based on the idea of percolation.<sup>177</sup> In general, the conductivity associated with defects is determined by the sum of the formation and migration energies,<sup>145</sup> which we will refer to as the transition state formation energy,  $E_t = E_f + E_a$ . The concentration of defects at the transition state is determined by  $E_t$ . Given that we have a distribution of transition state formation energies (because both  $E_f$  and  $E_a$  vary from site-to-site), what is a sensible way to compute the conductivity? Consistent with experimental observations of Arrhenius behavior for conductivity in amorphous materials,<sup>177</sup> we adopt an Arrhenius type expression for the conductivity, similar to that of Schirmacher,<sup>177</sup> with the activation energy given by the transition state formation energy at which a percolating network forms:

$$(4.2) \quad \sigma = \frac{\nu e^2}{ak_B T} \exp\left(-\frac{E_p}{k_B T}\right).$$

Here  $\nu$  is the migration attempt rate which we take to be  $10^{13}$  Hz,<sup>152,156</sup>  $e$  is the electron charge, and  $a$  is the characteristic distance between defects which we take to be  $3 \text{ \AA}$ . The energy scale  $E_p$  is set by the bond percolation threshold  $p$ ; that is,  $E_p$  is the smallest energy such that at least a fraction  $p$  of transition state formation energies are less than  $E_p$ ,

$$(4.3) \quad p = \int_0^{E_p} F(E) dE,$$

where  $F(E)$  is the probability distribution of transition state energies. Note that although the concentration and mobility do not appear explicitly in our expression for the conductivity, they are both accounted for via contributions from formation energies and migration barriers to the distribution of transition state energies. To estimate the integral in Eq. 7 from the transition state energies obtained from our DFT calculations, we employ linear interpolation<sup>179</sup> to calculate the percentile:

$$(4.4) \quad E_p = E_t^k + d(E_t^{k+1} - E_t^k).$$

Here  $E_t^i$  is the energy of the transition state that is the  $i^{\text{th}}$  lowest in energy. The variables  $k$  and  $d$  are defined by

$$(4.5) \quad p(N+1) = k + d,$$

where  $k$  is an integer,  $d$  is between zero and one, and  $N$  is the number of transition states sampled. We obtain  $E_t^i$  for  $V_{\text{Li}}^-$  migration by adding the calculated PBE GGA (forward) migration barriers to the HSE formation energies.

We adopt a percolation threshold of 0.2, which lies between the thresholds for fcc ( $p = 0.12$ ) and simple cubic lattices ( $p = 0.25$ ).<sup>180</sup> This is motivated by the fact that the Li-Li coordination number of 9.1 (based on the integrated pair distribution function up to the first minimum) lies between the coordination numbers of the fcc and simple cubic lattices, 12 and 6. The resulting percolation energy for  $V_{\text{Li}}^-$  migration,  $E_p = 0.55$  eV, is significantly lower than the  $V_{\text{Li}}^-$  transition state energy for crystalline  $\text{Li}_2\text{O}_2$  (1.32 eV),<sup>70</sup> suggesting that ionic conductivity should be greatly enhanced in the amorphous phase. Indeed, using this approach we find that the ionic conductivity for a- $\text{Li}_2\text{O}_2$ ,  $2 \times 10^{-7}$  S/cm, is 12 orders of magnitude larger than that predicted for c- $\text{Li}_2\text{O}_2$ ,  $4 \times 10^{-19}$  S/cm.<sup>70</sup> This increase arises from an increase to both the concentration and mobility of negative lithium vacancies. We note that the percolation energy is not greatly affected by the choice of percolation threshold: thresholds of 0.12 (fcc) and 0.25 (sc) yield  $V_{\text{Li}}^-$  percolation energies of 0.46 and 0.58 eV, respectively.

For polaron hopping, we calculated the HSE adiabatic hopping barrier using a chain of linearly interpolated geometries. Table 4.4 shows the barriers calculated for  $p^+$  hopping along a number of different paths, shown in Figure 4.6. Figure 4.6 also shows the energy profile for hopping along a contiguous pathway traversing all of 14 paths considered. The hopping barriers lie in the range 0.4-1.0 eV,

similar to the barriers of 0.4-0.7 found in c-Li<sub>2</sub>O<sub>2</sub>.<sup>70</sup> We observed that the barrier height was only weakly correlated with hopping distance and the relative orientation between dimers.

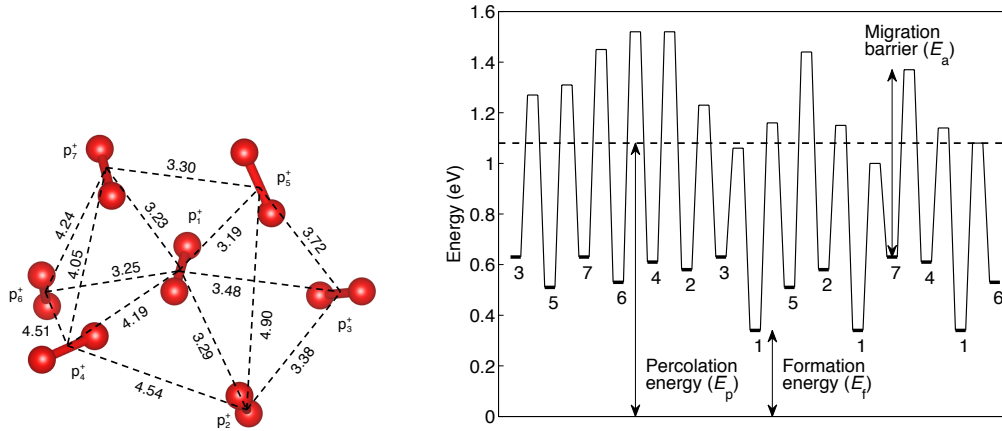


**Figure 4.6** Polaron hopping in amorphous Li<sub>2</sub>O<sub>2</sub>. Left: structural arrangement of polarons involved in the representative hopping paths considered. Distances between the centers of O<sub>2</sub> pairs are denoted in Å. Right: energy profile along a selected path for polaron hopping calculated with HSE ( $\alpha = 0.48$ ). Thick lines show the formation energies for polaron sites and thin lines show the hopping energies along a representative pathway. The horizontal dashed line shows the percolation energy. The polaron sites are numbered in the same order as in Table 4.2.

Applying the above procedure, we calculate a percolation energy of  $E_p = 1.08$  eV and conductivity of  $2 \times 10^{-16}$  S/cm for polaron hopping. (Percolation thresholds of 0.12 and 0.25 yield similar p<sup>+</sup> percolation energies of 1.05 and 1.13 eV.) The predicted electronic conductivity is four orders of magnitude higher than the predicted in-plane electronic conductivity of c-Li<sub>2</sub>O<sub>2</sub> ( $5 \times 10^{-20}$  S/cm), and significantly higher than the out-of-plane electronic conductivity of c-Li<sub>2</sub>O<sub>2</sub> ( $1 \times 10^{-24}$  S/cm).<sup>70</sup> Nevertheless, because the intrinsic conductivity of c-Li<sub>2</sub>O<sub>2</sub> is so low, the moderate increases exhibited by a-Li<sub>2</sub>O<sub>2</sub> relative to the crystalline phase do not result in a high electronic conductivity overall.

Taken together, our calculations suggest that transport within amorphous LiO<sub>2</sub> can differ significantly from that in crystalline Li<sub>2</sub>O<sub>2</sub>: ionic and electronic conductivities are predicted to be ~12 and ~4 orders of magnitude higher in a-Li<sub>2</sub>O<sub>2</sub>, respectively, than c-Li<sub>2</sub>O<sub>2</sub>. If the electron transfer occurs at the Li<sub>2</sub>O<sub>2</sub>/electrolyte interface (requiring potentially ‘long-range’ transport across the

Li<sub>2</sub>O<sub>2</sub> product phase), as has been suggested by some,<sup>73,80,89</sup> then an enhanced electronic conductivity would be expected to mitigate electrical passivation. On the other hand, ionic conductivity would not necessarily be expected to play an important role because the positive electrode material is typically ion-blocking.<sup>70,144</sup> However a high ionic conductivity could potentially enable other reaction pathways during recharge, such as the topotactic delithiation of Li<sub>2</sub>O<sub>2</sub> to form LiO<sub>2</sub>.<sup>75</sup> Li-ion transport would be important if the topotactic phase transformation initiates at the Li<sub>2</sub>O<sub>2</sub>/electrode interface. In this case Li-ion transport through the Li<sub>2</sub>O<sub>2</sub> could be rate limiting, and the enhanced ionic conductivity of the amorphous phase could improve performance. This scenario is discussed in more detail in Section 5.4.

**Table 4.4** Hole polaron hopping barriers in amorphous Li<sub>2</sub>O<sub>2</sub> (calculated by HSE) between O<sub>2</sub> dimer sites illustrated in Figure 4.6.  $E_a^+$  and  $E_a^-$  are respectively the barriers for the forward and backward directions of hopping. Hopping pairs are denoted by the polaron site numbers.

Path	$E_a^+ / E_a^-$ (eV)	Path	$E_a^+ / E_a^-$ (eV)
1-2	0.81/0.57	2-4	0.94/0.90
1-3	0.72/0.43	2-5	0.86/0.93
1-4	0.80/0.53	3-5	0.64/0.77
1-5	0.82/0.65	4-6	0.91/1.00
1-6	0.74/0.56	4-7	0.76/0.75
1-7	0.66/0.37	5-7	0.80/0.68
2-3	0.65/0.59	6-7	0.92/0.81

#### 4.4 Discussion

Using first-principles molecular dynamics, we have developed an atomic-scale model for amorphous  $\text{Li}_2\text{O}_2$ . We find that the formation energy of this phase is only slightly smaller (less negative) than crystalline  $\text{Li}_2\text{O}_2$ , confirming that a- $\text{Li}_2\text{O}_2$  can be formed electrochemically at potentials not much lower than for c- $\text{Li}_2\text{O}_2$ . The fact that energy difference between amorphous and crystalline  $\text{Li}_2\text{O}_2$  is relatively small can be attributed to the fact that the bonding between Li and O is primarily ionic and therefore isotropic. The small decrease in equilibrium potential and density of the amorphous phase relative to the crystalline phase indicates that a Li- $\text{O}_2$  battery which produces the amorphous phase will have a slightly lower gravimetric and volumetric energy density. However, such a sacrifice may be worthwhile given the differences in transport properties.

Our calculations suggest a moderately high ionic conductivity of  $2 \times 10^{-7}$  S/cm arising from the high mobility and concentration of lithium vacancies. In comparison, the electronic conductivity ( $2 \times 10^{-16}$  S/cm) is significantly lower than the ionic conductivity, but remains slightly higher than the electronic conductivity of crystalline  $\text{Li}_2\text{O}_2$ . We speculate that these enhanced transport properties could explain the lowered charging overpotentials observed in Li- $\text{O}_2$  cells containing amorphous discharge products. These results support the notion that the performance of Li- $\text{O}_2$  cells will depend upon the properties (degree of crystallinity, microstructure, particle morphology, etc.) of the primary discharge phase,  $\text{Li}_2\text{O}_2$ . We speculate that the round-trip efficiency of Li- $\text{O}_2$  batteries may be improved by biasing the discharge mechanism to produce a predominantly amorphous discharge phase.

## Chapter 5: Doped Li<sub>2</sub>O<sub>2</sub>

### 5.1 Introduction

As discussed in Chapter 1, one of the most significant of these challenges for Li-O<sub>2</sub> batteries is to minimize the high overpotential required to drive the recharging process, which is an oxygen evolution reaction (OER) associated with decomposition of the solid lithium peroxide (Li<sub>2</sub>O<sub>2</sub>) discharge product. Many studies have employed materials intended to reduce OER overpotentials, but the specific role these materials play is unclear.<sup>17,109,110,169,181–184</sup> Although these additives are often referred to as ‘catalysts’, it appears unlikely that they function as true electrocatalysts for the OER, given that: (i.) conventional catalysts would presumably become buried by Li<sub>2</sub>O<sub>2</sub> during discharge and rendered inactive;<sup>109</sup> and (ii.) prior studies have found kinetics of the OER to be facile on typical substrates without additives present.<sup>80</sup>

A recent study by Black et al. demonstrated the ability of Co<sub>3</sub>O<sub>4</sub>-containing electrodes to promote the oxidation of Li<sub>2</sub>O<sub>2</sub> in an Li-O<sub>2</sub> cell.<sup>183</sup> The charge plateau for these electrodes was approximately 400 mV lower than in carbon electrodes, despite the fact that the presence of Co<sub>3</sub>O<sub>4</sub> did not appear to influence the Li<sub>2</sub>O<sub>2</sub> morphology (which is known to affect charging potentials<sup>42,47,48,185–187</sup>) or contribute significantly to electrolyte oxidation. Since the effect could not be attributed to catalysis, the term ‘promoter’ was suggested.<sup>183</sup> Henceforth we adopt the same nomenclature to refer to a compound that reduces the overpotentials of a Li-O<sub>2</sub> cell by a mechanism besides catalysis. It was speculated that the promotion of the OER arose from an enhancement in surface transport of Li<sub>x</sub>O<sub>2</sub> species, or possibly the scavenging of nascent oxygen. Additional studies have found Li-O<sub>2</sub> electrodes containing Co<sub>3</sub>O<sub>4</sub><sup>188–192</sup> and Co-containing compounds<sup>193,194</sup> to exhibit improved performance.

Several mechanisms have been hypothesized to justify observations that positive-electrode additives reduce cell potentials during charging.<sup>17,42,47,48,109,157,169,183,185–187,195,196</sup> Despite the abundance of proposed explanations, the mechanism by which a given promoter functions remains an open question. Motivated by the experiments of Black et al.,<sup>183</sup> this paper explores the possibility and consequences of Co incorporation as a substitutional dopant within the  $\text{Li}_2\text{O}_2$  discharge product. More specifically, a detailed model is developed to evaluate the effects of Co doping on the transport properties of  $\text{Li}_2\text{O}_2$ , by combining first-principles calculations with a continuum transport model.

Charge-transport limitations through  $\text{Li}_2\text{O}_2$  are thought to contribute significantly to charging overpotentials.<sup>11,17,70,73,81</sup> Consequently, it is hypothesized here that the incorporation of impurities may enhance  $\text{Li}_2\text{O}_2$  oxidation, by improving the conductivity associated with hole polarons and/or Li-ion vacancies. This *in situ* doping could occur via diffusion of Co ions into the discharge product during its growth, or through the incorporation of Co ions that are dissolved in the electrolyte. The electrochemical incorporation of additives has been exploited in other contexts, such as the electrodeposition of metals<sup>197</sup> and the formation of tailored solid-electrolyte interphases in Li-ion batteries,<sup>198</sup> motivating the concept of doping  $\text{Li}_2\text{O}_2$  *in situ*. Indeed, experiments on Li-O<sub>2</sub> cells have shown that halide species from the electrolyte are incorporated into the discharge product.<sup>96</sup>

To investigate the feasibility and consequences of *in situ* doping of Li-O<sub>2</sub>-battery discharge products, here we calculate the thermodynamics of Co substitutions in  $\text{Li}_2\text{O}_2$ ; this data is subsequently used to parameterize a continuum model that demonstrates the impact of doping on transport within a  $\text{Li}_2\text{O}_2$  film. When incorporated into the transport model, the observed low formation energies for Co substitutions support the notion that doping could significantly enhance charge transport in  $\text{Li}_2\text{O}_2$ . For example, if Co is incorporated at equilibrium levels (13 ppm), the transport model predicts that only ~10 mV of potential is needed to drive a  $1 \mu\text{A}/\text{cm}^2$  current density through a 100 nm film. This contrasts strongly with undoped  $\text{Li}_2\text{O}_2$ , which some of the authors previously predicted to be highly

resistive, requiring overpotentials of  $\sim 1$  V to drive appreciable currents.<sup>70</sup> Such an enhancement of transport properties by doping is consistent with the well-known impact of point defects on solid-state charge and mass transport processes.<sup>145,146</sup> Although the present analysis focuses on rationalizing recent experiments involving Co-containing Li-O<sub>2</sub> electrodes,<sup>183</sup> it is reasonable to hypothesize that the mechanism proposed here could also explain the beneficial impact of other promoters on the OER from Li<sub>2</sub>O<sub>2</sub>.<sup>110,182,190,199</sup>

## 5.2 Methods

It is first necessary to determine the expected equilibrium concentration of Co dopants within the  $\text{Li}_2\text{O}_2$  discharge phase. As discussed in Chapter 3, it was determined that the dominant intrinsic charge carriers are hole polarons and negative lithium vacancies;<sup>70</sup> a recent experimental study also independently arrived at the same conclusion.<sup>81</sup>

The introduction of Co dopants within the  $\text{Li}_2\text{O}_2$  discharge phase can shift the equilibrium concentrations of intrinsic defects as follows. The equilibrium concentrations of defects were calculating following the method described in Section 2.3.1. The (HSE) functional<sup>119,120</sup> was used, with 144 atom supercells and  $\Gamma$ -point only  $k$ -space integration. An HSE mixing parameter of  $\alpha = 0.48$  was used, as discussed in Section 2.2.2.

The formation energies and equilibrium concentrations of defects depend on the chemical potentials of Li, O, and Co. To determine which phases will be present when the Li-O<sub>2</sub> electrode is at equilibrium, we have constructed the Li-Co-O phase diagram (Figure 5.1) using values for the Gibbs free energies of formation at standard temperature and pressure taken from experimental data (Table 5.1). In the case of  $\text{LiCoO}_2$ , we were unable to find an experimental value for the Gibbs free energy of formation. We instead combined the formation enthalpy of  $\text{LiCoO}_2$ <sup>200</sup> with the entropy of  $\text{O}_2$ ,<sup>12</sup> and neglected any contributions to entropy from the solid phases:

$$(5.1) \quad \Delta G_f(\text{LiCoO}_2) \approx \Delta H_f(\text{LiCoO}_2) + TS(\text{O}_2).$$

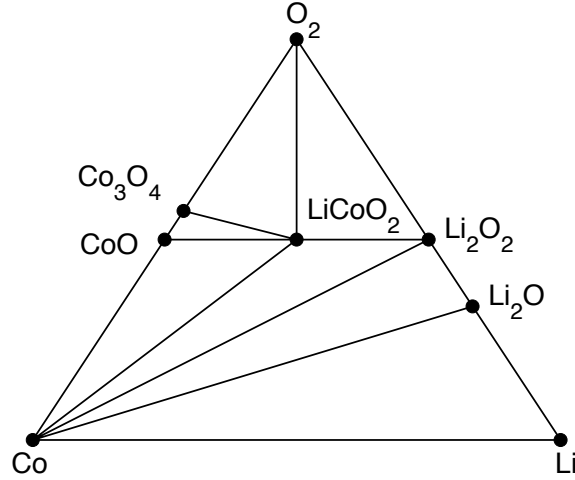


**Figure 5.1** Ternary Li-Co-O phase diagram constructed from experimental Gibb's free energies of formation.

**Table 5.1** Gibb's free energies of formation for Li-Co-O compounds.

Compound	$\Delta G_f$ (eV)
$\text{Li}_2\text{O}_2$	$-5.93^{12}$
$\text{Li}_2\text{O}$	$-5.84^{12}$
$\text{CoO}$	$-2.22^{12}$
$\text{Co}_3\text{O}_4$	$-8.25^{12}$
$\text{LiCoO}_2$	$-6.39^{12,200}$

As discussed in the main text, the chemical potential of Co in the electrode will be determined by which Co compounds can coexist with  $\text{Li}_2\text{O}_2$  and  $\text{O}_2$ . The Li-Co-O phase diagram shows that  $\text{LiCoO}_2$  is the only Co compound that can coexist with  $\text{Li}_2\text{O}_2$  and  $\text{O}_2$ . Therefore we have used equilibrium with  $\text{LiCoO}_2$ ,  $\text{Li}_2\text{O}_2$ , and  $\text{O}_2$  as the thermodynamic boundary condition for determining the chemical potential of Co:

$$(5.2) \quad \mu_{\text{Co}} = G(\text{LiCoO}_2) - \frac{1}{2}G(\text{Li}_2\text{O}_2) - \frac{1}{2}G(\text{O}_2).$$

However, accurately calculating the ground state energies of oxides (and particularly transition metal oxides) remains a challenge for density functional theory.<sup>75,89,201</sup> To mitigate these errors, we have adopted the strategy of obtaining the Co chemical potential by combining the ground state energy of a reference

phase, solid Co metal, with the experimental formation free energies<sup>12,200</sup> of  $\text{LiCoO}_2$  and  $\text{Li}_2\text{O}_2$ , similar to the procedure used in prior computational studies:<sup>70,158</sup>

$$(5.3) \quad \mu_{\text{Co}} = \Delta G_f(\text{LiCoO}_2) + E_0(\text{hcp Co}) - \frac{1}{2} \Delta G_f(\text{Li}_2\text{O}_2).$$

In principle, if our calculations yielded the true ground state energy (and the experimental data were exact), defect formation energies would be the same regardless of what reference state we use for Co. However, in practice different choices for the reference phase will yield different results. For example, one might use atomic Co, rather than solid Co, as the reference phase. Indeed we find that the magnitude of the atomization energy of hcp Co is underestimated by 1.06 and 1.83 eV/atom when using  $\alpha = 0.25$  and 0.48; thus the chemical potential of Co would be lower (and formation energies of substitutions higher) had we chosen atomic Co, rather than solid Co, as the reference state. This result is perhaps not surprising, as it has been previously observed that hybrid functionals tend to overbind transition metal atoms relative to the solid metal.<sup>128</sup> The decision to use solid Co as the reference state is motivated by the fact that the HSE functional generally gives a good description of solid metals because HSE, like LDAs and GGAs, is exact in the limit of a uniform electron gas.<sup>128</sup>

### 5.3 Defect chemistry

Substitution of Co on Li sites was considered for the two common charge states of  $\text{Co}^{2+}$  –  $\text{Co}^{2+}$  and  $\text{Co}^{3+}$ . These substitutions are notated here as  $\text{Co}_{\text{Li}}^+$  and  $\text{Co}_{\text{Li}}^{2+}$ , respectively, where the superscript refers to the net charge of the defect, not the charge state of the Co ion. We also considered substitution-vacancy complexes,  $\text{Co}_{\text{Li}}^{2+}\text{-V}_{\text{Li}}^-$  and  $\text{Co}_{\text{Li}}^+\text{-V}_{\text{Li}}^-$ . Since there are two symmetry inequivalent Li sites (trigonal prismatic (TP) and octahedral (Oct)), the total number of defects considered is twelve: two  $\text{Co}_{\text{Li}}^+$ , two  $\text{Co}_{\text{Li}}^{2+}$ , four  $\text{Co}_{\text{Li}}^+\text{-V}_{\text{Li}}^-$ , and four  $\text{Co}_{\text{Li}}^{2+}\text{-V}_{\text{Li}}^-$  sites.

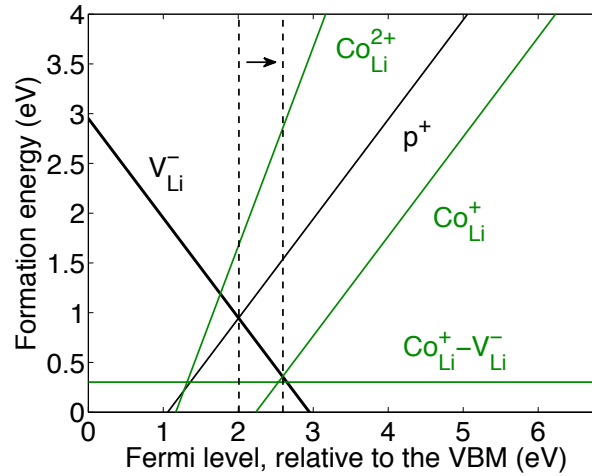


**Figure 5.2** Calculated formation energies of Co impurities, negative Li vacancies, and hole polarons in  $\text{Li}_2\text{O}_2$ . The zero of the Fermi level is to the valence band maximum (VBM); vertical dotted lines show the shift in equilibrium Fermi level induced by incorporating Co impurities. Only the lowest-energy extrinsic defect for each charge state is shown.

**Table 5.2** Equilibrium formation energies and concentrations of Co substitutions and intrinsic defects.

Defect	$E_k^0$ (eV)	$c_k^0$ (cm <sup>-3</sup> )	Defect	$E_k^0$ (eV)	$c_k^0$ (cm <sup>-3</sup> )
p <sup>+</sup>	1.54	1 × 10 <sup>-3</sup>	Co <sub>Li</sub> <sup>+</sup> (Oct)- V <sub>Li</sub> <sup>-</sup> (Oct)	0.42	1 × 10 <sup>16</sup>
V <sub>Li</sub> <sup>-</sup> (Oct)	0.36	2 × 10 <sup>16</sup>	Co <sub>Li</sub> <sup>+</sup> (Oct)- V <sub>Li</sub> <sup>-</sup> (TP)	0.30	2 × 10 <sup>18</sup>
V <sub>Li</sub> <sup>-</sup> (TP)	0.34	5 × 10 <sup>16</sup>	Co <sub>Li</sub> <sup>+</sup> (TP)- V <sub>Li</sub> <sup>-</sup> (Oct)	1.22	6 × 10 <sup>2</sup>
Co <sub>Li</sub> <sup>+</sup> (Oct)	0.36	7 × 10 <sup>16</sup>	Co <sub>Li</sub> <sup>+</sup> (TP)- V <sub>Li</sub> <sup>-</sup> (TP)	1.45	9 × 10 <sup>-2</sup>
Co <sub>Li</sub> <sup>+</sup> (TP)	1.38	7 × 10 <sup>-1</sup>	Co <sub>Li</sub> <sup>2+</sup> (Oct)- V <sub>Li</sub> <sup>-</sup> (Oct)	2.57	2 × 10 <sup>-20</sup>
Co <sub>Li</sub> <sup>2+</sup> (Oct)	2.86	3 × 10 <sup>-26</sup>	Co <sub>Li</sub> <sup>2+</sup> (Oct)- V <sub>Li</sub> <sup>-</sup> (TP)	2.45	1 × 10 <sup>-18</sup>
Co <sub>Li</sub> <sup>2+</sup> (TP)	3.16	3 × 10 <sup>-31</sup>	Co <sub>Li</sub> <sup>2+</sup> (TP)- V <sub>Li</sub> <sup>-</sup> (Oct)	2.65	7 × 10 <sup>-22</sup>
			Co <sub>Li</sub> <sup>2+</sup> (TP)- V <sub>Li</sub> <sup>-</sup> (TP)	4.02	7 × 10 <sup>-45</sup>

Figure 5.2 shows the calculated formation energies of the most stable of these 12 substitutional defects, as well as the formation energies of the dominant charged intrinsic defects,<sup>70</sup> Li-ion vacancies (V<sub>Li</sub><sup>-</sup>) and hole polarons (p<sup>+</sup>). Equilibrium formation energies and concentrations (with the Fermi level set by electroneutrality in the presence of Co) are listed in Table 5.2. The computations indicate that Co ions in Li<sub>2</sub>O<sub>2</sub> favor the +2 charge state over the +3 charge state, and prefer the Oct Li site over the TP site. The lowest energy configuration under equilibrium conditions is the Co<sub>Li</sub><sup>+</sup> (Oct)- V<sub>Li</sub><sup>-</sup> (TP) complex, with a formation energy of 0.30 eV, representing a 13 ppm doping level (2 × 10<sup>18</sup> cm<sup>-3</sup>). Since this complex is electrically neutral, it will not affect the Fermi level. The lowest-energy charged substitution is Co<sub>Li</sub><sup>+</sup> (Oct), which corresponds to the substitution of a Li<sup>+</sup> ion with a Co<sup>2+</sup> ion. The calculated equilibrium formation energy of Co<sub>Li</sub><sup>+</sup> (Oct) is 0.36 eV, which corresponds to a 1 ppm doping level (7 × 10<sup>16</sup> cm<sup>-3</sup>). To put this in context, note that the calculated Co concentration is comparable to the level of inorganic ionic impurities typically incorporated during electrodeposition of metals (10<sup>-5</sup>-10<sup>-4</sup> atomic fraction<sup>197</sup>) and is also within the typical range of dopant concentrations in semiconductor devices (10<sup>-8</sup>-10<sup>-5</sup> atomic fraction<sup>203</sup>). Notably, the Co<sub>Li</sub><sup>+</sup> (Oct) defect has significantly lower energy than the hole polaron (the dominant positive intrinsic defect). Thus the introduction of Co could

cause a substantial change in the defect chemistry, since the Fermi level relative to the local electrostatic potential is shifted to higher energies. Consequently, in the presence of Co dopants the concentration of  $V_{Li}^-$  increases 9 orders of magnitude to  $7 \times 10^{16} \text{ cm}^{-3}$  (i.e.,  $Li^+$  ions are removed to compensate the charge of the  $Co_{Li}^+$ ), and the concentration of  $p^+$  decreases to  $1 \times 10^{-3} \text{ cm}^{-3}$ . For comparison, the equilibrium concentration of  $p^+$  and  $V_{Li}^-$  in the absence of dopants is  $\sim 10^7 \text{ cm}^{-3}$ .<sup>70</sup>

One factor contributing to the stability of the Co substitutions may be the minimal strain they exert on the  $Li_2O_2$  lattice: the relaxation of the  $Co_{Li}^+$  (Oct) geometry results in only a 2% change in the cation-anion nearest neighbor distance. Table 5.3 shows how the substitution of Co on Li sites alters the cation-anion distances in  $Li_2O_2$ , as well as the lattice strain energies. The lattice strain energy is calculated as the energy it takes to distort a pristine lattice to the relaxed defect geometry, but without replacing a  $Li^+$  ion with a  $Co^{2+}/Co^{3+}$  ion. The  $Co_{Li}^+$  defect shows a similar change in the cation-anion distance and a similar lattice strain energy at the Oct and TP sites. This suggests that some other effect is responsible for the  $\sim 1 \text{ eV}$  energy difference between these two sites. As discussed below, we speculate that the crystal field stabilization energy could be make up a significant portion of this energy difference.

**Table 5.3** Cation-anion distances and lattice strain energies for Co substitutions in  $Li_2O_2$ . Slashes separate values where a Jahn-Teller distortion breaks the symmetry between the nearest oxygen sites.

Site	Configuration	Cation-anion distance (Å)	Percent change	Strain energy (eV)
	Pristine	2.146	0.0	0.00
Octahedral	$Co_{Li}^+$	2.098/2.108	-2.3/-1.8	0.53
	$Co_{Li}^{2+}$	1.930	-10.1	3.10
	Pristine	1.947	0.0	0.00
Trigonal prismatic	$Co_{Li}^+$	2.003/2.015	2.9/3.5	0.74
	$Co_{Li}^{2+}$	1.909	-2.0	2.42

To further elucidate the thermodynamic and magnetic properties of Co substitutions, we have used crystal field theory<sup>204</sup> to analyze the electronic structure of these defects. Figure 5.3 shows qualitative energy level diagrams for the Co d states for the four different substitutions. In a site with perfect octahedral symmetry, the d states will be split into a high energy two-fold degenerate  $e_g$  level and a low energy three-fold degenerate  $t_{2g}$  level. The ‘octahedral’ site in  $\text{Li}_2\text{O}_2$  is in fact slightly distorted, lowering the symmetry of the cation site from  $O_h$  to  $D_{3d}$ . Consequently, the  $t_{2g}$  level splits into a two-fold degenerate  $e_g$  level and a non-degenerate  $a_{1g}$  level. The fact that the aspect ratio of the distorted octahedron is larger than that of a perfect octahedron suggests that the  $a_{1g}$  level will be the lower of these two. This reasoning is confirmed by the presence of a Jahn-Teller distortion in the high-spin ( $\mu = 3\mu_B$ )  $\text{Co}_{\text{Li}}^+(\text{Oct})$  defect. This distortion lowers the symmetry from  $D_{3d}$  to  $C_{2h}$  via the slight contraction of one of the three nearest neighbor distances. Figure 5.3a summarizes the energy levels for this defect. The  $\text{Co}_{\text{Li}}^{2+}(\text{Oct})$  defect (Figure 5.3b) was found to be in a low-spin state ( $\mu = 0$ ) and did not exhibit any Jahn-Teller distortion.

The TP site, having  $D_{3h}$  symmetry, behaves similarly to the Oct site. We assign the lowest energy state to be the non-degenerate  $a_1'$  state, while the remaining states form a two-fold degenerate  $e'$  level and two-fold degenerate  $e''$  level. A visual inspection of the  $lm$ -decomposed density of states (not shown) indicates that the  $e''$  level ( $xz, yz$ ) is above the  $e'$  level ( $xy, x^2-y^2$ ). The  $\text{Co}_{\text{Li}}^+(\text{TP})$  defect (Figure 5.3c) exhibits a high-spin state ( $\mu = 3\mu_B$ ) with a Jahn-Teller distortion due to the degeneracy of the  $e'$  levels, lowering the symmetry to  $C_{2v}$ . However, unlike the  $\text{Co}_{\text{Li}}^{2+}(\text{Oct})$  defect, the  $\text{Co}_{\text{Li}}^{2+}(\text{TP})$  defect favors a high-spin state ( $\mu = 4\mu_B$ ), as shown in Figure 5.3d. The absence of any Jahn-Teller distortion for the  $\text{Co}_{\text{Li}}^{2+}(\text{TP})$  supports our assigned ordering of the energy levels.

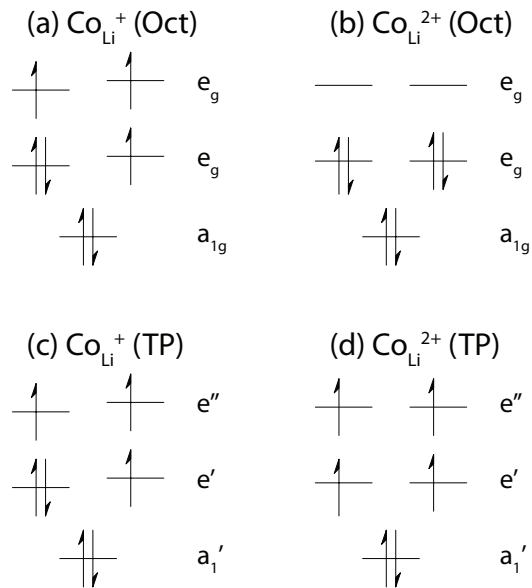


**Figure 5.3** Crystal field splittings for Co substitutions at the octahedral (Oct) and trigonal prismatic (TP) Li sites in  $\text{Li}_2\text{O}_2$ .

The  $\text{Co}_{\text{Li}}^+$  is 1.01 eV more stable at the octahedral site than the trigonal prismatic site. We speculate that the stabilization energy associated with the crystal field splitting may contribute to the preference for the octahedral site: the lobes of the lower  $e_g$  orbitals in the octahedral site are oriented along the gaps between the neighboring oxygen sites, thus minimizing electron-electron repulsion. The  $\text{Co}_{\text{Li}}^{2+}$  is also more stable at the octahedral site than the trigonal prismatic site, but only by 0.30 eV. Again, the crystal field stabilization energy could contribute to this preference, and the decreased occupancy of this  $e_g$  level could explain why the Oct site and TP sites are closer in energy in this charge state. Furthermore, the large crystal field splitting associated with the stabilization of the lower  $e_g$  level would explain why the  $\text{Co}_{\text{Li}}^{2+}$  defect prefers a low-spin state in the Oct site but a high-spin state in the TP site.

## 5.4 Transport model

Having established the concentration of Co dopants in  $\text{Li}_2\text{O}_2$  at equilibrium, we next examine the effect that this doping exerts on transport properties. To this end, a one-dimensional transport model based on Nernst-Planck theory was developed to calculate the quasi-steady-state voltage drop associated with charge transport through doped  $\text{Li}_2\text{O}_2$ . This voltage drop represents the contribution of charge-transport limitations to the cell's overpotential. In the present context, 'quasi-steady-state' is intended to mean that diffusional relaxations associated with local accumulation of material occur very rapidly in comparison to the timescale of interest, and also that the film thickness changes sufficiently slowly on this timescale that the velocity of the peroxide-film/electrolyte boundary can be neglected. The former is valid when the characteristic diffusion time for the slowest-diffusing species is much shorter than the period of discharge or charge; indeed this is the case for hole polarons and Li-ion vacancies under realistic operating conditions.<sup>70</sup>

Figure 5.4 illustrates two scenarios, motivated by previous experimental and theoretical studies, to which the transport model is applied: (a) the layer-by-layer electrochemical deposition/stripping of the  $\text{Li}_2\text{O}_2$  deposit, occurring at the  $\text{Li}_2\text{O}_2$ /electrolyte interface;<sup>73</sup> and (b) a two-phase delithiation mechanism, in which delithiation of  $\text{Li}_2\text{O}_2$ , starts at the buried  $\text{Li}_2\text{O}_2$ /electrode interface, and  $\text{Li}^+$  diffuses through the film to reach the electrolyte.<sup>64,70,75</sup> Key differences between the scenarios are summarized below:

1. While Scenario I (layer-by-layer stripping/deposition) can represent mechanisms for both discharge and charge, Scenario II (two-phase delithiation) applies only to charging.

2. As is shown below, steady-state charge transport through  $\text{Li}_2\text{O}_2$  in Scenario I is mediated by hole polarons; in Scenario II, Li-ion vacancies mediate charge transport. Both mechanisms are illustrated qualitatively in Figure 5.4.

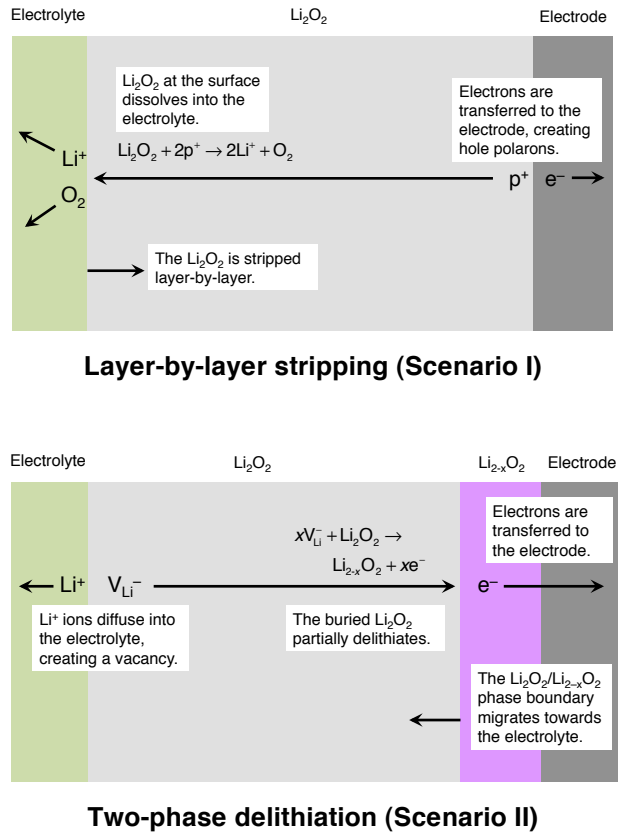


**Figure 5.4** Model for transport through a doped  $\text{Li}_2\text{O}_2$  film during recharge in the case of (top) Scenario I: layer-by-layer stripping and (bottom) Scenario II: two-phase delithiation. Here  $\text{p}^+$  refers to a hole polaron in  $\text{Li}_2\text{O}_2$ , which moves in the opposite direction as an electron,  $\text{e}^-$ . Similarly,  $\text{V}_{\text{Li}}^-$  refers to a negatively charged Li vacancy, which moves in the opposite direction as  $\text{Li}^+$ .

The overall half-reaction for oxidation in Scenario I is  $\frac{1}{2}\text{Li}_2\text{O}_2(\text{p}) \rightarrow \text{Li}^+(\text{l}) + \frac{1}{2}\text{O}_2(\text{l}) + \text{e}^-(\text{s})$  [where (p) indicates a species in the discharge product, (l) a species in the liquid-electrolyte phase, and (s) a species in the electrode's support material], but in Scenario II it is  $\text{Li}_2\text{O}_2(\text{p}) \rightarrow x\text{Li}^+(\text{l}) + \text{Li}_{2-x}\text{O}_2(\text{p}) + x\text{e}^-(\text{s})$ . Presumably, the oxidation of  $\text{Li}_2\text{O}_2$  to  $\text{Li}_{2-x}\text{O}_2$  in Scenario II would be followed by a subsequent oxidation of  $\text{Li}_{2-x}\text{O}_2$  to form molecular  $\text{O}_2$ ; the implications of this are addressed in Section 5.5.

Scenario I assumes that the accumulation of defects does not produce a distinct solid phase. (In principle, the accumulation of  $V_{\text{Li}}^-$  and  $p^+$  could lead to the nucleation of a lithium-deficient  $\text{Li}_{2-x}\text{O}_2$  phase; Scenario II describes one such situation.) The defect concentration in Scenario I is small enough ( $\sim 1$  ppm, as shown below) that the nucleation of a Li-deficient phase may not occur. Also, observe that an accumulation of both lithium and oxygen vacancies could lead to void formation, but the high barrier for oxygen-vacancy diffusion in  $\text{Li}_2\text{O}_2$  ( $1.5 \text{ eV}$ )<sup>205</sup> suggests that voids are unlikely.

Scenario II is motivated by a recent study which predicted that  $\text{Li}_2\text{O}_2$  could be topotactically delithiated to lithium superoxide ( $\text{LiO}_2$ ) at moderate charge potentials ( $3.34 \text{ V vs. Li/Li}^+$ ).<sup>75</sup> The presence of a plateau at  $3.4\text{-}3.5 \text{ V vs. Li/Li}^+$  during potentiostatic intermittent titration technique (PITT) experiments on  $\text{Li}/\text{O}_2$  cells also supports a two-phase delithiation hypothesis.<sup>79,206</sup> The formation of  $\text{LiO}_2$  corresponds to  $x = 1$ , although other Li-deficient stoichiometries may be possible. Electron-transport limitations through a Li-deficient phase could also contribute to charging overpotentials, but any such limitations are neglected here because: (i) the high electronic conductivity reported for crystalline  $\text{KO}_2$  suggests that  $\text{LiO}_2$  may also have a high electronic conductivity;<sup>207</sup> and (ii) a  $\text{Li}_{2-x}\text{O}_2$  ( $0 < x < 1$ ) solid-solution phase is expected to have a high electronic conductivity associated with electron hopping.<sup>70</sup>

Prior studies have treated transport in  $\text{Li}_2\text{O}_2$  through simplified models wherein the carrier concentrations are taken to be spatially and temporally uniform.<sup>64,70,73</sup> Although these studies provide important baselines, the incorporation of concentration gradients within the present model leads to qualitatively different – and presumably more accurate – current-voltage relationships for transport through doped  $\text{Li}_2\text{O}_2$ . The model described below indicates that charge transport through doped  $\text{Li}_2\text{O}_2$  is facile in both scenarios during recharge.

### 5.4.1 Governing equations

The model accounts for four mobile species in the  $\text{Li}_2\text{O}_2$  film:  $\text{V}_{\text{Li}}^-$ ,  $\text{p}^+$ , and  $\text{Co}_{\text{Li}}^+$ , and  $\text{Co}_{\text{Li}}^+ - \text{V}_{\text{Li}}^-$  bound pairs. The most fundamental model equations describe the continuity of material, which requires that (i.) the fluxes Li and Co atoms are divergence free,

$$(5.5) \quad \frac{d}{dy} \left( N_{\text{V}_{\text{Li}}^-} + N_{\text{Co}_{\text{Li}}^+ - \text{V}_{\text{Li}}^-} \right) = 0 \quad \text{and} \quad \frac{d}{dy} \left( N_{\text{Co}_{\text{Li}}^+} + N_{\text{Co}_{\text{Li}}^+ - \text{V}_{\text{Li}}^-} \right) = 0,$$

where  $N_k$  is the flux of species  $k$ ; and (ii.) the continuity of charge, which requires that the current density  $i$  also be divergenceless,

$$(5.6) \quad \frac{di}{dy} = 0.$$

Here  $i$  is intended to be a cathodic current, meaning that  $i > 0$  for discharge and  $i < 0$  for recharge. In addition to obeying a continuity equation, charge is taken to balance locally through the electroneutrality constraint

$$(5.7) \quad c_{\text{p}^+} - c_{\text{V}_{\text{Li}}^-} + c_{\text{Co}_{\text{Li}}^+} = 0,$$

where  $c_k$  represents the number density of species  $k$ . This approximation is suitable for a doped film under typical operating conditions for a Li-O<sub>2</sub> cell, except in certain regimes where double-layer charging becomes important, as discussed below and in the Supporting Information.

### 5.4.2 Constitutive laws

Inside the  $\text{Li}_2\text{O}_2$  film Nernst-Planck flux laws describe the diffusion and migration of each species  $k$ ,

$$(5.8) \quad N_k = -D_k \frac{dc_k}{dy} - \frac{D_k z_k e}{k_B T} c_k \frac{d\Phi}{dy}$$

where  $\Phi$  is the electrostatic potential,  $k_B$  is the Boltzmann constant,  $e$  is the elementary charge, and  $T$  is the absolute temperature;  $D_k$  represents the diffusivity of species  $k$ , and  $z_k$  its equivalent charge ( $z_{V_{Li}^-} = -1$ ,  $z_{p^+} = +1$ ,  $z_{Co_{Li}^+} = +1$ , and  $z_{Co_{Li}^+ - V_{Li}^-} = 0$ ). Note that Nernst-Planck theory only applies to point defects if their concentrations are relatively low,<sup>208</sup> as discussed in the Supporting Information, this approximation is fair under operating regimes relevant for Li-O<sub>2</sub> batteries. Charge flux follows from the material fluxes through Faraday's law,

$$(5.9) \quad i = e \sum_k z_k N_k$$

The diffusion coefficients of hole polarons and Li-ion vacancies were taken from our prior DFT calculations ( $D_{p^+} = 9 \times 10^{-10} \text{ cm}^2\text{s}^{-1}$  and  $D_{V_{Li}^-} = 6 \times 10^{-9} \text{ cm}^2\text{s}^{-1}$ ).<sup>70</sup> Co is assumed to diffuse via a vacancy-mediated mechanism as a  $Co_{Li}^+ - V_{Li}^-$  bound pair, and the contributions of other diffusion mechanisms are neglected. Consequently the mobility of unbound Co is negligible ( $D_{Co_{Li}^+} = 0$ ), causing the unbound Co flux to vanish everywhere. As shown below, no assumptions about the value of the bound-pair diffusivity need be made, since the net flux of bound pairs vanishes uniformly; this also implies that bound-pair diffusion does not affect the potential drop.

Vacancy-substitution association/dissociation ( $Co_{Li}^+ + V_{Li}^- \leftrightarrow Co_{Li}^+ - V_{Li}^-$ ) is taken to be locally equilibrated,

$$(5.10) \quad \frac{c_{V_{Li}^-} c_{Co_{Li}^+}}{c_{Co_{Li}^+ - V_{Li}^-}} = \frac{c_{V_{Li}^-}^0 c_{Co_{Li}^+}^0}{c_{Co_{Li}^+ - V_{Li}^-}^0}$$

### 5.4.3 Boundary conditions

The film is taken to be planar and one-dimensional, with  $y$  representing the direction normal to the interfaces with the electrode and electrolyte. Boundary conditions differ for Scenario I (layer-by-layer deposition/stripping) and Scenario II (two-phase delithiation). In both scenarios we require defect formation to be in equilibrium with  $O_2$ ,  $Li_2O_2$ , and  $LiCoO_2$  at the  $Li_2O_2$ /electrolyte interface, corresponding to position  $y = 0$ . This constrains the concentrations of defects to those shown in Table 1:

$$(5.11) \quad c_k(0) = c_k^0.$$

By combining these constraints with the defect association/dissociation equilibrium (Eq. 6), the concentration of the  $Co_{Li}^+ - V_{Li}^-$  bound pairs at the  $Li_2O_2$ /electrolyte interface is also constrained.

The boundary at  $y = L$  represents the  $Li_2O_2$ /electrode interface in Scenario I and the  $Li_2O_2/Li_{2-x}O_2$  interface in Scenario II. Both scenarios require that the flux of Co through the  $y = L$  boundary be zero because the electrode is assumed to block flux of ionic Co:

$$(5.12) \quad N_{Co_{Li}^+}(L) + N_{Co_{Li}^+ - V_{Li}^-}(L) = 0.$$

In Scenario I, one additionally stipulates that the flux of Li vacancies across the  $Li_2O_2$ /electrode interface should vanish, as the electrode blocks Li-ion transport:

$$(5.13) \quad N_{V_{Li}^-}(L) + N_{Co_{Li}^+ - V_{Li}^-}(L) = 0.$$

In Scenario II, polarons are not consumed or produced at the  $Li_2O_2$ /electrolyte interface (or at least the rate of polaron consumption/production is assumed to be

negligible compared to the rate of delithiation). Thus the flux of hole polarons across the  $\text{Li}_2\text{O}_2/\text{electrolyte}$  interface is zero in Scenario II:

$$(5.14) \quad N_{p^+}(0) = 0.$$

#### 5.4.4 General remarks

Important consequences of this model include:

1. By combining the material balances from Eq. (5.5), the ion-blocking condition on Co from (5.5), and the fact that the flux of  $\text{Co}_{\text{Li}}^+$  vanishes, the steady-state flux of  $\text{Co}_{\text{Li}}^+ \text{-V}_{\text{Li}}^-$  bound pairs proves to vanish everywhere:
$$N_{\text{Co}_{\text{Li}}^+ \text{-V}_{\text{Li}}^-}(y) = 0.$$
2. Since  $N_{\text{Co}_{\text{Li}}^+ \text{-V}_{\text{Li}}^-}(y) = 0$  and bound pairs are electrically neutral, the flux law from Eq. (5.8) requires the number density  $c_{\text{Co}_{\text{Li}}^+ \text{-V}_{\text{Li}}^-}$  to be uniform throughout the film.
3. Because the concentration of bound pairs is uniform, the defect association/dissociation equilibrium, Eq. (5.10), requires that gradients in the  $\text{V}_{\text{Li}}^-$  and  $\text{Co}_{\text{Li}}^+$  concentrations are always opposed (i.e.,  $dc_{\text{V}_{\text{Li}}^-}/dy$  and  $dc_{\text{Co}_{\text{Li}}^+}/dy$  have opposite signs).
4. To maintain the electroneutrality condition from Eq. (5.7), gradients in the  $\text{V}_{\text{Li}}^-$  and  $p^+$  concentrations must have coincident directions (i.e.,  $dc_{\text{V}_{\text{Li}}^-}/dy$  and  $dc_{p^+}/dy$  have similar signs).

Before discussing the predictions of the transport model, it is first worth commenting on its connection to the equilibrium concentrations derived from Figure 5.2. As previously mentioned, these concentrations  $c_k^0$  establish a boundary condition at the  $\text{Li}_2\text{O}_2/\text{electrolyte}$  interface ( $y = 0$ ), where it is assumed

that equilibrium with  $O_2$ ,  $Li_2O_2$ , and  $LiCoO_2$  holds. Solving the transport model then yields the number densities as a function of position;  $c_k(y)$  varies spatially due to changes in the local electrochemical potential. Therefore, a solution to the transport model is akin to generating a formation-energy diagram (with a unique Fermi level) at each point  $y$  in the film based on the values of the electrochemical potentials there.

#### 5.4.5 Scenario I: Layer-by-layer stripping/deposition

By combining material continuity with the ion-blocking condition on Li and the fact that the bound-pair flux uniformly vanishes, it follows that the flux of Li-ion vacancies vanishes uniformly:  $N_{V_{Li}}(y) = 0$ . Thus all of the current is carried by hole polarons, as indicated in Figure 5.4. From the above equations, the current through a film of thickness  $L$  is shown to be

$$(5.15) \quad i = \frac{2eD_{p^+}c_{V_{Li}}^0}{L} \left[ 1 - \exp\left(\frac{e\Delta\Phi}{k_B T}\right) \right].$$

(Note that the diffusion coefficients of bound pairs and lithium vacancies do not appear here, because the net fluxes of these species vanish, as discussed above.) Eq. (5.15) predicts that the peroxide film acts like a diode: the negative current responds exponentially, allowing arbitrarily large anodic (recharge) currents ( $i < 0$ ), whereas the cathodic (discharge) current ( $i > 0$ ) saturates when  $|\Delta\Phi| \gg k_B T/e$ . Eq. (5.15) suggests a limiting cathodic current density of  $2eD_{p^+}c_{V_{Li}}^0/L$ . As discussed in Appendix C, however, electroneutrality does not hold in the positive current (discharge) regime of Scenario I because the  $Li_2O_2$ /electrode interface becomes starved of polarons and the charging of the double-layer at that interface accommodates most of the potential drop. In the Appendix C, we modify the model to account for electroneutrality violations and show that the discharge current indeed does saturate, but not at the value implied by Eq. (5.15). The correct limiting cathodic current density is approximately

$eD_{p^+}c_{p^+}^0/L$ , which for a 100 nm thick film corresponds to  $\sim 10^{-20}$   $\mu\text{A}/\text{cm}^2$ . This current is far smaller than experimentally observed current densities during discharge.

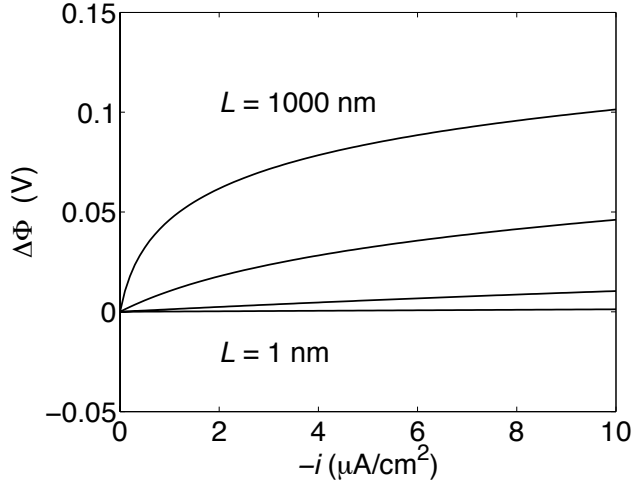


**Figure 5.5** Calculated potential drop as a function of current density for doped  $\text{Li}_2\text{O}_2$  films of thickness 1, 10, 100, and 1000 nm in Scenario I (layer-by-layer stripping/deposition).

Although only minimal discharge currents can be supported, recharge is predicted to be quite facile. Figure 5.5 shows the potential drop calculated from Eq. (5.15) as a function of anodic (recharge) current for various film thicknesses. The potential drop needed to drive recharge is quite small in the presence of Co dopants. For example, a potential drop of only 10 mV is needed to drive a current density of 1  $\mu\text{A}/\text{cm}^2$  through a 100 nm thick film. This current density is fairly representative of the microscopic current densities of typical Li- $\text{O}_2$  experiments<sup>53,79</sup> and would correspond to a 27-hour charge for a 100 nm thick film. (1  $\mu\text{A}/\text{cm}^2$  also is representative of the estimated microscopic current density required to achieve the macroscopic current density target described in Refs.<sup>15,70</sup>.) This result contrasts strongly with undoped  $\text{Li}_2\text{O}_2$ , whose low intrinsic conductivity is thought to be a performance-limiting factor.<sup>70,73,81</sup> Thus our results indicate that donor doping, such as through the incorporation of Co substitutions, can in principle moderate charge transport limitations in the Li- $\text{O}_2$  discharge product during recharge.

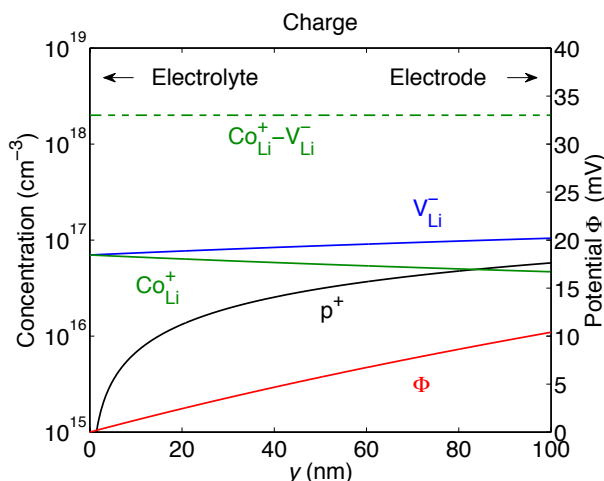


**Figure 5.6** Calculated defect concentrations and electrostatic potential for Scenario I (layer-by-layer stripping/deposition) in a 100 nm doped  $\text{Li}_2\text{O}_2$  film during charge at a current density of  $1 \mu\text{A}/\text{cm}^2$ .

Figure 5.6 shows the steady-state concentrations of defects and the electrostatic potential across the film for  $1 \mu\text{A}/\text{cm}^2$  charging of a 100 nm thick film. At the  $\text{Li}_2\text{O}_2$ /electrolyte interface ( $y = 0$ ), the addition of dopants lowers the number density of  $p^+$  and increases that of  $V_{\text{Li}}^-$  as the Fermi level shifts to higher energies (cf. Figure 5.2 and Eqs. (5.7) and (5.10)). As discussed above, the net  $V_{\text{Li}}^-$  flux must vanish. Thus the electrostatic force pushing lithium vacancies towards the electrode – a consequence of the rise in potential as  $y$  increases – must be balanced by an opposing force arising from a concentration gradient. Consequently the concentration of  $V_{\text{Li}}^-$  rises as one approaches the electrode (increasing  $y$ ) in Figure 5.5.

This gradient in the  $V_{\text{Li}}^-$  concentration is accompanied by a gradient in the  $p^+$  concentration with the same sign, as discussed above. As more Co is added to the film, the number density of  $V_{\text{Li}}^-$  at the  $\text{Li}_2\text{O}_2$ /electrolyte interface rises, and a larger gradient of  $V_{\text{Li}}^-$  concentration is needed to compensate the electric field. Consequently, increased doping leads to a larger  $p^+$  concentration gradient. In a highly doped sample, the  $p^+$  concentration will rapidly rise as one moves away from the  $\text{Li}_2\text{O}_2$ /electrolyte interface, resulting in an increased electronic film conductance during recharge.

The conclusion that Co substitutions should enhance charge transport during recharge may appear counter-intuitive, given that the addition of Co donors shifts the equilibrium Fermi level towards higher energies (Figure 5.2), thereby reducing the equilibrium polaron concentration. The present model reveals that this effect, which applies only as an equilibrium boundary condition at the  $\text{Li}_2\text{O}_2/\text{electrolyte}$  interface, is in fact offset by the conductivity enhancement associated with the accumulation of  $V_{\text{Li}}^-$  and  $p^+$  deeper into the film. The accumulation of  $V_{\text{Li}}^-$  and  $p^+$  represents a partial delithiation of the discharge product. Unlike Scenario II, however, this delithiation represents a concentration gradient of vacancies, rather than the formation of a new lithium-deficient phase.

#### 5.4.6 Scenario II: Two-phase delithiation

In the case of a delithiation recharge mechanism, one can combine continuity of mass and charge (Eqs. (5.5) and (5.6)), Faraday's law (Eq. (5.9)), and the boundary condition on hole polaron flux (Eq. (5.14)) to show that the flux of hole polarons vanishes everywhere. Thus all of the current is carried by Li-ion vacancies, consistent with the schematic in Figure 5.4b. The model's behavior is straightforward in the limit that the dopant concentration is much larger than the intrinsic defect concentration in the absence of impurities. It can be shown that the concentration of vacancies in this limit is uniform throughout the film, and the current-voltage relationship is Ohmic,

$$(5.16) \quad i = -\frac{e^2 D_{V_{\text{Li}}^-} c_{V_{\text{Li}}^-}^0 \Delta\Phi}{k_{\text{B}} T L}.$$

The effective conductivity  $e^2 D_{V_{\text{Li}}^-} c_{V_{\text{Li}}^-}^0 / k_{\text{B}} T$  is  $3 \times 10^{-9}$  S/cm. This is nine orders of magnitude larger than the predicted intrinsic ionic conductivity of crystalline  $\text{Li}_2\text{O}_2$ ,<sup>70</sup> and is high enough to provide adequate charge transport under typical conditions in a Li-O<sub>2</sub> cell. For example, a 1  $\mu\text{A}/\text{cm}^2$  current through a 100 nm thick film results in a potential drop of only 4 mV.

## 5.5 Discussion

The transport model predicts that doped  $\text{Li}_2\text{O}_2$  cannot support appreciable currents during discharge due to the limited charge transport supported by hole polarons, as shown in Eq. (5.15). (The contribution of lithium vacancies to conductivity is also limited, as it has been assumed that the electrode blocks their transport during discharge.) The fact that large  $\text{Li}_2\text{O}_2$  deposits are nevertheless observed in  $\text{Li-O}_2$  cells suggests that either:<sup>70</sup> (i.) alternative electronic charge transport pathways exist (e.g., surfaces<sup>70</sup> or grain boundaries<sup>83</sup>), or (ii.) particle growth can occur via the solution-mediated transport and subsequent precipitation of a soluble species<sup>42</sup> (e.g.,  $\text{LiO}_2$ ). The fact that very similar biconcave disk morphologies have been observed in the chemical deposition of unrelated systems supports the latter explanation.<sup>57,58</sup>

On the other hand, the model indicates that during recharge, charge transport in doped  $\text{Li}_2\text{O}_2$  is facile, regardless of whether the OER occurs via layer-by-layer stripping (Scenario I) or two-phase delithiation (Scenario II). We speculate that the improved transport properties of doped  $\text{Li}_2\text{O}_2$  may explain the reduced charging overpotentials observed in recent experiments on  $\text{Co}_3\text{O}_4$ -based  $\text{Li-O}_2$  electrodes.<sup>183</sup> This suggests that the doping of the discharge product may be a promising strategy for overcoming high charging overpotentials in  $\text{Li-O}_2$  batteries.

The doping of  $\text{Li-O}_2$  discharge products is unlike the *ex situ* doping of conventional semi-conducting materials or Li-ion battery materials (e.g.,  $\text{LiFePO}_4$ <sup>209,210</sup>). In  $\text{Li-O}_2$  cells the discharge product is in principle deposited and dissolved at every cycle. Therefore, any successful doping strategy must occur *in situ* during each charge/discharge cycle, and at a sufficient concentration. Black et al.<sup>183</sup> found that the ability of  $\text{Co}_3\text{O}_4$  to promote the OER was reproducible over many cycles, suggesting that if Co doping was indeed responsible for this

behavior, then the incorporation of Co occurred repeatedly. The mechanism for OER promotion suggested here may also explain the lowered charging potentials observed in cells preloaded with  $\text{Li}_2\text{O}_2$  when Pt, Ru, or various transition metal oxides were included.<sup>110,182,190,199</sup> In these cases, dopant incorporation may have occurred *ex situ* via sonication or stirring.<sup>110,182</sup>

Of course the relative importance of different discharge/recharge mechanisms may also be influenced by experimental details such as positive electrode support material, depth of discharge, system cleanliness, *etc.* These factors are not included in the present model. For example, several studies have suggested that when the discharge product is a thin film ( $\sim 4$  nm or less), charge transport through  $\text{Li}_2\text{O}_2$  occurs via electron tunneling.<sup>53,73,211</sup> The present model is intended to capture transport through thicker deposits (10-1000 nm) where electron tunneling is thought to be negligible.

Finally, the enhancement of charge transport predicted by the model developed here differs from the ‘polaron preemption’ mechanism recently hypothesized for  $\text{Li}_2\text{O}_2$  that is highly doped ( $\sim 2\%$ ) with silicon.<sup>157</sup> The polaron preemption mechanism involves a change to the host’s electronic structure, driven by a high level of impurities. In contrast, the present mechanism involves a change in the dynamic equilibrium between vacancies and polarons due to the introduction of trace (ppm-level) impurities.

Understanding of the mechanism by which promoters enhance the oxygen evolution reaction is an important step in the rational design of Li-O<sub>2</sub> electrode materials. Here a multi-scale model has been developed that can explain the ability of  $\text{Co}_3\text{O}_4$  to promote oxidation of bulk  $\text{Li}_2\text{O}_2$  and consequently improve the voltaic efficiency of Li-O<sub>2</sub> batteries.<sup>110,182,183,199</sup> The promotion effect is hypothesized to arise from enhanced electronic and/or ionic transport within the discharge product due to *in situ* doping of the  $\text{Li}_2\text{O}_2$  discharge phase with Co. This hypothesis is supported by calculations, which show that thick  $\text{Li}_2\text{O}_2$  deposits doped with Co can support large recharge current densities with only minimal overpotentials. In particular, a  $\text{Li}_2\text{O}_2$  film doped at ppm low levels will have an effective conductivity of  $10^{-9}$  S/cm or higher during recharge, regardless of

whether decomposition occurs via layer-by-layer stripping or two-phase delithiation. Under typical experimental conditions, a conductivity of this magnitude would reduce contributions to the overpotential from charge-transport limitations to the order of millivolts. Although the proposed mechanism is not ‘catalytic’ in the traditional sense, it may provide insight into the effect (or non-effect) of various putative catalysts on the Li-O<sub>2</sub> OER.

## Chapter 6: $\text{Li}_2\text{O}_2$ surfaces

### 6.1 Introduction

Lithium peroxide ( $\text{Li}_2\text{O}_2$ ) surfaces can play an important role in many processes in non-aqueous Li- $\text{O}_2$  batteries, including deposition/dissolution of the discharge product,<sup>89,90,158</sup> electrolyte decomposition,<sup>95,98,108</sup> and – potentially – charge transport.<sup>68,82</sup> A few computational studies have sought to identify the low-energy surfaces of  $\text{Li}_2\text{O}_2$ ,<sup>68,90,158,212</sup> and also the kinetics of deposition/dissolution at those surfaces.<sup>89–91,158</sup> Additionally, simulations have been performed to explore the electronic structure of  $\text{Li}_2\text{O}_2$  surfaces,<sup>67,82</sup> and in particular the presence of unpaired spins associated with superoxide ( $\text{O}_2^-$ ) dimers. Some computational studies have also examined interactions between  $\text{Li}_2\text{O}_2$  surfaces and common Li- $\text{O}_2$  battery solvents<sup>95,108</sup> and electrode support materials.<sup>53,84,165,211</sup> One study has also explored  $\text{Li}_2\text{O}_2$  grain boundaries.<sup>83</sup>

The purpose of this chapter is to (i.) systemically determine the thermodynamics and electronic structure of  $\text{Li}_2\text{O}_2$  surfaces and (ii.) elucidate the defect chemistry of the low-energy terminations. Previous computational studies that sought to identify low-energy  $\text{Li}_2\text{O}_2$  surfaces used semilocal functionals. However, the prevalence of surface compensating charge predicted at low energy  $\text{Li}_2\text{O}_2$  surfaces and the poor description of self-trapping in bulk  $\text{Li}_2\text{O}_2$  by semilocal functionals (see Chapter 4) suggests that a higher level of theory may be necessary. Thus our work builds upon these prior studies by properly accounting for self-trapping of surface compensating charge through the use of a hybrid functional and the exploration of alternative surface reconstructions.

## 6.2 Methods

### 6.2.1 Surface formation energies

The formation energy of a surface  $\gamma$  is defined in analogy to the formation energy of a point defect in Section 2.3.1:<sup>68,213</sup>

$$(6.1) \quad \gamma = \frac{1}{2A} \left[ E_{\text{slab}}^{\text{DFT}} - N_{\text{Li}} \mu_{\text{Li}} - N_{\text{O}} \mu_{\text{O}} \right],$$

where  $E_{\text{slab}}^{\text{DFT}}$  is the ground-state energy of a supercell containing a symmetric slab (whose two surfaces are separated by a suitably large vacuum region),  $A$  is the cross-sectional area of the slab,  $N_i$  is the number of atoms of species  $i$  in the slab, and  $\mu_i$  is the chemical potential of species  $i$ . When an  $\text{Li}_2\text{O}_2$  surface is at equilibrium with the bulk, the chemical potentials of Li and O are related by  $\mu_{\text{Li}} + \mu_{\text{O}} = \frac{1}{2} G_{\text{Li}_2\text{O}_2}$ , where  $G_{\text{Li}_2\text{O}_2}$  represents the free energy of bulk  $\text{Li}_2\text{O}_2$ . Eq. (6.1) can then be written as

$$(6.2) \quad \gamma = \frac{1}{2A} \left[ G_{\text{slab}} - \frac{1}{2} N_{\text{Li}} G_{\text{Li}_2\text{O}_2} + (N_{\text{Li}} - N_{\text{O}}) \mu_{\text{O}} \right].$$

Here we neglect vibrational contributions to free energy and so approximate the free energies  $G_{\text{slab}}$  and  $G_{\text{Li}_2\text{O}_2}$  with the DFT ground-state energies  $E_{\text{slab}}^{\text{DFT}}$  and  $E_{\text{Li}_2\text{O}_2}^{\text{DFT}}$ . The chemical potential of oxygen is set by assuming equilibrium with  $\text{O}_2$  gas at ambient conditions, and is calculated as discussed in Section 2.3.1. Throughout this work we employ a mixing parameter of  $\alpha = 0.48$  for all HSE calculations, as discussed in Section 2.2.2. Lattice constants were determined by the PBE exchange-correlation functional.

### 6.2.2 *Surface reconstruction*

We consider the possibility of the surface compensating charge becoming self-trapped at  $\text{Li}_2\text{O}_2$  surfaces. By ‘compensating charge’, we mean the deviation in the charge state of the ions near the surface from the charge state these ions nominally exhibit in the bulk material. (Note that the surface slabs in our calculations are constrained to be electrically neutral overall.) Compensating charges arise in order to satisfy electrostatic stability: if the repeating unit of the surface slab (parallel to the surface normal) has a net dipole moment, then an electrostatic divergence (‘polar catastrophe’) will arise if the surface ions retain the same charge state they have in the bulk.<sup>214,215</sup> This instability can be resolved by a depletion or accumulation of charge at the surface, resulting in a change in the charge state of surface ions.

A related concept is the idea of surface stoichiometry. This refers not to the local stoichiometry of the surface layer *per se*, but rather to the relative numbers of cations and anions within the entire symmetric slab. It is nevertheless frequently the case that the slab stoichiometry and surface stoichiometry are the same. (We note that some low-symmetry crystals do not permit the construction of symmetric slabs along some Miller indices, and so the concept of stoichiometry is more complex in these cases.) In general, non-stoichiometric surfaces are polar, meaning that they require a compensating charge for electrostatic stability, while stoichiometric surfaces are non-polar. In a symmetric slab DFT simulation of a non-stoichiometric (polar) surface, the compensating charge naturally arises from the stoichiometry. In other words, because the stoichiometry of the slab does not match the stoichiometry of the crystal, some ions will necessarily deviate from their normal charge state. One can easily determine the amount of compensating charge from the relative number of cations and anions in the cell, or equivalently by making a Tasker diagram.<sup>214</sup>

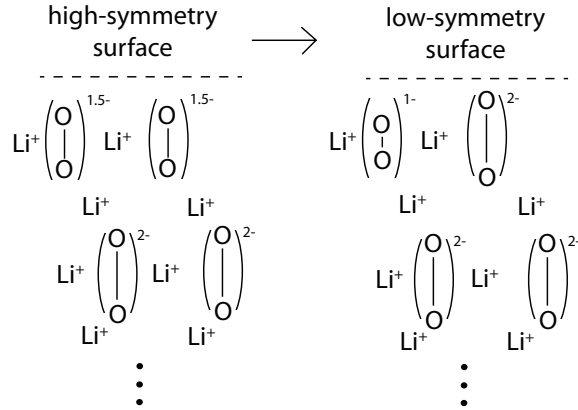


**Figure 6.1** Conceptual illustration of surface compensating charge self-trapping at the {0001} O-rich-1 termination. Left: pristine surface before symmetry breaking. Right: distorted surface after self-trapping.

In some cases, the compensating charge will be distributed in such a way that some surface ions have a fractional charge. As an example, we consider the  $\text{Li}_2\text{O}_2$  {0001} O-rich-1 termination, which in our prior calculations we found to be the lowest energy surface when using the semilocal PBE exchange-correlation functional.<sup>68,82</sup> A compensating charge of  $+\frac{1}{2}e$  per surface unit cell is achieved by the depletion of surface oxygen p states, causing the surface  $\text{O}_2$  dimers to be in a nominal charge state of  $-1.5$ , as illustrated in the left panel of Figure 6.1. Given holes in bulk  $\text{Li}_2\text{O}_2$  will self-trap<sup>69,70,74</sup> (as discussed in Chapter 3), we speculated that the compensating charge at the {0001} terminations could also become self-trapped: instead of each surface oxygen dimer receiving a compensating charge of  $+\frac{1}{2}e$ , half of the dimers could receive a compensating charge of  $+e$  while the other half received no compensating charge. In this case half of the surface oxygen dimers are in a  $-2$  (peroxide) charge state, while the other half are in a  $-1$  (superoxide) charge state. This mixed-valence surface is illustrated in the right panel of Figure 6.1, and can be thought of as a 50% occupancy of hole polarons in the surface  $\text{O}_2$  layer.

We tested the stability of such a distortion by replicating the {0001} unit cell into a  $2 \times 1$  supercell and breaking the symmetry between  $\text{O}_2$  surface dimers by manually adjusting the  $\text{O}_2$  bond length and Li-O distances to mimic the geometry of peroxide and superoxide (i.e., hole polaron) dimers in bulk  $\text{Li}_2\text{O}_2$ . Relaxations

showed that while HSE finds this distortion to be energetically favorable, PBE does not. (Even when starting from the broken-symmetry HSE structure, PBE calculations returned to the high-symmetry geometry.) This discrepancy is not surprising, as self-interaction error in GGAs<sup>117,118</sup> destabilizes hole polarons in bulk  $\text{Li}_2\text{O}_2$ .<sup>70,74</sup>

The higher stability of this mixed-valence reconstruction on the  $\{0001\}$  O-rich-1 surface demonstrates that surface compensating charge can indeed self-trap. In order to systematically study a large number of different surfaces, we need a general procedure to test for surface compensating charge self-trapping. We adopt the following strategy:

1. The compensating charge per surface unit cell  $q$  is determined for each surface. This can be simply calculated from the stoichiometry of a symmetric slab as  $q = (N_- v_- - N_+ v_+)/2$ , where  $N_{\pm}$  is the number of cations/anions in the cell and  $v_{\pm}$  is the charge of the cations/anions (the factor of two arising from the fact that there are two surfaces on a slab). In the general case, the compensating charge can be determined from a Tasker diagram.<sup>214</sup>
2. The species on which the compensating charge resides was identified. In the case of  $\text{Li}_2\text{O}_2$ , we found that compensating charges (both positive and negative) preferred to  $\text{O}_2$  molecular orbitals. We came to this conclusion by examining the O-O bond length (which serve as a proxy for the charge state) and by visual inspection of the magnetization density. That the compensating charge resides on the oxygen atoms is expected since both the conduction and valence bands in  $\text{Li}_2\text{O}_2$  are derived from oxygen p states.
3. The compensating charge per symmetry equivalent surface ion (of the species determined in step 2) was calculated. Here we count polyatomic ions (e.g.,  $\text{O}_2^{2-}$ ) as a single ion.

4. If the compensating charge per ion calculated in step 3 is not an integer, then we tested for charge self-trapping. To do this, we manually adjusted bonds to break the symmetry between symmetry-equivalent surface ions, and then re-relaxed the cell. In many cases this requires replicating the surface unit cell to allow for a lower-symmetry reconstruction.

Following the above procedure, we found that only 4 of the 23 surfaces considered exhibit fractional-charges: {0001} O-rich-1, O-rich-2, Li-rich-1, and Li-rich-2. In all four cases, HSE calculations found symmetry-breaking distortions to be energetically favorable. In contrast, PBE calculations favored distortions only for the Li-rich-2 termination. This behavior is consistent with our prior calculations showing that in bulk  $\text{Li}_2\text{O}_2$ , GGAs find electron polarons to be stable but hole polarons to be unstable.<sup>70,74,156</sup> As we discuss below, self-interaction error and symmetry-lowering reconstructions can be important not only for the surface geometries, but also for the thermodynamics and electronic structure of these terminations. The results presented below for these four terminations use the structure (high-symmetry or low-symmetry) that is most energetically favorable for each functional.

### 6.2.3 Defect chemistry

The calculations of defect thermodynamics and kinetics are carried out in the manner described in Chapter 2. For the {0001} stoichi-4 surface, a  $3 \times 2$  supercell of the surface unit cell (144 atoms total) was used. For the {1-100} stoichi-3 surface, a  $4 \times 2$  supercell of the surface unit cell (256 atoms total) was used. Large supercells were selected in order to minimize spurious interactions between periodic images of the defects.

The Makov-Payne finite-size correction<sup>147</sup> as originally formulated is not applicable to surface slabs because the dielectric constant is non-uniform in a cell which contains both a solid region and a vacuum region. As a first approximation, we nevertheless employ the same finite-size correction as used for bulk  $\text{Li}_2\text{O}_2$ , as described in Appendix A. This is motivated by the fact that the supercell sizes

used for surface defect calculations are similar in size to that used for defect calculations in bulk  $\text{Li}_2\text{O}_2$  (Chapter 3). Size convergence tests for surface defects, shown in Appendix A, support this choice.

### 6.3 Surface thermodynamics and electronic structure

Figure 6.2 and Table 6.1 compare the surface formation energies calculated by the PBE and HSE functionals. Although the formation energies of the majority of surfaces examined are not very sensitive to the choice of functional, in a few cases notable differences exist. For example, the formation energies of the {0001} O-rich-1 surface calculated by the PBE and HSE functionals are 17 and 53 meV/Å. We note that this surface is one of the four that undergoes a symmetry-lowering reconstruction in HSE calculations.

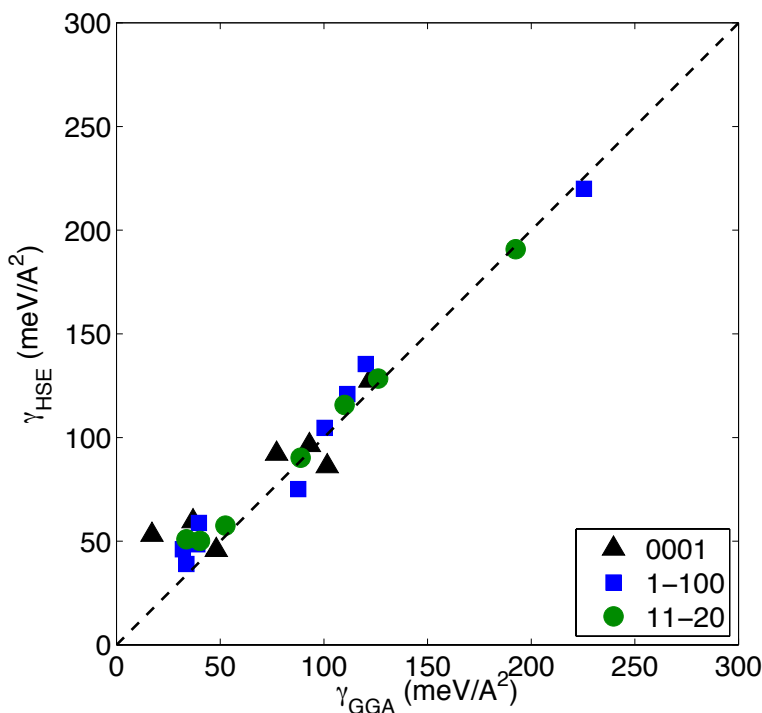


**Figure 6.2** Comparison of GGA and HSE surface formation energies.

Because of the differences in surface energies, the equilibrium crystallite shapes predicted by the two functionals are qualitatively different, as shown in Figure 6.3. While PBE predicts the low energy terminations to be oxygen-rich, HSE predicts the low energy terminations to be stoichiometric. Furthermore, the aspect ratio of the equilibrium crystallite shape differs, with the HSE functional

predicting a prism that is prolate (i.e., greater in height than width) and the PBE functional predicting an prism that is oblate (i.e., greater in width than height).

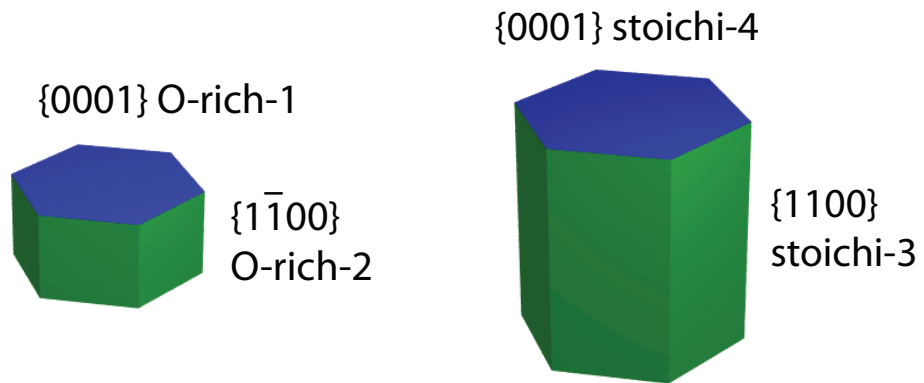


**Figure 6.3** Equilibrium crystallite shapes predicted from (a) PBE and (b) HSE surface energies.

**Table 6.1** Surface formation energies and surface band gaps calculated from PBE and HSE. For both functionals, the lowest energy surface for each Miller index is written in bold.

	$\gamma^{\text{PBE}}$ (meV/Å <sup>2</sup> )	$\gamma^{\text{HSE}}$ (meV/Å <sup>2</sup> )	$E_{\text{gap}}^{\text{PBE}}$ (eV)	$E_{\text{gap}}^{\text{HSE}}$ (eV)	
{0001}	Li-rich-1	77	92	-0.49	3.06
	Li-rich-2	93	96	0.22	4.00
	O-rich-1	<b>17</b>	53	-0.83	3.14
	stoichi-1	102	86	0.21	4.92
	stoichi-2	37	60	-0.23	2.82
	stoichi-3	122	127	-0.26	3.33
	stoichi-4	48	<b>46</b>	1.66	4.71
	{1-100}	Li-rich-1	225	220	-0.15
Li-rich-2		100	105	1.04	4.11
Li-rich-3		120	135	0.7	3.84
O-rich-1		39	48	0.05	4.48
O-rich-2		<b>32</b>	46	0.08	4.34
O-rich-3		40	59	0.08	4.25
stoichi-1		111	121	0.75	3.26
stoichi-2		88	75	0.12	4.82
stoichi-3	34	<b>39</b>	2.38	5.41	
{11-20}	half-oxy-1	126	128	1.16	3.56
	half-oxy-2	110	116	2.12	4.89
	half-oxy-3	89	90	2.61	5.76
	Li-rich	192	191	0.41	2.55
	O-rich-1	40	<b>50</b>	0.18	4.48
	O-rich-2	<b>34</b>	51	0.19	4.56
	stoichi	53	58	2.12	5.94

In addition to differences in surface thermodynamics, these functionals exhibit important differences in electronic structure. While PBE predicts many surfaces to be metallic or nearly-metallic, HSE predicts all but one surface, {1-100} Li-rich-1, to be insulating, as shown in Figure 6.4 and Table 6.1. Here the band gap is calculated as the difference between the highest eigenvalue of the band  $N$  and the lowest eigenvalue of band  $N - 1$ , where  $N$  is the number of electrons in per unit cell; thus a negative band gap is indicative of metallic behavior. The band-decomposed charge density (not shown) indicates that the metallicity at the

{1-100} Li-rich-1 surface is associated with surface states associated with surface Li sites.

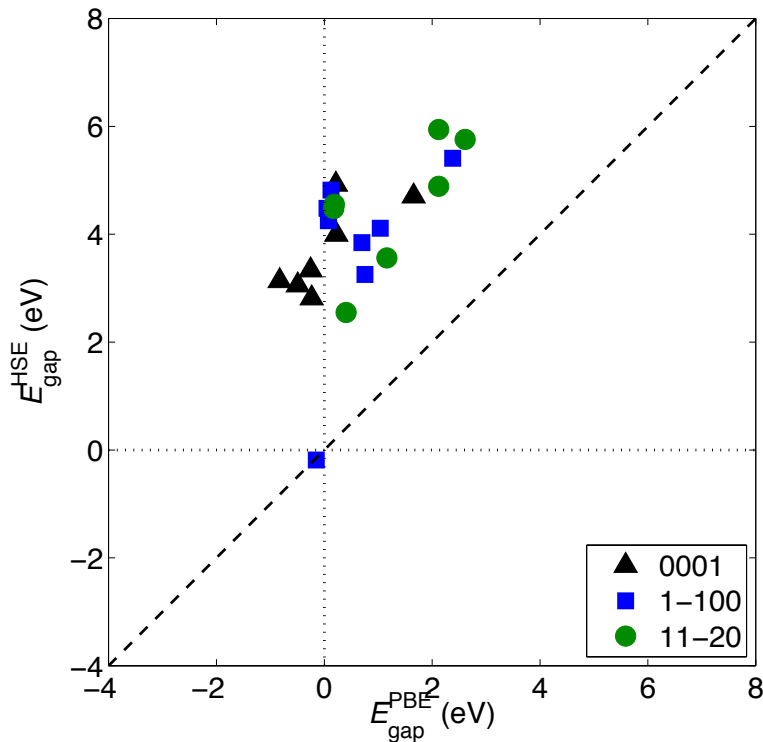
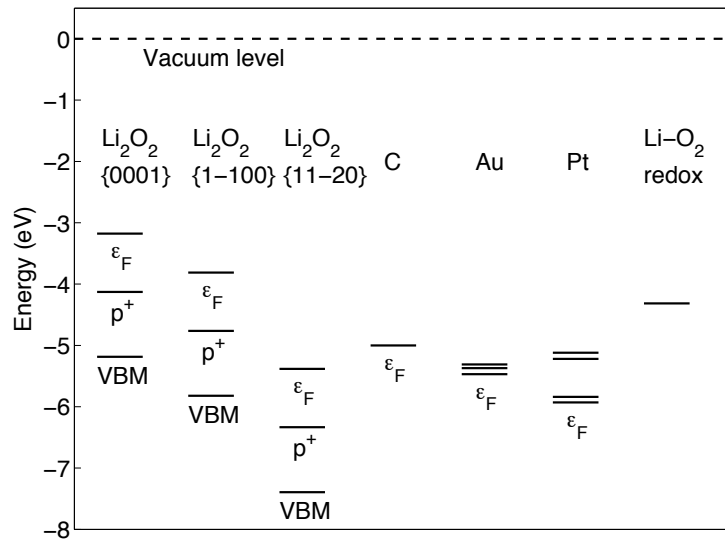


**Figure 6.4** Comparison of GGA and HSE surface band gaps.

Figure 6.5 shows the alignment of the relevant energy levels in a  $\text{Li-O}_2$  electrode. The valence band maximum (VBM) has been aligned to the vacuum through HSE slab calculations, using the electrostatic potential at the oxygen atomic cores to align the potentials in bulk and slab calculations.<sup>216</sup> The position of the hole polaron level and intrinsic Fermi level of  $\text{Li}_2\text{O}_2$  relative to the VBM is taken from the hole polaron formation energy calculated in Chapter 3. (By VBM, we mean the highest occupied states in the bulk, which may be lower than the highest occupied surface states.)

Importantly, the intrinsic Fermi level of  $\text{Li}_2\text{O}_2$  at the surfaces which appear on the equilibrium crystallite shape, {0001} stoichi-4 and {1-100} stoichi-3, lies above the Fermi levels of C, Au, and Pt. This suggests that when these materials are brought into contact with  $\text{Li}_2\text{O}_2$ , hole polarons will accumulate in the  $\text{Li}_2\text{O}_2$  near the interface due to charge transfer, forming a space-charge layer. The positive charge associated with the accumulation of hole polarons in the  $\text{Li}_2\text{O}_2$

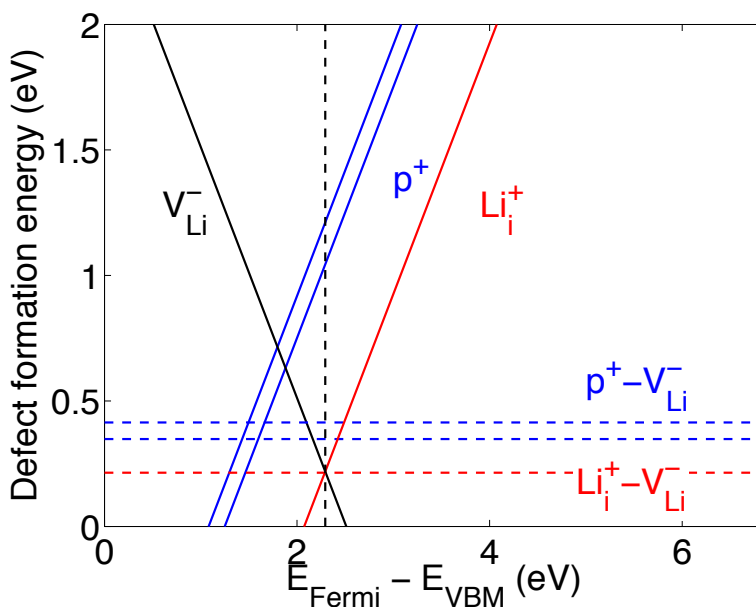
would be compensated for by the accumulation of electrons on the other side of the interface. Similarly, the fact that the  $\text{Li}_2\text{O}_2$  intrinsic Fermi level lies above  $\text{Li-O}_2$  redox potential suggests that hole polarons may accumulate at the  $\text{Li}_2\text{O}_2$ -electrolyte interface in a  $\text{Li-O}_2$  cell. In this case, the charge would be compensated by salt anions in the electrolyte.



**Figure 6.5** Alignment of the  $\text{Li}_2\text{O}_2$  valence band maximum (VBM), hole polaron level, and intrinsic Fermi level with the Fermi levels of common  $\text{Li-O}_2$  materials<sup>202</sup> and the  $\text{Li-O}_2$  redox potential.<sup>12,217,218</sup>

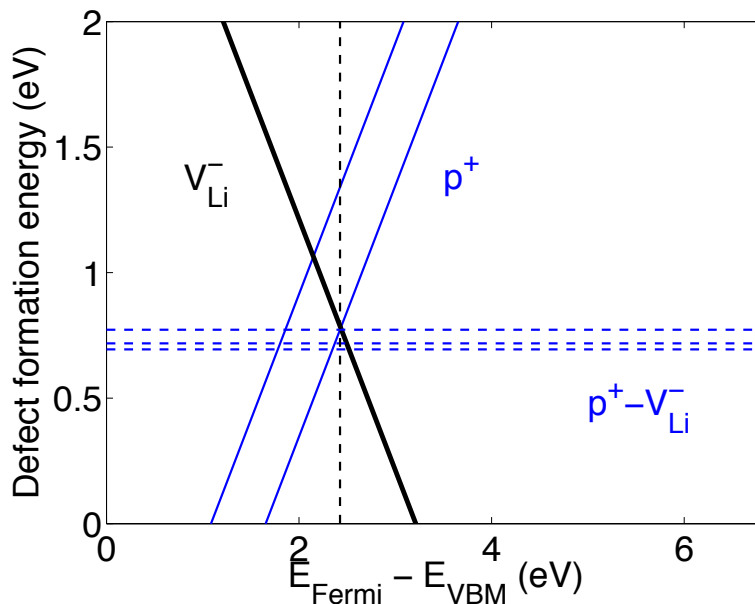
## 6.4 Surface defect chemistry

To explore how the presence of surfaces may affect charge transport in the  $\text{Li}_2\text{O}_2$  discharge product, we have explored the defect chemistry of the two surfaces predicted by HSE to terminate the equilibrium crystallite:  $\{0001\}$  stoichi-4 and  $\{1-100\}$  stoichi-3. Defect formation energies for the  $\{0001\}$  stoichi-4 surface are shown in Figure 6.6. Like bulk  $\text{Li}_2\text{O}_2$ , the lowest energy negative defect at this surface is a Li-ion vacancy ( $V_{\text{Li}}^-$ ). However, unlike bulk  $\text{Li}_2\text{O}_2$ , the lowest energy positive defect at this surface is a Li-ion interstitial. The interstitial represents the insertion of a  $\text{Li}^+$  ion into a vacant octahedral Li site in the surface layer (a site which would be occupied in the bulk crystal). Thus the defect chemistry of the  $\{0001\}$  stoichi-4 surface is disorder on the partially occupied surface Li sublattice (i.e., Frenkel disorder).



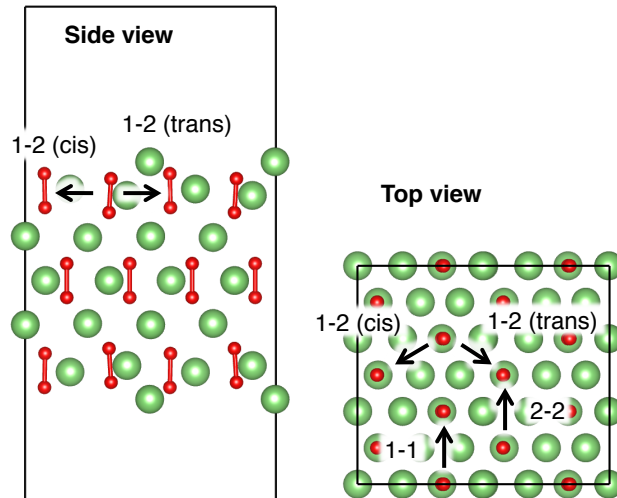
**Figure 6.6** Defect formation energy plot for the  $\{0001\}$  stoichi-4 surface.

Figure 6.7 shows the defect formation energies for the  $\{1-100\}$  stoichi-3 surface. The defect chemistry of this surface is similar to bulk  $\text{Li}_2\text{O}_2$ , consisting of hole polarons and Li-ion vacancies.



**Figure 6.7** Defect formation energy plot for the  $\{1-100\}$  stoichi-3 surface.

We next considered the dynamics of polarons at the  $\{0001\}$  stoichi-4 and  $\{1-100\}$  stoichi-3 surfaces. (We do not investigate Li-ion dynamics because in a Li-O<sub>2</sub> cell, the Li<sub>2</sub>O<sub>2</sub> surfaces are in contact with the electrolyte which has a high ionic conductivity; hence the transport of Li-ions along surfaces would not be expected to provide any reduction in charge-transport losses.) Nearest-neighbor hopping along the surface was considered. Figure 6.8 shows the four symmetry inequivalent pathways for hopping amongst the two symmetry inequivalent polaron sites at the  $\{0001\}$  stoichi-4 surface. The energy profiles, shown in Figure 6.9, indicate that hopping barriers at this surface are no lower than in bulk Li<sub>2</sub>O<sub>2</sub> (0.42-0.71 eV<sup>70</sup>).



**Figure 6.8.** Hole polaron hopping pathways on the {0001} stoichi-4 surface.

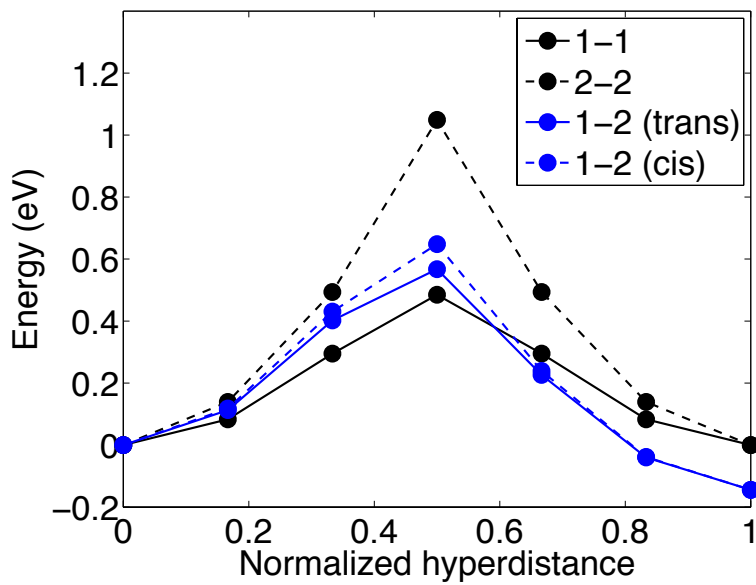


**Figure 6.9.** Energy profiles for hole polaron hopping at the {0001} stoichi-4 surface.

Figure 6.10 shows the three symmetry inequivalent hopping paths amongst the two symmetry inequivalent polaron sites at the {1-100} stoichi-3 surface. The energy profiles, shown in Figure 6.11, again indicate that the barriers are no lower at this surface than in bulk  $\text{Li}_2\text{O}_2$ .

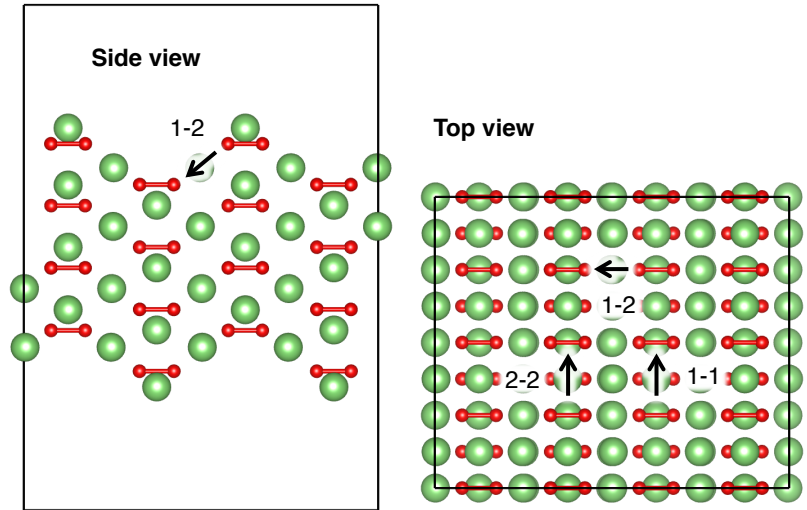


Figure 6.10 Hole polaron hopping pathways on the  $\{1-100\}$  stoichi-3 surface.

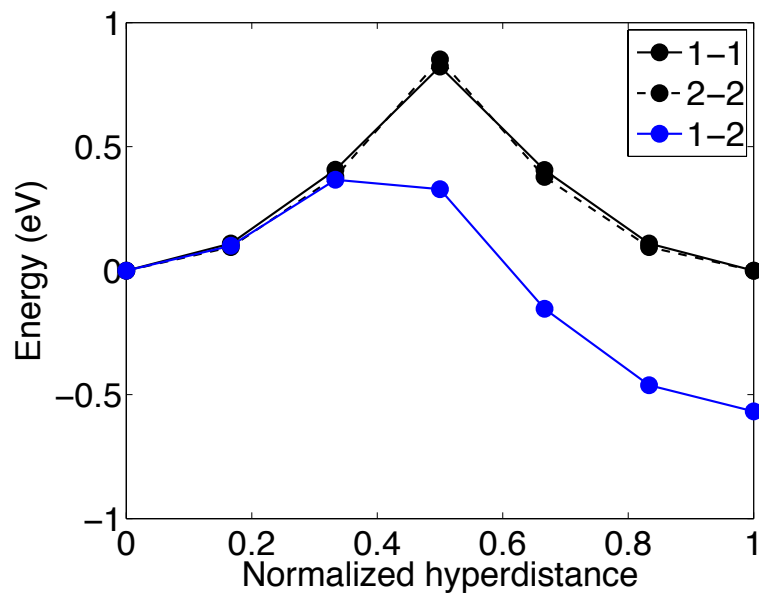


Figure 6.11 Energy profiles for hole polaron hopping at the  $\{1-100\}$  stoichi-3 surface.

## 6.5 Discussion

The data in Table 6.1 show that PBE and HSE give qualitatively different descriptions of the thermodynamics and electronic structure of  $\text{Li}_2\text{O}_2$  surfaces. These differences can largely be attributed to self-interaction error, which causes semi-local functionals (such as PBE) to overbind delocalized states.<sup>117,118</sup> Consequently, PBE will disfavor the self-trapping of surface charges. The delocalized states will lead to metallic behavior, and due to self-interaction error<sup>117,118</sup> cause surface formation energies to be underestimated. Because the incorporation of exact exchange in HSE corrects for these delocalization errors, self-trapping can be stabilized and the correct electronic structure obtained. That HSE is more reliable than PBE for predicting the self-trapping of surface charge at these surfaces is supported by the agreement in bulk band edge positions with *GW* calculations, as discussed in Section 2.2.2, and by the agreement with experiments regarding the self-trapping of holes in bulk  $\text{Li}_2\text{O}_2$ , as discussed in Chapter 3.

The equilibrium crystallite shape predicted by HSE (Figure 6.3) is prolate; in contrast, the crystallites observed in  $\text{Li-O}_2$  cells are typically oblate.<sup>52</sup> This suggests that the crystallite shapes in the  $\text{Li-O}_2$  discharge product are determined by factors beyond interfacial energy, such as mass transport or deposition kinetics.<sup>89-91,158</sup>

Conductivity is ultimately determined by the energy to form a polaron at the hopping transition state (see Chapters 2 and 4), and so depends on both the formation energy and hopping barrier. The lowest transition state energies  $E_t = E_f + E_a$  at the {0001} stoichi-4 and {1-100} stoichi-3 surfaces are 1.70 and 1.62 eV, which are higher than the polaron transition state energy in bulk  $\text{Li}_2\text{O}_2$  (1.37 eV). This suggests that there is no inherent enhancement of conductivity at  $\text{Li}_2\text{O}_2$  surfaces.

However, in the context of a Li-O<sub>2</sub> battery, Li<sub>2</sub>O<sub>2</sub> surfaces are in contact with other cell components, such as the positive electrode support material and the liquid electrolyte. The energy level alignment shown in Figure 6.5 shows that the Fermi level of common support materials are significantly below the intrinsic Fermi level of Li<sub>2</sub>O<sub>2</sub> for the {0001} stoichi-4 and {1-100} stoichi-3 surfaces, suggesting that a positively charged space charge layer will accumulate on the Li<sub>2</sub>O<sub>2</sub> side of the Li<sub>2</sub>O<sub>2</sub>/electrode interface. (That is, an increase in the concentration of hole polarons.) Similarly, the fact that the Li-O<sub>2</sub> redox couple lies below the Li<sub>2</sub>O<sub>2</sub> Fermi level for these surfaces suggests that a positively charged space charge layer will accumulate on the Li<sub>2</sub>O<sub>2</sub> side of the Li<sub>2</sub>O<sub>2</sub>/electrolyte interface. Furthermore, the fact that the hole polaron level for the {0001} stoichi-4 and {1-100} stoichi-3 surfaces lies above the Fermi level of the support materials and above the Li-O<sub>2</sub> redox potential suggests that the amount of charge on the space charge layer could be significant (i.e., a large fraction of polaron sites could be occupied). An enhancement in the concentration of polarons near interfaces would increase the electronic conductivity in these regions. The implications of a space charge layer for charge transport are explored in more detail in Chapter 7.

From a methodological point of view, this work demonstrates that the electronic and thermodynamic properties of Li<sub>2</sub>O<sub>2</sub> surfaces can depend upon both (i.) the exchange-correlation functional used, particularly in cases where self-interaction errors are important, and (ii.) the existence of symmetry-breaking distortions which allow for self-trapping of charge. In light of these results, prior calculations on Li<sub>2</sub>O<sub>2</sub> interfaces<sup>84</sup> and grain boundaries,<sup>83</sup> as well as prior calculations predicting metallic surfaces on other oxides,<sup>219</sup> may need to be revisited.

## Chapter 7: Space-charge effects in thin films

### 7.1 Introduction

While Chapters 3-6 have focused on transport through bulk materials, we now consider transport phenomenon in nano-scale deposits. This question is motivated by (i.) the widespread occurrence of nano-scale films or particles in Li-O<sub>2</sub> cells<sup>42,53,59</sup> (ii.) DFT calculations indicating that the Fermi level at Li<sub>2</sub>O<sub>2</sub> interfaces in Li-O<sub>2</sub> batteries could be pinned to low energies (Figure 6.5 and prior studies<sup>53,211</sup>). These calculations suggest that the intrinsic Fermi level of Li<sub>2</sub>O<sub>2</sub> is higher than the Fermi level of common electrode materials, as well as the Li-O<sub>2</sub> redox potential. This suggests that in nano-scale deposits, space-charge layers may form wherein hole polarons accumulate near the interfaces.

To this end, we have built a 1D transport model based on non-electroneutral Nernst-Planck theory to study the transport of hole polarons through thin Li<sub>2</sub>O<sub>2</sub> films in Li-O<sub>2</sub> batteries. The key result of the model is that space-charge effects can explain ‘sudden death’ behavior (i.e., a rapid drop in potential with increasing film thickness during a galvanostatic discharge<sup>53,73</sup>). When the thickness of the film exceeds the thickness of the space-charge layer, electrochemistry becomes limited by slow charge transport. We demonstrate that this model is in good agreement with discharge curves from flat-electrode experiments.

## 7.2 Formulation of the model

Our model is intended to be as simple as possible, while still capturing the essential physics of a pinned  $\text{Li}_2\text{O}_2$  film. We assume the film to be at quasi-steady-state, meaning that diffusional relaxations associated with local accumulation of material occur very rapidly in comparison to the timescale of interest, and also that the film thickness changes sufficiently slowly on this timescale that the velocity of the peroxide-film/electrolyte boundary can be neglected.

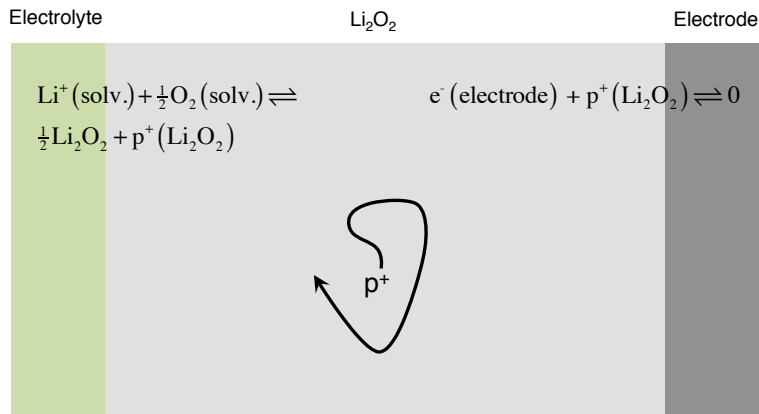


**Figure 7.1:** Schematic of transport model.

Our 1D model is conceptually illustrated in Figure 7.1. The most fundamental equation governing the model described continuity of charge, which requires that the current be divergence free at steady state:  $di/dy = 0$ . The electrostatic potential inside the  $\text{Li}_2\text{O}_2$  film is determined by Poisson's equation:

$$(7.1) \quad \frac{d^2\Phi}{dy^2} = -\frac{\rho}{\epsilon},$$

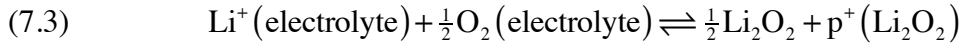
where  $\epsilon$  is the dielectric constant of the film (which we assume to be isotropic) and  $\rho$  is the charge density.

A Nernst-Planck flux law describes the diffusion and migration of hole polarons:

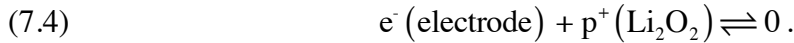
$$(7.2) \quad N = -\frac{DF}{RT}c \frac{d\Phi}{dy} - D \frac{dc}{dy}.$$

Here  $c$  is the polaron concentration,  $D$  is the polaron diffusion coefficient (assumed to be isotropic),  $F$  is Faraday's constant, and  $RT$  is the thermal energy. The flux of polarons  $\bar{N}$  is related to the flux of charge via Faraday's law,  $i = FN$ , and the polaron number density is related to the charge density via  $\rho = cF$ .

At the interface with the electrolyte, which we define to be  $y=0$ , the Li-O<sub>2</sub> redox reaction



is stipulated to be in equilibrium. This assumption is motivated by previous experiments and simulations which found the kinetics of the Li-O<sub>2</sub> redox couple to be facile.<sup>80</sup> At the electrode interface,  $y=L$ , we assume that electron transfer between the Li<sub>2</sub>O<sub>2</sub> and electrode support is in equilibrium:



The above reaction represents the transfer of one electron from the electrode to the Li<sub>2</sub>O<sub>2</sub> film. The concentration of polarons at the boundaries is taken to be fixed by mass action laws associated with (7.3) and (7.4):  $c(0) = c_1$  and  $c(L) = c_2$ .

The above equations represent the complete statement of the model, which can be simplified by introducing a dimensionless position  $\xi = y/L$  and dimensionless concentration  $\Theta(\xi) = c(y)/c_1$ . This dimensionless concentration obeys a governing equation:

$$(7.5) \quad 0 = \frac{d^2\Theta}{d\xi^2} - \beta^2\Theta^2 - j \frac{1}{\Theta} \frac{d\Theta}{d\xi} - \frac{1}{\Theta} \left( \frac{d\Theta}{d\xi} \right)^2,$$

where  $j = iL/FDc_1$  represents the dimensionless current and  $\beta = \sqrt{F^2L^2c_1/\epsilon RT}$  represents the dimensionless film thickness.  $\Theta$  satisfies the boundary conditions  $\Theta(0)=1$  and  $\Theta(1) = s \equiv c_2/c_1$ . The dimensionless voltage drop  $\Delta\phi = F[\Phi(L) - \Phi(0)]/RT$  can be expressed as:

$$(7.6) \quad \Delta\phi = -\int_0^1 \frac{j}{\Theta} d\xi - \log s.$$

The overpotential is given by

$$(7.7) \quad \eta_{\text{passivation}} = \frac{RT}{F} \left| \Delta\phi - (\Delta\phi)_{j=0} \right|.$$

### 7.3 Results

Analytic solutions to the model can be obtained for certain limits. We consider the limit that the dimensionless film thickness is large ( $\beta \rightarrow \infty$ ), but the current is small in the sense that  $j\beta^2 \rightarrow 0$ . In this case, we can transform Eq. (7.5)

with  $\Theta = \Theta'/\beta^2$  to obtain

$$(7.8) \quad 0 = \frac{d^2\Theta'}{d\xi^2} - \Theta'^2 - j\beta^2 \frac{1}{\Theta'} \frac{d\Theta'}{d\xi} - \frac{1}{\Theta'} \left( \frac{d\Theta'}{d\xi} \right)^2,$$

where  $\Theta'$  satisfies the boundary conditions  $\Theta'(0) = \Theta'(1) = \infty$ . In the regime where the  $j\beta^2$  term is negligible, the solution is

$$(7.9) \quad \Theta' = \frac{4\pi^2}{1 + \cos\left[2\pi\left(\xi - \frac{1}{2}\right)\right]}.$$

This yields  $\Delta\phi - (\Delta\phi)_{j=0} = -j\beta^2/4\pi^2$ , and an overpotential of

$$(7.10) \quad \eta = \frac{1}{4\pi^2} \frac{|j|L^3}{D\varepsilon}.$$

Eq. (7.10) demonstrates a few important points about the thick film/small current limit:

1. The overpotential in the limit does not depend on the boundary concentrations  $c_1$  and  $c_2$ ; consequently discharge and recharge are symmetric,  $\eta(-j) = \eta(j)$ .

2. The overpotential increases with the cube of the film thickness, illustrating the ‘sudden death’ behavior.
3. The overpotential does not depend on the temperature explicitly; however, the diffusion coefficient  $D$  will in general be sensitive to temperature (see Eq. (2.30)).

In the thin film limit ( $\beta \rightarrow 0$ ), one can neglect the  $\beta\Theta^2$  term in Eq. (7.5) and obtain an implicit current-voltage relationship:

$$(7.11) \quad \frac{s\Delta\phi + j}{\Delta\phi + j} e^{\Delta\phi} = 1.$$

The current-voltage relationship becomes Ohmic in the limits that the current is large or small:

$$(7.12) \quad \Delta\phi - \ln s = \begin{cases} -j/s & \text{when } j \ll -1 \\ j(1-s)/s \ln s & \text{when } |j| \ll 1 \\ -j & \text{when } j \gg 1 \end{cases}.$$

We present a numerical solution of Eq. (7.5) to compare our model to experiments. We additionally include the kinetics of the Li-O<sub>2</sub> couple, representing the cell potential as

$$(7.13) \quad U = E^0 \pm \eta_{\text{kinetic}} \pm \eta_{\text{passivation}},$$

where the upper (lower) sign applies for recharge (discharge).  $E^0$  is the equilibrium cell potential (2.96 V vs. Li/Li<sup>+12</sup>),  $\eta_{\text{passivation}}$  is given by Eq. (7.7), and  $\eta_{\text{kinetic}}$  is determined by the Butler-Volmer equation:

$$(7.14) \quad i = i_0 \left\{ \exp\left(-\frac{\alpha F \eta_{\text{kinetic}}}{RT}\right) - \exp\left[\frac{(1-\alpha) F \eta_{\text{kinetic}}}{RT}\right] \right\}.$$

For simplicity, we take the symmetry factor  $\alpha$  to be  $\frac{1}{2}$  and neglect the second term on the right hand side of Eq. (7.14), an approximation that is valid in the regime in which the kinetic overpotential is large compared to  $RT/F$ . Thus we express the kinetic overpotential as

$$(7.15) \quad \eta_{\text{kinetic}} = -2 \frac{RT}{F} \ln \frac{i}{i_0}.$$

Figure 7.2 shows the potential calculated from Eq. (7.13) as a function of capacity for various currents. The values of the free parameters (polaron diffusion coefficient  $D$ , the dielectric constant  $\epsilon$ , the exchange current density  $i_0$ , and the boundary concentrations  $c_1$  and  $c_2$ ) were adjusted by hand to match experimental galvanostatic discharge curves from flat electrode experiments.<sup>73</sup> (For simplicity, we set  $c_1 = c_2$ .) The values of these parameters and values reported elsewhere in the literature are summarized in Table 7.1. The fitted values for the polaron diffusion coefficient, dielectric constant and exchange current density are in reasonable agreement with reported values from calculations and experiments. No experimental or theoretical value for the boundary concentrations  $c_1$  and  $c_2$  has been reported, but our fitted value is physically reasonable in that it represents a small fraction ( $\sim 5\%$ ) of the concentration of polaron sites in the  $\text{Li}_2\text{O}_2$  lattice.

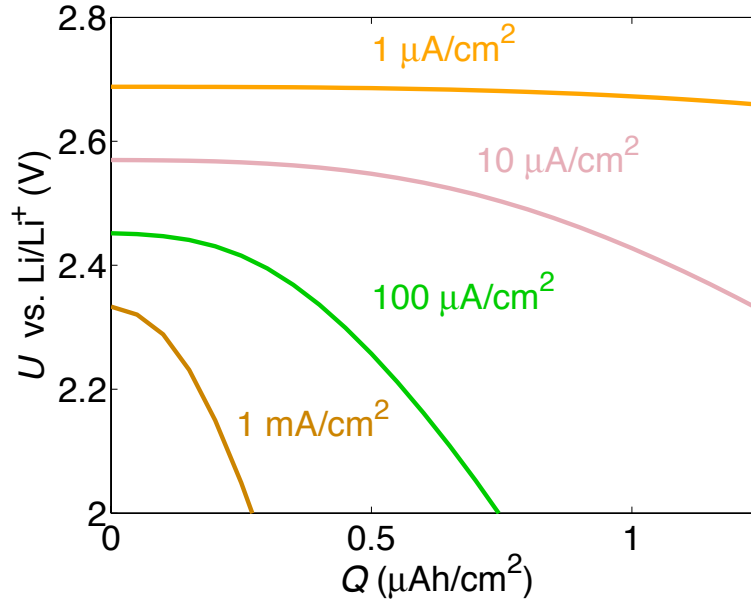


**Figure 7.2** Simulated potential as a function of discharge capacity for uniform  $\text{Li}_2\text{O}_2$  deposition.

**Table 7.1** Values of parameters used in the model and relevant values from the literature.

Parameter	Description	Value used in model	Other values reported
$D$	Polaron diffusion coefficient	$8 \times 10^{-13} \text{ cm}^2/\text{s}$	$9 \times 10^{-10} \text{ cm}^2/\text{s}$ (in-plane) <sup>70</sup> $2 \times 10^{-14} \text{ cm}^2/\text{s}$ (out-of-plane) <sup>70</sup>
$\epsilon$	$\text{Li}_2\text{O}_2$ dielectric constant	10	$\epsilon_{xx} = \epsilon_{yy} = 7.5$ ; $\epsilon_{zz} = 12.5$ <sup>70</sup>
$i_0$	Exchange current density	$5 \times 10^{-9} \text{ A}/\text{cm}^2$	$10^{-5} \text{ A}/\text{cm}^2$ <sup>99</sup> $10^{-9} \text{ A}/\text{cm}^2$ <sup>14</sup>
$c_1 = c_2$	Polaron concentration at interfaces	$8 \times 10^{20} \text{ cm}^{-3}$ (~5% occupancy)	

The curves in Figure 7.2 clearly illustrate the effect of electrical passivation: the potential drops with increasing thickness, and this drop increases with severity at higher current densities. The film does not behave as an Ohmic resistor: the magnitude of the charge transport overpotential increases superlinearly with film thickness (i.e., ‘sudden death’ behavior).

## 7.4 Discussion

Experiments have found that electrical passivation of the electrode by  $\sim 5$  nm of  $\text{Li}_2\text{O}_2$  can lead to the sudden death of Li- $\text{O}_2$  cells. Previously, this sudden death was suggested to occur when the film thickness exceeded the electron tunneling distance.<sup>53,73</sup> (However, depending on the electrode design, pore clogging can also cause sudden death.<sup>77,85</sup>) Our model shows that sudden death behavior is in fact consistent with polaron diffusion, and can occur when the film thickness exceeds the thickness of the space-charge layer. We hypothesize that polaron diffusion, not electron tunneling, is responsible for charge transport through thin films in Li- $\text{O}_2$  cells.

Luntz et al.<sup>73</sup> presented a model for electron transport through thin  $\text{Li}_2\text{O}_2$  films, and concluded that hole polaron transport could not explain the sudden death behavior observed in experiments, and therefore electron tunneling must be the primary transport mechanism. Our model, in contrast, indicates that hole polaron transport is indeed consistent with sudden death behavior. The reason for this difference is that the model of Luntz et al. assumes that the polaron concentration is uniform throughout the film. Our model illustrates that there are regimes where this assumption is not valid.

Whether transport is mediated by hole polarons or electron tunneling has implications for battery engineering. First, transport via hole polarons would be improved at higher temperatures due to the increase in the polaron diffusion coefficient, whereas electron tunneling would not be enhanced by increased temperatures. (In fact, defect and phonon scattering may make electron tunneling less facile at higher temperatures.)

Second, transport via hole polarons is sensitive to crystallographic orientation due to the anisotropy in the dielectric and polaron diffusion tensors. Although such anisotropies have been neglected in the present model, the fact that in-plane

polaron diffusion coefficient is  $5 \times 10^4$  times larger than the out-of-plane diffusion coefficient<sup>70</sup> (see Chapter 3) indicates that transport overpotentials will be lower in films where the {0001} axis lies in the plane of electrode surface.

Lastly, we discuss the asymmetry between discharge and charge observed in flat electrode experiments. The symmetry between discharge and charge in our model is broken only by the parameter  $s$  quantifying the ratio of the polaron concentrations at the  $\text{Li}_2\text{O}_2/\text{electrode}$  and  $\text{Li}_2\text{O}_2/\text{electrolyte}$  interfaces. However, no value of parameters in our model can reproduce two features in the charging curves observed by Luntz et al.<sup>73</sup> First, the overpotential rises as charging proceeds. This is inconsistent with our model because as charging proceeds, the film must become thinner and so overpotentials should decrease. Secondly, the overpotential observed experimentally by Luntz et al.<sup>73</sup> is not uniquely determined by the capacity and current. In fact, Figure S4 of that study indicates that the overpotential appears to be uniquely determined by the *fractional* capacity and current. This implies that there is some hidden variable that is changing as recharge proceeds, such as composition or morphology.

Luntz et al.<sup>73</sup> hypothesized that the accumulation of side reaction products could account for the rise in potential as charge proceeds. However, it is difficult to reconcile this hypothesis with the experimental observation that the shape of the potential vs. capacity curve varies with the initial thickness of the film (i.e., the thickness at the beginning of recharge). Presumably any accumulation of side reaction products on the surface would not be sensitive to the initial thickness of the film and so the shape would be independent of initial thickness.

The above observations suggest that the recharge mechanism in flat electrode experiments is in some way fundamentally different from the discharge mechanism. One possibility is that while discharge presumably occurs homogeneously, recharge could occur inhomogeneously. Perturbations to the smoothness of the film, which are stable during discharge, may be unstable during charge. That is, any dimple in the film will become amplified during recharge as charge transport is the most facile at the thinnest parts of the film. A second

possibility is that recharge could occur via the delithiation of the discharge product (either as a two-phase or solid-solution process).<sup>70,75</sup>

## Chapter 8: Conclusions

We have used density functional theory calculations and continuum transport models to elucidate how the degree of crystallinity, composition, presence of surfaces, and presence of space charge layers affect charge transport in  $\text{Li}_2\text{O}_2$ . The results of this work suggest that the following design guidelines could lead to improved performance in Li-O<sub>2</sub> cells:

1. Increase the operating temperature
2. Reduce the degree of crystallinity of the discharge product
3. Reduce the thickness of deposits
4. Increase the concentration of donor dopants
5. For crystalline deposits, orient the crystallites' *c* axes to be orthogonal to the electrode surface normal

Some of the points above suggestions are supported by experiments. Operating temperature (Item 1) is arguably the easiest variable to control experimentally, of those listed above. Indeed, experiments have found that increasing the operating temperature reduces charging overpotentials<sup>160,220,221</sup> and in some cases increases discharge capacity<sup>73,220</sup>, consistent with the hypothesis that hole polaron and/or Li-ion vacancy diffusion limits performance. Regarding Item 2, reducing the degree of crystallinity, experiments<sup>42,47,48</sup> have found evidence that amorphous or poorly-crystalline  $\text{Li}_2\text{O}_2$  can be electrochemically oxidized at lower overpotentials than crystalline  $\text{Li}_2\text{O}_2$ . This is consistent with our hypothesis that enhanced transport in amorphous  $\text{Li}_2\text{O}_2$  can enhance cell performance.

One avenue for further research would be to explore to what extent variation in electrode structure and/or composition could promote Items 2-5. Experiments have found that catalysts/additives might influence the degree of crystallinity of

the discharge product<sup>42,47,48</sup> (Item 2) and the thickness/morphology of the discharge product<sup>48,187</sup> (Item 3). However, the influence of the electrode's properties on the discharge product is not well understood. A more complete understanding of the deposition process<sup>51,59</sup> which elucidates this influence may accelerate the rational design of new Li-O<sub>2</sub> electrodes.

One of the overarching themes revealed by this work is that the tendency of peroxide, O<sub>2</sub><sup>2-</sup>, dimers in Li<sub>2</sub>O<sub>2</sub> to donate electrons to form superoxide dimers, O<sub>2</sub><sup>-</sup> (i.e., hole polaron). For example, this may occur when Li<sub>2</sub>O<sub>2</sub> is biased to moderately high potentials and forms either a solid solution<sup>70</sup> (as discussed in Chapter 3) or a topotactically delithiated LiO<sub>2</sub> phase.<sup>75</sup> The accumulation of hole polarons is also predicted to occur at low potentials in doped Li<sub>2</sub>O<sub>2</sub> (see Chapter 5 and Figure 5.6). And also, the accumulation of hole polarons to form a space-charge layer is predicted to occur at interfaces with the electrode support material and electrolyte in a Li-O<sub>2</sub> cell, as discussed in Chapters 6 and 7 (see Figure 6.5).

Indeed, a number of experiments have now demonstrated the presence of a superoxide component in both Li-O<sub>2</sub> discharge products<sup>65</sup> and also Li<sub>2</sub>O<sub>2</sub> powders.<sup>81</sup> The presence of a species that can readily change charge state makes Li<sub>2</sub>O<sub>2</sub> fundamentally different from Li<sub>2</sub>O and other non-transition-metal oxides. (For example, prior simulations and experiments have found that intrinsic conduction in Li<sub>2</sub>O is mediated by cationic Frenkel defects (i.e., Li<sub>i</sub><sup>+</sup> and V<sub>Li</sub><sup>-</sup>), which do not involve changes in charge state.<sup>222,223</sup>)

We conclude by considering how the present results relate to other non-aqueous metal-air battery chemistries. More specifically, we speculate that the capability for even a modest amount of electronic charge transport in the discharge phase could explain why some non-aqueous metal-air chemistries are rechargeable at moderate potentials, while others are not. For example, Li<sub>2</sub>O<sub>2</sub>,<sup>224-</sup><sup>226</sup> Na<sub>2</sub>O<sub>2</sub>,<sup>227</sup> NaO<sub>2</sub>,<sup>23</sup> and KO<sub>2</sub><sup>24</sup> can be electrochemically decomposed in non-aqueous environments at moderate overpotentials (~1 V or less); on the other hand Li<sub>2</sub>O and SiO<sub>2</sub> are apparently electrochemically inactive in this context.<sup>226,228-</sup><sup>230</sup> To rationalize these differences we recall that ionic solids in which the valence state can change tend to exhibit electronic conductivity due to the presence of

charge carriers.<sup>144,145</sup> Examples include transition metal oxides in which the cation species can change its valence state (e.g.,  $\text{TiO}_2$  or  $\text{ZnO}$ <sup>144,145</sup>). This differs, of course, from the behavior in peroxides and superoxides where it is the anion that can change valence state.

The results presented here suggest that the presence of  $\text{O}_2$  dimers in  $\text{Li}_2\text{O}_2$ ,  $\text{Na}_2\text{O}_2$ ,  $\text{NaO}_2$ , and  $\text{KO}_2$  may contribute to the rechargeability of these materials in non-aqueous metal-air batteries by providing a mechanism for charge transport. Although for  $\text{Li}_2\text{O}_2$  moderate charge overpotentials may be needed to activate charge transport, the decomposition of  $\text{NaO}_2$  and  $\text{KO}_2$  can occur with only minimal overpotentials.<sup>23,24</sup> For example, (as previously mentioned) earlier reports suggest that potassium superoxide exhibits a high conductivity at room temperature.<sup>207</sup>

In contrast, the absence of a species that can change valence state in  $\text{Li}_2\text{O}$  and  $\text{SiO}_2$  may account for the electrochemical inertness of these materials. For example, prior simulations and experiments have found that intrinsic conduction in  $\text{Li}_2\text{O}$  is mediated by cationic Frenkel defects (i.e.,  $\text{Li}_i^+$  and  $\text{V}_{\text{Li}}^-$ ),<sup>222,223</sup> and we do not expect the ionic conductivity associated with these defects to contribute to significant charge transport during cell operation because, as discussed in Chapter 5, the electrodes are ion-blocking.

The presence of species that can change its charge state may provide an important pathway for charge transport, and we propose that this feature explains why compounds containing  $\text{O}_2$  dimers can be electrochemically decomposed in non-aqueous metal-air cells. This has implications for the development of other non-aqueous metal-air chemistries: for cations that cannot change charge state (e.g., Li, Na, K, Mg), only peroxide and superoxide discharge products (and not oxides) would be expected to be rechargeable. On the other hand, transition metals that can change valence state in principle may yield rechargeable non-aqueous metal-air chemistries even if the discharge product is an oxide.

## Appendices

### Appendix A: Convergence tests

Figure A.1 shows the convergence of the positions of the valence band maximum (VBM) and conduction band minimum (CBM) with respect to the average electrostatic potential. These calculations were performed in a unit cell with a number of bands equal to 32, 64, 128, 256, 512, and 1024. Based on this data, we chose to use 1024 bands. An extrapolation to an infinite number of bands indicates that the band edges are converged to within about 50 meV.

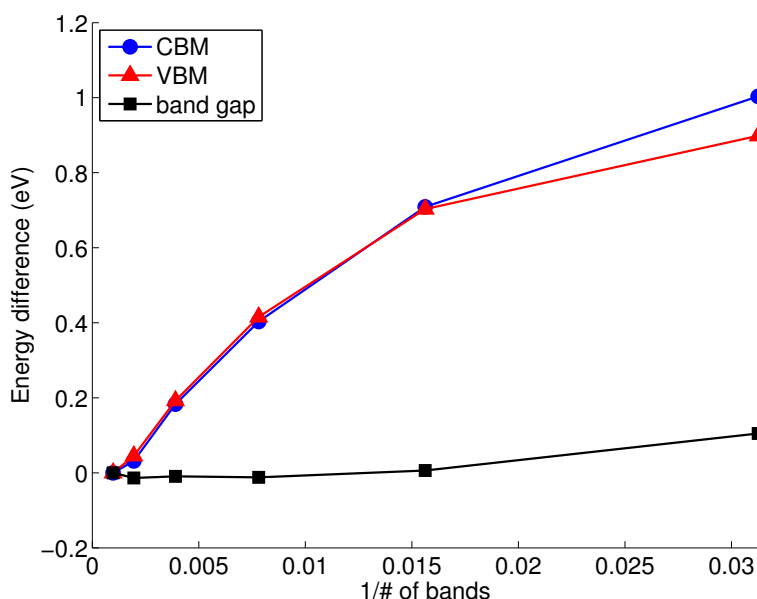


**Figure A.1** Convergence of the GGA+ $G_0W_0$  band edges and band gap with respect to the number of bands used in the calculation.

Next we discuss finite-size effects in our simulations. While more complicated finite-size corrections have been proposed, the monopole errors have been shown to be the leading error, scaling as one over the length of the supercell.<sup>148</sup> We note that the inclusion of the monopole correction is an improvement over previous studies on polarons in  $\text{Li}_2\text{O}_2$ , which did not include

any finite-size corrections.<sup>69,156</sup> Using density functional perturbation theory (with the PBE functional),<sup>231</sup> we have calculated the in-plane and out-of-plane relaxation (i.e., low-frequency) components of the dielectric tensor of  $\text{Li}_2\text{O}_2$  to be  $\epsilon_{xx} = \epsilon_{yy} = 7.48$  and  $\epsilon_{zz} = 12.54$ ; given the relatively modest anisotropy, we simply adopt a value of  $\epsilon = 10$  for the purposes of calculating finite-size corrections. This yields a correction of  $E_{\text{MP1}} = 0.17$  eV for defects with a charge of  $z = \pm 1$  in our  $3 \times 3 \times 2$  supercell.

Figure A.2 shows that the MP1 correction significantly improves size convergence for the  $\text{V}_{\text{Li}}^-$  (Oct) defect. We also performed some finite-size tests on the hole polaron, as shown in Figure A.3. However, because this defect is unstable in PBE, it was necessary to use a hybrid functional; consequently it was not possible to go to larger cell sizes. At small sizes, one can see that the hole polaron in HSE is more sensitive to supercell size than the negative lithium vacancy. Based on the magnetization density shown in Figure 3.6 we attribute this behavior to wavefunction overlap between periodic images.<sup>149</sup>

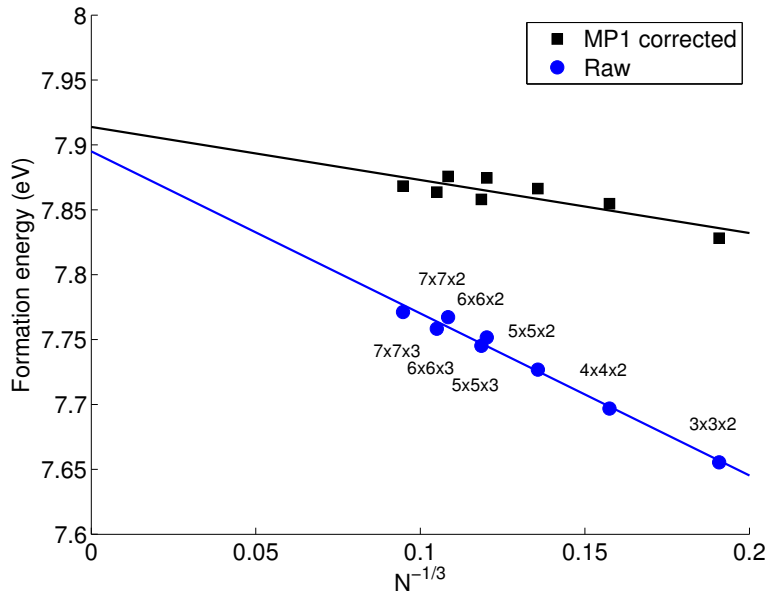


**Figure A.2** Size convergence of the  $\text{V}_{\text{Li}}^-$  (Oct) PBE formation energy referenced to the average electrostatic potential. Calculations were performed up to a  $7 \times 7 \times 3$  supercell ( $N = 1176$  atoms). A linear fit is shown to allow for extrapolation to infinite supercell size.

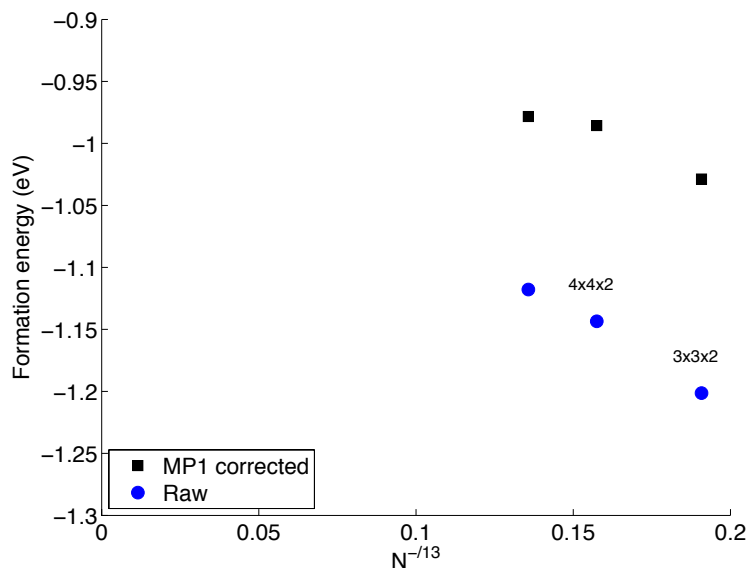


**Figure A.3** Size convergence of the hole polaron formation energy referenced to the average electrostatic potential calculated with HSE ( $\alpha = 0.48$ ). Calculations were performed up to a  $5 \times 5 \times 2$  supercell ( $N = 400$  atoms). We refrain from including a linear fit because the errors due to wavefunction overlap are not expected to have a linear dependence on the cell dimension.

Figure A.4 shows size convergence tests for a surface  $V_{Li}^-$  at the  $\{0001\}$  stoichi-4 termination performed with the PBE functional. We considered symmetric slabs (one defect on each side of the slab) and asymmetric slabs (a defect on only one side). In these size convergence tests, all dimensions of the cell (width, slab height, and vacuum height) were scaled approximately uniformly. Interestingly, the size convergence appears to be about the same for the symmetric and asymmetric slabs. Extrapolation to the dilute limit shows that the finite-size error in the 144 atom cell is about 0.25-0.3 eV.

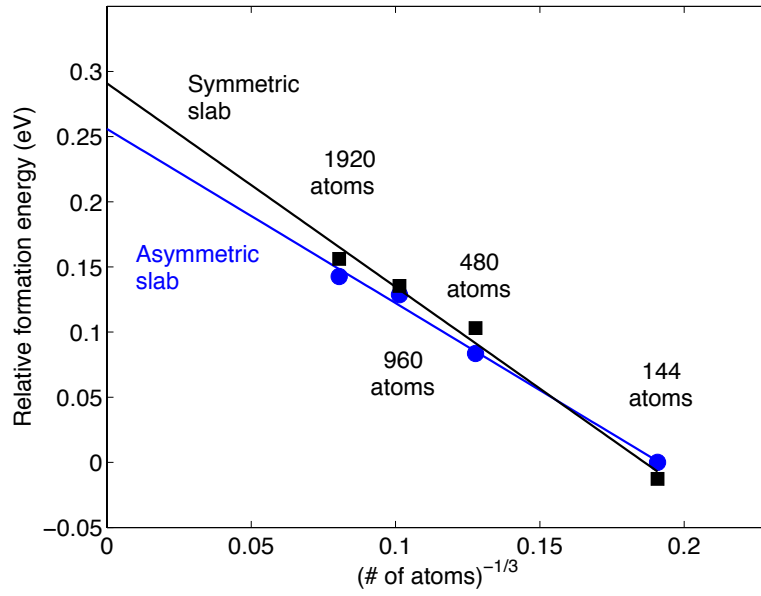


**Figure A.4** Size convergence of the surface  $V_{Li}^-$  formation energy (with the Fermi level set at the surface slab's valence band maximum). Formation energies are shown relative to the formation energy on the 144 atom asymmetric slab.

## Appendix B: Target conductivity estimate

We estimate the conductivity required for a hypothetical bipolar plate battery pack described by Adams and Karulkar.<sup>15</sup> We assume that the positive electrode uses carbon with a specific area of  $100 \text{ m}^2/\text{g}_C$ ,<sup>79</sup> and that  $\text{Li}_2\text{O}_2$  forms a film of uniform thickness. Based on the parameters shown in Table B.1, the film will be of thickness  $T = QV/4ae = 6 \text{ nm}$ , where  $e$  is the elementary charge and the factor of four arises from the fact that four electrons are transferred per unit cell of  $\text{Li}_2\text{O}_2$ . The carbon loading is  $L = E/NAUQ = 0.013 \text{ g}_C/\text{cm}^2$ , so the microscopic current density is  $j = i/aL = 3.4 \text{ }\mu\text{A}/\text{cm}^2$ . To achieve an  $iR$  drop across the discharge product of  $\eta = 0.1 \text{ V}$ , the conductivity must be  $\sigma = Tj/\eta = 2 \times 10^{-11} \text{ S}/\text{cm}$ . We assume an uncertainty of two orders of magnitude in this estimate.

**Table B.1** Parameters used to determine overpotential for a hypothetical Li-O<sub>2</sub> battery.

Parameter	Description	Units	Value
$Q$	Specific capacity	C/g <sub>C</sub>	1650
$E$	Pack energy	Wh	40
$N$	Number of cells	Dimensionless	1434
$i$	Macroscopic current density	mA/cm <sup>2</sup>	42
$A$	Plate active area	cm <sup>2</sup>	500
$U$	Cell voltage	V	2.7
$V$	Li <sub>2</sub> O <sub>2</sub> unit cell volume	Å <sup>3</sup>	64
$a$	Specific area of carbon	m <sup>2</sup> /g <sub>C</sub>	100

### Appendix C: Electroneutrality violations

As discussed in Chapter 5, electroneutrality violations must be accounted for to properly describe discharge in Scenario I. (In contrast, recharge in Scenario I, as well as recharge and discharge in Scenario II, can be correctly described within the electroneutral model.) Local electroneutrality is a valid approximation on the interior of the domain so long as the length scale of the system is larger than the screening length.<sup>232</sup> Indeed, for our system, the screening length (~10 nm) is smaller than system size of interest (10-1000 nm). However, an important caveat is that even when the system size is large compared to the screening length, electroneutrality violations at the boundaries (i.e., double layer charging) can play an important role in determining the current-voltage relationship. For example, if deviations from electroneutrality in these regions are not accounted for, then one obtains the unphysical result that the polaron concentration during discharge in Scenario I can be negative. When electroneutrality violations are accounted for, the hole polaron concentration is prevented from going below zero by the accumulation of charge in the double layer at the  $\text{Li}_2\text{O}_2/\text{electrode}$  interface. This phenomenon can be illustrated by solving the non-electroneutral model in the appropriate regime.

The non-electroneutral formulation of the model is identical to the electroneutral model presented in the main text, except that (i.) the electroneutrality constraint is replaced with Poisson's equation:

$$(C.1) \quad \frac{d^2\Phi}{dy^2} = -\frac{e}{\epsilon} \sum_k z_k c_k ,$$

and (ii.) the mass action law for the exchange of electrons across the  $\text{Li}_2\text{O}_2/\text{electrode}$  interface,  $\text{p}^+(\text{p}) + \text{e}^-(\text{s}) \leftrightarrow 0$ , is employed as an additional boundary condition:

$$(C.2) \quad c_{\text{p}^+}(L)c_{\text{e}^-}(L) = K.$$

Here  $c_{\text{e}^-}(L)$  represents the concentration of electrons on the electrode side of the  $\text{Li}_2\text{O}_2/\text{electrode}$  interface. Eq. (C.2) can be written as  $c_{\text{p}^+}(L) = c_{\text{p}^+}^1$  where  $c_{\text{p}^+}^1 = K/c_{\text{e}^-}(L)$ . (In principle,  $c_{\text{p}^+}^1$  could depend on the electric field; however for the purposes of the present analysis the exact value of  $c_{\text{p}^+}^1$  is not important.)

The model can be simplified through the introduction of the dimensionless position  $\xi$ , the dimensionless electric field  $\Sigma$ , the dimensionless fluxes  $\text{N}_k$ , and the dimensionless concentrations  $\theta_k$ :

$$(C.3) \quad \xi = \frac{y}{L} \quad \Sigma = \frac{LeE}{k_{\text{B}}T} \quad \text{N}_k = \frac{LN_k}{D_k c_k^0} \quad \theta_k = \frac{c_k}{c_k^0}.$$

Introducing a ‘charge-carrier strength’  $c_q^0 = c_{\text{p}^+}^0 + c_{\text{VLi}^-}^0 + c_{\text{CoLi}^+}^0$  and a screening length  $\lambda = \sqrt{k_{\text{B}}T\epsilon/e^2 c_q^0}$  defines a dimensionless expression of film thickness in units of screening length,  $\Lambda = L/\lambda$ . Finally, we express the equilibrium concentrations as fractions of the charge-carrier strength,  $w_k^0 = c_k^0/c_q^0$ . With these variables the model can be re-cast in a dimensionless form:

$$(C.4) \quad \frac{d \ln \theta_{\text{VLi}^-}}{d\xi} = -\Sigma$$

$$(C.5) \quad \frac{d \ln \theta_{p^+}}{d \xi} = \Sigma - \frac{N_{p^+}}{\theta_{p^+}}$$

$$(C.6) \quad \frac{d \Sigma}{d \xi} = \Lambda^2 \left[ w_{p^+}^0 \theta_{p^+} - \left( 1 - w_{p^+}^0 - w_{CoLi^+}^0 \right) \theta_{V_{Li}} + w_{CoLi^+}^0 \frac{1}{\theta_{V_{Li}}} \right].$$

The boundary conditions are  $\theta_{p^+}(0) = 1$ ,  $\theta_{V_{Li}}(0) = 1$ , and  $\theta_{p^+}(1) = \theta_{p^+}^1$ . This model can be solved explicitly in the regime that all of the following conditions are satisfied:

1.  $w_{p^+}^0 \ll 1$  (i.e., the polaron concentration is small)
2.  $\Lambda \gg 1$  (i.e., the film thickness is large compared to the screening length)
3.  $c_{p^+}(0) - c_{V_{Li}}(0) + c_{CoLi^+}(0) = 0$  (i.e., no double layer forms at the  $Li_2O_2$ /electrolyte interface)

Condition 3 is included so that the analysis can focus on double layer formation at the  $Li_2O_2$ /electrode interface. In principle, double layers could form at both interfaces, but one can neglect the double layer at the  $Li_2O_2$ /electrolyte interface when the film thickness is large compared to the screening length (Condition 2).

From Condition 1, we can simplify Eq. (C.6) to

$$(C.7) \quad \frac{d \Sigma}{d \xi} = \frac{\Lambda^2}{2} \left[ \frac{1}{\theta_{V_{Li}}} - \theta_{V_{Li}} \right],$$

where we have employed  $w_{p^+}^0 + w_{V_{Li}}^0 + w_{CoLi^+}^0 = 1$  and Condition 3 above to find that

$w_{V_{Li}}^0 = w_{CoLi^+}^0 = \frac{1}{2}$ . Let  $\phi = \frac{e[\Phi - \Phi(0)]}{k_B T}$  and  $\xi' = (L - y)/\lambda$ . Then Eq. (C.4) can be

integrated, and Eq. (C.7) can be expressed as

$$(C.8) \quad \frac{d^2\phi}{d\xi'^2} = -\sinh\phi .$$

The boundary conditions on the dimensionless potential are  $\phi(0) = \Delta\phi$  and  $\phi(\Lambda) = 0$ . When  $\Lambda \gg 1$ , the solution is

$$(C.9) \quad \phi(\xi') = 4 \tanh^{-1} \left[ \tanh \left( \frac{\Delta\phi}{4} \right) \exp(-\xi') \right].$$

We are interested in the limiting current, i.e., the current when  $\Delta\phi \rightarrow \infty$ . In this limit Eq. (C.9) simplifies to

$$(C.10) \quad \phi(\xi') = 4 \tanh^{-1} [\exp(-\xi')].$$

Substituting this into our equation for the polaron concentration (Eq. (C.5)) yields:

$$(C.11) \quad \frac{d \ln \theta_{p^+}}{d\xi} = 4\Lambda \tanh^{-1} \left\{ \exp[-\Lambda(1-\xi)] \right\} - \frac{N_{p^+}}{\theta_{p^+}} .$$

Note that  $N_{p^+} = 1$  represents the ‘polaron extinction’ discharge current in the electroneutral model, i.e., the current at which the polaron concentration reaches zero at the  $\text{Li}_2\text{O}_2/\text{electrode}$  interface. We show now that no (continuous) solution with  $N_{p^+} > 1$  exists in the non-electroneutral model through proof by contradiction. In the outer region,  $\xi \gg \Lambda^{-1}$ , the first term on the right side of Eq. (C.11) is negligible yielding a linear solution  $\theta_{p^+} = (1-\xi)N_{p^+}$ .

Suppose that there exists a solution with  $N_{p^+} > 1$ . Then the polaron concentration would be negative in some region of the outer solution. Since the

polaron concentration is non-negative at  $\xi=1$ , then (assuming that the concentration is a continuous function) there must be a zero crossing with positive slope. In other words, there exists some  $\xi_{\text{crit}}$  such that

$$(C.12) \quad \left( \frac{d\theta_{p^+}}{d\xi} \right)_{\xi=\xi_{\text{crit}}} > 0 \text{ and } \theta_{p^+}(\xi_{\text{crit}}) = 0.$$

Rewriting Eq. (C.11) as

$$(C.13) \quad \frac{d\theta_{p^+}}{d\xi} = \theta_{p^+} 4\Lambda \tanh^{-1} \left\{ \exp[-\Lambda(1-\xi)] \right\} - N_{p^+}$$

and inserting Eq. (C.12) yields  $N_{p^+} < 0$ , which contradicts our original supposition that  $N_{p^+} > 1$ . Therefore the flux of polarons cannot exceed  $N_{p^+} = 1$  in the non-electroneutral model.

To illustrate this quantitatively, Figure C.5 shows the dimensionless concentration profiles and electric field for a 100 nm film in which the discharge current is saturated. Here for simplicity we have taken  $\theta_{p^+}^1 = 0$ . The drop in vacancy concentration and increase in electric field near  $\xi=1$  signifies the formation of a double layer at the  $\text{Li}_2\text{O}_2/\text{electrode}$  interface.

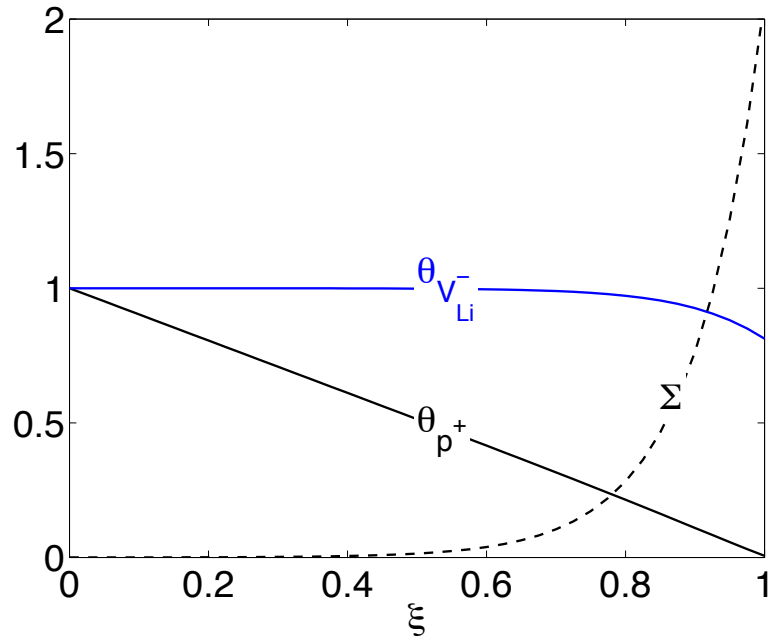


**Figure C.5** Dimensionless concentration and electric field in a 100 nm  $\text{Li}_2\text{O}_2$  film when the discharge current is saturated in the non-electroneutral model.

## References

- (1) Chu, S.; Majumdar, A. Opportunities and Challenges for a Sustainable Energy Future. *Nature* **2012**, *488*, 294–303.
- (2) Krause, F.; Müller-Reißmann, K.-F. *Energie-Wende : Wachstum Und Wohlstand Ohne Erdöl Und Uran ; Ein Alternativ-Bericht Des Öko-Institut, Freiburg*; Fischer: Frankfurt am Main, 1981.
- (3) IPCC. Summary for Policymakers. In *Climate Change 2014: Mitigation of Climate Change*; Cambridge University Press: Cambridge, UK, 2014.
- (4) Graham, J. D.; Messer, N. M.; Hartmann, D.; Lane, B. W.; Carley, S.; Crookham, C. Plug-in Electric Vehicles: A Practical Plan for Progress. **2011**.
- (5) *Multi-Path Transportation Futures Study : Vehicle Characterization and Scenario Analyses*; 2009.
- (6) Bruce, P.; Freunberger, S.; Hardwick, L. Li-O<sub>2</sub> and Li-S Batteries with High Energy Storage. *Nat. Mater.* **2012**, *11*, 19–30.
- (7) Christensen, J.; Albertus, P.; Sánchez-Carrera, R. S.; Lohmann, T.; Kozinsky, B.; Liedtke, R.; Ahmed, J.; Kojic, A. A Critical Review of Li/Air Batteries. *J. Electrochem. Soc.* **2012**, *159*, R1.
- (8) Girishkumar, G.; McCloskey, B.; Luntz, a. C.; Swanson, S.; Wilcke, W. Lithium-Air Battery: Promise and Challenges. *J. Phys. Chem. Lett.* **2010**, *1*, 2193–2203.
- (9) Kraytsberg, A.; Ein-Eli, Y. Review on Li–air batteries—Opportunities, Limitations and Perspective. *J. Power Sources* **2011**, *196*, 886–893.
- (10) Lee, J.-S.; Tai Kim, S.; Cao, R.; Choi, N.-S.; Liu, M.; Lee, K. T.; Cho, J. Metal-Air Batteries with High Energy Density: Li-Air versus Zn-Air. *Adv. Energy Mater.* **2011**, *1*, 34–50.
- (11) Lu, Y.-C.; Gallant, B. M.; Kwabi, D. G.; Harding, J. R.; Mitchell, R. R.; Whittingham, M. S.; Shao-Horn, Y. Lithium-Oxygen Batteries: Bridging Mechanistic Understanding and Battery Performance. *Energy Environ. Sci.* **2013**, *6*, 750.
- (12) Chase Jr., M. W. *NIST-JANAF Thermochemical Tables*; 1998.

- (13) Gallagher, K. G.; Goebel, S.; Greszler, T.; Mathias, M.; Oelerich, W.; Eroglu, D.; Srinivasan, V. Quantifying the Promise of Lithium–air Batteries for Electric Vehicles. *Energy Environ. Sci.* **2014**.
- (14) Imanishi, N.; Luntz, A. C.; Bruce, P. *The Lithium Air Battery : Fundamentals*.
- (15) Adams, J.; Karulkar, M. Bipolar Plate Cell Design for a Lithium Air Battery. *J. Power Sources* **2012**, *199*, 247–255.
- (16) Vergnes, M. Improvement in the Construction of Voltaic Gas-Batteries, 1860.
- (17) Shao, Y.; Ding, F.; Xiao, J.; Zhang, J.; Xu, W.; Park, S.; Zhang, J.-G.; Wang, Y.; Liu, J. Making Li-Air Batteries Rechargeable: Material Challenges. *Adv. Funct. Mater.* **2013**, *23*, 987–1004.
- (18) Heise, G. W.; Schumacher, E. A. An Air-Depolarized Primary Cell with Caustic Alkali Electrolyte. **1932**, *291*, 383–391.
- (19) Reddy, T. B.; Linden, D. *Handbook of Batteries*; McGraw-Hill Companies: New York, 2011.
- (20) Mohamad, A. A.; Mohamed, N. S.; Alias, Y.; Arof, A. K. Mechanically Alloyed Mg<sub>2</sub>Ni for Metal-Hydride–air Secondary Battery. **2003**, *115*, 161–166.
- (21) Lu, J.; Li, L.; Park, J.-B.; Sun, Y.-K.; Wu, F.; Amine, K. Aprotic and Aqueous Li-O<sub>2</sub> Batteries. *Chem. Rev.* **2014**, *114*, 5611–5640.
- (22) Hayashi, K.; Shima, K.; Sugiyama, F. A Mixed Aqueous/Aprotic Sodium/Air Cell Using a NASICON Ceramic Separator. *J. Electrochem. Soc.* **2013**, *160*, A1467–A1472.
- (23) Hartmann, P.; Bender, C. L.; Vračar, M.; Dürr, A. K.; Garsuch, A.; Janek, J.; Adelhelm, P. A Rechargeable Room-Temperature Sodium Superoxide (NaO<sub>2</sub>) Battery. *Nat. Mater.* **2013**, *12*, 228–232.
- (24) Ren, X.; Wu, Y. A Low-Overpotential Potassium-Oxygen Battery Based on Potassium Superoxide. *J. Am. Chem. Soc.* **2013**, *135*, 2923–2926.
- (25) Downing, B. W. Metal – Air Technology. In *Electrochemical Technologies for Energy Storage and Conversion*; 2012.
- (26) Shiga, T.; Hase, Y.; Yagi, Y.; Takahashi, N.; Takechi, K. Catalytic Cycle Employing a TEMPO–Anion Complex to Obtain a Secondary Mg–O<sub>2</sub> Battery. *J. Phys. Chem. Lett.* **2014**, *5*, 1648–1652.
- (27) Hosseiny, S. S.; Saakes, M.; Wessling, M. A Polyelectrolyte Membrane-Based Vanadium/air Redox Flow Battery. *Electrochem. commun.* **2011**, *13*, 751–754.

- (28) Walker, C. W.; Walker, J. Molybdenum/air Battery and Cell Design, 2012.
- (29) Zhao, X.; Gong, Y.; Li, X.; Xu, N.; Huang, K. A New Solid Oxide Molybdenum–air Redox Battery. *J. Mater. Chem. A* **2013**, *1*, 14858.
- (30) Zhao, X.; Li, X.; Gong, Y.; Xu, N.; Romito, K.; Huang, K. A High Energy Density All Solid-State Tungsten–Air Battery. *Chem. Commun. (Camb)*. **2013**, *49*, 5357–5359.
- (31) Wagner, O. C. Secondary Cadmium–Air Cells. *J. Electrochem. Soc.* **1969**, *116*, 693.
- (32) Mori, R. A Novel Aluminium–air Secondary Battery with Long-Term Stability. *RSC Adv.* **2014**, *4*, 1982.
- (33) Zhong, X.; Zhang, H.; Liu, Y.; Bai, J.; Liao, L.; Huang, Y.; Duan, X. High-Capacity Silicon–Air Battery in Alkaline Solution. *ChemSusChem* **2012**, *5*, 177–180.
- (34) Cohn, G.; Starosvetsky, D.; Hagiwara, R.; Macdonald, D. D.; Ein-Eli, Y. Silicon–air Batteries. *Electrochem. commun.* **2009**, *11*, 1916–1918.
- (35) Jiang, R. Combinatorial Electrochemical Cell Array for High Throughput Screening of Micro-Fuel-Cells and Metal/air Batteries. *Rev. Sci. Instrum.* **2007**, *78*, 072209.
- (36) Abraham, K. M.; Jiang, Z. A Polymer Electrolyte-Based Rechargeable Lithium/Oxygen Battery. *J. Electrochem. Soc.* **1996**, *143*, 1–5.
- (37) Toni, J. E. A.; McDonald, G. D.; Elliott, W. E. *Lithium-Moist Air Battery*; Fort Belvoir, Virginia, 1966.
- (38) Blurton, K. F.; Sammells, A. F. Metal/air Review Batteries: Their Status and Potential - a Review. *J. Power Sources* **1979**, *4*, 263–279.
- (39) Semkow, K. W.; Sammells, A. F. A Lithium Oxygen Secondary Battery. *J. Electrochem. Soc.* **1987**, *134*, 2084–2085.
- (40) Abraham, K. M. A Brief History of Non-Aqueous Metal–Air Batteries. *ECS Trans.* **2008**, *3*, 67–71.
- (41) Zhang, T.; Zhou, H. A Reversible Long-Life Lithium–Air Battery in Ambient Air. *Nat. Commun.* **2013**, *4*, 1817.
- (42) Adams, B. D.; Radtke, C.; Black, R.; Trudeau, M. L.; Zaghbi, K.; Nazar, L. F. Current Density Dependence of Peroxide Formation in the Li–O<sub>2</sub> Battery and Its Effect on Charge. *Energy Environ. Sci.* **2013**, *6*, 1772.

- (43) Mitchell, R. R.; Gallant, B. M.; Thompson, C. V.; Shao-Horn, Y. All-Carbon-Nanofiber Electrodes for High-Energy Rechargeable Li-O<sub>2</sub> Batteries. *Energy Environ. Sci.* **2011**, *4*, 2952–2958.
- (44) Lu, Y. C.; Kwabi, D. G.; Yao, K. P. C.; Harding, J. R.; Zhou, J.; Zuin, L.; Shao-Horn, Y. The Discharge Rate Capability of Rechargeable Li-O<sub>2</sub> Batteries. *Energy Environ. Sci.* **2011**, *4*, 2999–3007.
- (45) Ottakam Thotiyl, M. M.; Freunberger, S. a.; Peng, Z.; Chen, Y.; Liu, Z.; Bruce, P. G. A Stable Cathode for the Aprotic Li–O<sub>2</sub> Battery. *Nat. Mater.* **2013**, *12*, 1–7.
- (46) Kim, B. G.; Kim, H.-J.; Back, S.; Nam, K. W.; Jung, Y.; Han, Y.-K.; Choi, J. W. Improved Reversibility in Lithium-Oxygen Battery: Understanding Elementary Reactions and Surface Charge Engineering of Metal Alloy Catalyst. *Sci. Rep.* **2014**, *4*, 18–21.
- (47) Lu, J.; Lei, Y.; Lau, K. C.; Luo, X.; Du, P.; Wen, J.; Assary, R. S.; Das, U.; Miller, D. J.; Elam, J. W.; et al. A Nanostructured Cathode Architecture for Low Charge Overpotential in Lithium-Oxygen Batteries. *Nat. Commun.* **2013**, *4*, 2383.
- (48) Yilmaz, E.; Yogi, C.; Yamanaka, K.; Ohta, T.; Byon, H. R. Promoting Formation of Noncrystalline Li<sub>2</sub>O<sub>2</sub> in Li-O<sub>2</sub> Battery with RuO<sub>2</sub> Nanoparticles. *Nano Lett.* **2013**, *13*, 4679–4684.
- (49) Meini, S.; Piana, M.; Tsiouvaras, N.; Garsuch, A.; Gasteiger, H. a. The Effect of Water on the Discharge Capacity of a Non-Catalyzed Carbon Cathode for Li-O<sub>2</sub> Batteries. *Electrochem. Solid-State Lett.* **2012**, *15*, A45.
- (50) Meini, S.; Solchenbach, S.; Piana, M.; Gasteiger, H. a. The Role of Electrolyte Solvent Stability and Electrolyte Impurities in the Electrooxidation of Li<sub>2</sub>O<sub>2</sub> in Li-O<sub>2</sub> Batteries. *J. Electrochem. Soc.* **2014**, *161*, A1306–A1314.
- (51) Aetukuri, N. B.; McCloskey, B. D.; García, J. M.; Krupp, L. E.; Viswanathan, V.; Luntz, A. C. On the Origin and Implications of Li<sub>2</sub>O<sub>2</sub> Toroid Formation in Nonaqueous Li-O<sub>2</sub> Batteries. arXiv:1406.3335v1.
- (52) Mitchell, R. R.; Gallant, B. M.; Shao-Horn, Y.; Thompson, C. V. Mechanisms of Morphological Evolution of Li<sub>2</sub>O<sub>2</sub> Particles during Electrochemical Growth. *J. Phys. Chem. Lett.* **2013**, *4*, 1060–1064.
- (53) Viswanathan, V.; Thygesen, K. S.; Hummelshøj, J. S.; Nørskov, J. K.; Girishkumar, G.; McCloskey, B. D.; Luntz, A. C. Electrical Conductivity in Li<sub>2</sub>O<sub>2</sub> and Its Role in Determining Capacity Limitations in Non-Aqueous Li-O<sub>2</sub> Batteries. *J. Chem. Phys.* **2011**, *135*, 214704.

- (54) Jung, H.-G.; Kim, H.-S.; Park, J.-B.; Oh, I.-H.; Hassoun, J.; Yoon, C. S.; Scrosati, B.; Sun, Y.-K. A Transmission Electron Microscopy Study of the Electrochemical Process of Lithium-Oxygen Cells. *Nano Lett.* **2012**, *1*, 2–4.
- (55) Zhai, D.; Wang, H.-H.; Yang, J.; Lau, K. C.; Li, K.; Amine, K.; Curtiss, L. a. Disproportionation in Li-O<sub>2</sub> Batteries Based on a Large Surface Area Carbon Cathode. *J. Am. Chem. Soc.* **2013**, *135*, 15364–15372.
- (56) Xia, C.; Waletzko, M.; Chen, L.; Pepler, K.; Klar, P. J.; Janek, J. Evolution of Li<sub>2</sub>O<sub>2</sub> Growth and Its Effect on Kinetics of Li-O<sub>2</sub> Batteries. *ACS Appl. Mater. Interfaces* **2014**, *6*, 12083–12092.
- (57) Kosma, V. a.; Beltsios, K. G. Simple Solution Routes for Targeted Carbonate Phases and Intricate Carbonate and Silicate Morphologies. *Mater. Sci. Eng. C* **2013**, *33*, 289–297.
- (58) Felker, F. C.; Kenar, J. A.; Fanta, G. F.; Biswas, A. Comparison of Microwave Processing and Excess Steam Jet Cooking for Spherulite Production from Amylose–fatty Acid Inclusion Complexes. *Starch* **2013**, *65*, 864–874.
- (59) Horstmann, B.; Gallant, B.; Mitchell, R.; Bessler, W. G.; Shao-horn, Y.; Bazant, M. Z. Rate-Dependent Morphology of Li<sub>2</sub>O<sub>2</sub> Growth in Li-O<sub>2</sub> Batteries. *J. Phys. Chem. Lett.* **2013**, *4*, 4217–4222.
- (60) Griffith, L. D.; Sleightholme, A. E. S.; Mansfield, J. F.; Siegel, D. J.; Monroe, C. W. In Preparation.
- (61) Morse, J. W.; Casey, W. H. Ostwald Processes and Mineral Paragenesis in Sediments. *Am. J. Sci.* **1988**, *288*, 537–560.
- (62) Feenstra, T. P.; Bruyn, P. L. De. The Ostwald Rule of Stages in Precipitation from Highly Supersaturated Solutions: A Model and Its Application to the Formation of the Nonstoichiometric Amorphous Calcium Phosphate Precursor Phase. *J. Colloid Interface Sci.* **1981**, *84*, 66–72.
- (63) Ostwald, W. Studien Über Die Umwandlung Fester Körper. *Z. Phys. Chem.* **1897**, *22*, 289–330.
- (64) Tian, F.; Radin, M. D.; Siegel, D. J. Enhanced Charge Transport in Amorphous Li<sub>2</sub>O<sub>2</sub>. *Chem. Mater.* **2014**, *26*, 2952–2959.
- (65) Lau, K. C.; Lu, J.; Luo, X.; Curtiss, L. a.; Amine, K. Implications of the Unpaired Spins in Li-O<sub>2</sub> Battery Chemistry and Electrochemistry: A Minireview. *Chempluschem* **2014**, DOI:10.1002/cplu.201402053.
- (66) Vannerberg, N.-G. Peroxides, Superoxides, and Ozonides of the Metals of Groups Ia, IIa, and IIb. In *Progress in Inorganic Chemistry*; John Wiley & Sons, Inc., 1962; pp. 125–197.

- (67) Lu, J.; Jung, H.-J.; Lau, K. C.; Zhang, Z.; Schlueter, J. a; Du, P.; Assary, R. S.; Greeley, J.; Ferguson, G. a; Wang, H.-H.; et al. Magnetism in Lithium-Oxygen Discharge Product. *ChemSusChem* **2013**, *6*, 1196–1202.
- (68) Radin, M. D.; Rodriguez, J. F.; Tian, F.; Siegel, D. J. Lithium Peroxide Surfaces Are Metallic, While Lithium Oxide Surfaces Are Not. *J. Am. Chem. Soc.* **2012**, *134*, 1093–1103.
- (69) Ong, S. P.; Mo, Y.; Ceder, G. Low Hole Polaron Migration Barrier in Lithium Peroxide. *Phys. Rev. B* **2012**, *85*, 081105.
- (70) Radin, M. D.; Siegel, D. J. Charge Transport in Lithium Peroxide: Relevance for Rechargeable Metal-Air Batteries. *Energy Environ. Sci.* **2013**, *6*, 2370–2379.
- (71) McCloskey, B. D.; Valery, A.; Luntz, A. C.; Gowda, S. R.; Wallra, G. M.; Garcia, J. M.; Mori, T.; Krupp, L. E. Combining Accurate O<sub>2</sub> and Li<sub>2</sub>O<sub>2</sub> Assays to Separate Discharge and Charge Stability Limitations in Nonaqueous Li-O<sub>2</sub> Batteries. *J. Phys. Chem. Lett.* **2013**, *4*, 2989–2993.
- (72) Freunberger, S. a; Chen, Y.; Drewett, N. E.; Hardwick, L. J.; Bardé, F.; Bruce, P. G. The Lithium-Oxygen Battery with Ether-Based Electrolytes. *Angew. Chem. Int. Ed. Engl.* **2011**, *50*, 8609–8613.
- (73) Luntz, A. C.; Viswanathan, V.; Voss, J.; Varley, J. B.; Speidel, A. Tunneling and Polaron Charge Transport through Li<sub>2</sub>O<sub>2</sub> in Li-O<sub>2</sub> Batteries. *J. Phys. Chem. Lett.* **2013**, 2–7.
- (74) Garcia-Lastra, J. M.; Myrdal, J. S. G.; Christensen, R.; Thygesen, K. S.; Vegge, T. DFT+U Study of Polaronic Conduction in Li<sub>2</sub>O<sub>2</sub> and Li<sub>2</sub>CO<sub>3</sub>: Implications for Li-Air Batteries. *J. Phys. Chem. C* **2013**, *117*, 5568–5577.
- (75) Kang, S.; Mo, Y.; Ong, S. P.; Ceder, G. A Facile Mechanism for Recharging Li<sub>2</sub>O<sub>2</sub> in Li-O<sub>2</sub> Batteries. *Chem. Mater.* **2013**, *25*, 3328–3336.
- (76) Malik, R.; Abdellahi, A.; Ceder, G. A Critical Review of the Li Insertion Mechanisms in LiFePO<sub>4</sub> Electrodes. *J. Electrochem. Soc.* **2013**, *160*, A3179–A3197.
- (77) Albertus, P.; Girishkumar, G.; McCloskey, B.; Sánchez-Carrera, R. S.; Kozinsky, B.; Christensen, J.; Luntz, a. C. Identifying Capacity Limitations in the Li/Oxygen Battery Using Experiments and Modeling. *J. Electrochem. Soc.* **2011**, *158*, A343.
- (78) Das, S. K.; Xu, S.; Emwas, A.-H.; Lu, Y. Y.; Srivastava, S.; Archer, L. a. High Energy Lithium-Oxygen Batteries - Transport Barriers and Thermodynamics. *Energy Environ. Sci.* **2012**, *5*, 8927.
- (79) Lu, Y.-C.; Shao-Horn, Y. Probing the Reaction Kinetics of the Charge Reactions of Nonaqueous Li-O<sub>2</sub> Batteries. *J. Phys. Chem. Lett.* **2013**, *4*, 93–99.

- (80) Viswanathan, V.; Nørskov, J. K.; Speidel, A.; Scheffler, R.; Gowda, S.; Luntz, A. C. Li-O<sub>2</sub> Kinetic Overpotentials: Tafel Plots from Experiment and First-Principles Theory. *J. Phys. Chem. Lett.* **2013**, *4*, 556–560.
- (81) Gerbig, O.; Merkle, R.; Maier, J. Electron and Ion Transport In Li<sub>2</sub>O<sub>2</sub>. *Adv. Mater.* **2013**, *25*, 3129–3133.
- (82) Radin, M. D.; Tian, F.; Siegel, D. J. Electronic Structure of Li<sub>2</sub>O<sub>2</sub> {0001} Surfaces. *J. Mater. Sci.* **2012**, *47*, 7564–7570.
- (83) Geng, W. T.; He, B. L.; Ohno, T. Grain Boundary Induced Conductivity in Li<sub>2</sub>O<sub>2</sub>. *J. Phys. Chem. C* **2013**, *117*, 25222–25228.
- (84) Zhao, Y.; Ban, C.; Kang, J.; Santhanagopalan, S.; Kim, G.-H.; Wei, S.-H.; Dillon, A. C. P-Type Doping of Lithium Peroxide with Carbon Sheets. *Appl. Phys. Lett.* **2012**, *101*, 023903.
- (85) Zhu, D.; Zhang, L.; Song, M.; Wang, X.; Mi, R.; Liu, H.; Mei, J.; Lau, L. W. M.; Chen, Y. Intermittent Operation of the Aprotic Li-O<sub>2</sub> Battery: The Mass Recovery Process upon Discharge Interval. *J. Solid State Electrochem.* **2013**, *17*, 2539–2544.
- (86) Sahapatombut, U.; Cheng, H.; Scott, K. Modelling the Micro–macro Homogeneous Cycling Behaviour of a Lithium–air Battery. *J. Power Sources* **2013**, *227*, 243–253.
- (87) Nimon, V. Y.; Visco, S. J.; De Jonghe, L. C.; Volfkovich, Y. M.; Bograchev, D. a. Modeling and Experimental Study of Porous Carbon Cathodes in Li-O<sub>2</sub> Cells with Non-Aqueous Electrolyte. *ECS Electrochem. Lett.* **2013**, *2*, A33–A35.
- (88) Liu, J.; Monroe, C. W. In Preparation.
- (89) Hummelshøj, J. S.; Luntz, a C.; Nørskov, J. K. Theoretical Evidence for Low Kinetic Overpotentials in Li-O<sub>2</sub> Electrochemistry. *J. Chem. Phys.* **2013**, *138*, 034703.
- (90) Mo, Y.; Ong, S.; Ceder, G. First-Principles Study of the Oxygen Evolution Reaction of Lithium Peroxide in the Lithium-Air Battery. *Phys. Rev. B* **2011**, *84*, 205446.
- (91) Lee, B.; Seo, D.-H.; Lim, H.-D.; Park, I.; Park, K.-Y.; Kim, J.; Kang, K. First-Principles Study of the Reaction Mechanism in Sodium–Oxygen Batteries. *Chem. Mater.* **2014**, *26*, 1048–1055.
- (92) Leung, K. Electronic Structure Modeling of Electrochemical Reactions at Electrode/Electrolyte Interfaces in Lithium Ion Batteries. *J. Phys. Chem. C* **2013**, *117*, 1539–1547.
- (93) Mizuno, F.; Nakanishi, S.; Kotani, Y.; Yokoishi, S.; Iba, H. Rechargeable Li-Air Batteries with Carbonate-Based Liquid Electrolytes. *Electrochemistry* **2010**, *78*, 403–405.

- (94) McCloskey, B.; Bethune, D.; Shelby, R.; Girishkumar, G.; Luntz, A. Solvents' Critical Role in Nonaqueous Lithium-Oxygen Battery. *J. Phys. Chem. Lett.* **2011**, *2*, 1161–1166.
- (95) Laino, T.; Curioni, A. A New Piece in the Puzzle of Lithium/Air Batteries: Computational Study on the Chemical Stability of Propylene Carbonate in the Presence of Lithium Peroxide. *Chem. - Eur. J.* **2012**, *18*, 3510–3520.
- (96) Veith, G. M.; Nanda, J.; Delmau, L. H.; Dudney, N. J. Influence of Lithium Salts on the Discharge Chemistry of Li-Air Cells. *J. Phys. Chem. Lett.* **2012**, *3*, 1242–1247.
- (97) Du, P.; Lu, J.; Lau, K. C.; Luo, X.; Bareño, J.; Zhang, X.; Ren, Y.; Zhang, Z.; Curtiss, L. a; Sun, Y.-K.; et al. Compatibility of Lithium Salts with Solvent of the Non-Aqueous Electrolyte in Li-O<sub>2</sub> Batteries. *Phys. Chem. Chem. Phys.* **2013**, *15*, 5572–5581.
- (98) Younesi, R.; Hahlin, M.; Bjo, F.; Johansson, P.; Edstro, K. Li-O<sub>2</sub> Battery Degradation by Lithium Peroxide (Li<sub>2</sub>O<sub>2</sub>): A Model Study. *Chem. Mater.* **2013**, *25*, 77–84.
- (99) McCloskey, B. D.; Speidel, A.; Scheffler, R.; Miller, D. C.; Viswanathan, V.; Hummelshøj, J. S.; Nørskov, J. K.; Luntz, A. C. Twin Problems of Interfacial Carbonate Formation in Nonaqueous Li-O<sub>2</sub> Batteries. *J. Phys. Chem. Lett.* **2012**, *3*, 997–1001.
- (100) Peng, Z.; Freunberger, S. a; Chen, Y.; Bruce, P. G. A Reversible and Higher-Rate Li-O<sub>2</sub> Battery. *Science (80-. )*. **2012**, *337*, 563–566.
- (101) Lau, K. C.; Lu, J.; Low, J.; Peng, D.; Wu, H.; Albishri, H. M.; Al-Hady, D. A.; Curtiss, L. a.; Amine, K. Investigation of the Decomposition Mechanism of Lithium Bis(oxalate)borate (LiBOB) Salt in the Electrolyte of an Aprotic Li-O<sub>2</sub> Battery. *Energy Technol.* **2014**, *2*, 348–354.
- (102) Bryantsev, V. Computational Study of the Mechanisms of Superoxide-Induced Decomposition of Organic Carbonate-Based Electrolytes. *J. Phys. Chem. Lett.* **2011**, *2*, 379–383.
- (103) Beyer, H.; Meini, S.; Tsiouvaras, N.; Piana, M.; Gasteiger, H. a. Thermal and Electrochemical Decomposition of Lithium Peroxide in Non-Catalyzed Carbon Cathodes for Li-Air Batteries. *Phys. Chem. Chem. Phys.* **2013**, *15*, 11025–11037.
- (104) Bryantsev, V. S.; Faglioni, F. Predicting Autoxidation Stability of Ether- and Amide-Based Electrolyte Solvents for Li-Air Batteries. *J. Phys. Chem. A* **2012**, *116*, 7128–7138.
- (105) Zhu, D.; Zhang, L.; Song, M.; Wang, X.; Mei, J.; Lau, L. W. M.; Chen, Y. Solvent Autoxidation, Electrolyte Decomposition, and Performance Deterioration of the Aprotic Li-O<sub>2</sub> Battery. *J. Solid State Electrochem.* **2013**, *17*, 2865–2870.

- (106) McCloskey, B. D.; Bethune, D. S.; Shelby, R. M.; Mori, T.; Scheffler, R.; Speidel, A.; Sherwood, M.; Luntz, A. C. Limitations in Rechargeability of Li-O<sub>2</sub> Batteries and Possible Origins. *J. Phys. Chem. Lett.* **2012**, *3*, 3043–3047.
- (107) Assary, R. S.; Lau, K. C.; Amine, K.; Sun, Y.; Curtiss, L. A. Interactions of Dimethoxy Ethane with Li<sub>2</sub>O<sub>2</sub> Clusters and Likely Decomposition Mechanisms for Li-O<sub>2</sub> Batteries. *J. Phys. Chem. C* **2013**, *117*, 8041–8049.
- (108) Laino, T.; Curioni, A. Chemical Reactivity of Aprotic Electrolytes on a Solid Li<sub>2</sub>O<sub>2</sub> Surface: Screening Solvents for Li–air Batteries. *New J. Phys.* **2013**, *15*, 095009.
- (109) McCloskey, B.; Scheffler, R.; Speidel, A.; Bethune, D. S.; Shelby, R. M.; Luntz, A. C. On the Efficacy of Electrocatalysis in Nonaqueous Li-O<sub>2</sub> Batteries. *J. Am. Chem. Soc.* **2011**, *133*, 18038–18041.
- (110) Harding, J. R.; Lu, Y.; Shao-horn, Y. Evidence of Catalyzed Oxidation of Li<sub>2</sub>O<sub>2</sub> for Rechargeable Li-Air Battery Applications. *Phys. Chem. Chem. Phys.* **2012**, *14*, 10540–10546.
- (111) Hohenberg, P.; Kohn, W. Inhomogeneous Electron Gas. *Phys. Rev.* **1964**, *136*, B864.
- (112) Ceperley, D.; Alder, B. Ground State of the Electron Gas by a Stochastic Method. *Phys. Rev. Lett.* **1980**, *45*, 566–569.
- (113) Martin, R. M. *Electronic Structure: Basic Theory and Practical Methods*; Cambridge University Press: Cambridge, UK, 2004.
- (114) Perdew, J. P.; Burke, K.; Ernzerhof, M. Generalized Gradient Approximation Made Simple [Phys. Rev. Lett. *77*, 3865 (1996)]. *Phys. Rev. Lett.* **1997**, *78*, 1396–1396.
- (115) Perdew, J.; Ruzsinszky, A.; Csonka, G.; Vydrov, O.; Scuseria, G.; Constantin, L.; Zhou, X.; Burke, K. Restoring the Density-Gradient Expansion for Exchange in Solids and Surfaces. *Phys. Rev. Lett.* **2008**, *100*, 1–4.
- (116) Klimeš, J.; Michaelides, A. Perspective: Advances and Challenges in Treating van Der Waals Dispersion Forces in Density Functional Theory. *J. Chem. Phys.* **2012**, *137*, 120901.
- (117) Mori-Sánchez, P.; Cohen, A.; Yang, W. Localization and Delocalization Errors in Density Functional Theory and Implications for Band-Gap Prediction. *Phys. Rev. Lett.* **2008**, *100*, 146401.
- (118) Cohen, A. J.; Mori-Sánchez, P.; Yang, W. Insights into Current Limitations of Density Functional Theory. *Science* **2008**, *321*, 792–794.

- (119) Heyd, J.; Scuseria, G. E.; Ernzerhof, M. Hybrid Functionals Based on a Screened Coulomb Potential. *J. Chem. Phys.* **2003**, *118*, 8207.
- (120) Krukau, A. V.; Vydrov, O. a.; Izmaylov, A. F.; Scuseria, G. E. Influence of the Exchange Screening Parameter on the Performance of Screened Hybrid Functionals. *J. Chem. Phys.* **2006**, *125*, 224106.
- (121) Perdew, J. P.; Burke, K.; Ernzerhof, M. Generalized Gradient Approximation Made Simple. *Phys. Rev. Lett.* **1996**, *77*, 3865–3868.
- (122) Lambrecht, W. R. L. Which Electronic Structure Method for the Study of Defects: A Commentary. *Phys. Status Solidi B* **2011**, *248*, 1547–1558.
- (123) Alkauskas, A.; Broqvist, P.; Pasquarello, A. Defect Levels Through Hybrid Density Functionals: Insights and Applications. *Phys. Status Solidi B* **2011**, *248*, 775–789.
- (124) Choi, M.; Janotti, A.; Van de Walle, C. G. Native Point Defects and Dangling Bonds in A-Al<sub>2</sub>O<sub>3</sub>. *J. Appl. Phys.* **2013**, *113*, 044501.
- (125) Shishkin, M.; Kresse, G. Self-Consistent GW Calculations for Semiconductors and Insulators. *Phys. Rev. B* **2007**, *75*, 1–9.
- (126) Shishkin, M.; Marsman, M.; Kresse, G. Accurate Quasiparticle Spectra from Self-Consistent GW Calculations with Vertex Corrections. *Phys. Rev. Lett.* **2007**, *99*, 246403.
- (127) Garcia-Lastra, J. M.; Bass, J. D.; Thygesen, K. S. Communication: Strong Excitonic and Vibronic Effects Determine the Optical Properties of Li<sub>2</sub>O<sub>2</sub>. *J. Chem. Phys.* **2011**, *135*, 121101.
- (128) Schimka, L.; Harl, J.; Kresse, G. Improved Hybrid Functional for Solids: The HSEsol Functional. *J. Chem. Phys.* **2011**, *134*, 024116.
- (129) Aulbur, W. G.; Jönsson, L.; Wilkins, J. W. Quasiparticle Calculations in Solids. *Solid State Phys.* **1999**, *54*, 1–218.
- (130) Hedin, L. New Method for Calculating the One-Particle Green's Function with Application to the Electron-Gas Problem. *Phys. Rev.* **1965**, *139*, A796–A823.
- (131) Shishkin, M.; Kresse, G. Implementation and Performance of the Frequency-Dependent GW Method within the PAW Framework. *Phys. Rev. B* **2006**, *74*, 035101.
- (132) Fuchs, F.; Furthmüller, J.; Bechstedt, F.; Shishkin, M.; Kresse, G. Quasiparticle Band Structure Based on a Generalized Kohn-Sham Scheme. *Phys. Rev. B* **2007**, *76*, 1–8.
- (133) Ashcroft, N. W.; Mermin, N. D. *Solid State Physics*; Holt, Rinehart and Winston: New York, 1976.

- (134) Blöchl, P.; Jepsen, O.; Andersen, O. Improved Tetrahedron Method for Brillouin-Zone Integrations. *Phys. Rev. B. Condens. Matter* **1994**, *49*, 16223–16233.
- (135) Troullier, N.; Martins, J. L. Efficient Pseudopotentials for Plane-Wave Calculations. *Phys. Rev. B* **1991**, *43*, 1993.
- (136) Vanderbilt, D. Soft Self-Consistent Pseudopotentials in a Generalized Eigenvalue Formalism. *Phys. Rev. B* **1990**, *41*, 7892.
- (137) Blöchl, P. E. Projector Augmented-Wave Method. *Phys. Rev. B* **1994**, *50*, 17953.
- (138) Kresse, G.; Hafner, J. Ab Initio Molecular-Dynamics Simulation of the Liquid-Metal-Amorphous-Semiconductor Transition in Germanium. *Phys. Rev. B* **1994**, *49*, 14251–14269.
- (139) Kresse, G.; Furthmüller, J. Efficient Iterative Schemes for Ab Initio Total-Energy Calculations Using a Plane-Wave Basis Set. *Phys. Rev. B* **1996**, *54*, 11169–11186.
- (140) Kresse, G.; Furthmüller, J. Efficiency of Ab-Initio Total Energy Calculations for Metals and Semiconductors Using a Plane-Wave Basis Set. *Comput. Mater. Sci.* **1996**, *6*, 15–50.
- (141) Kresse, G.; Hafner, J. Ab Initio Molecular Dynamics for Liquid Metals. *Phys. Rev. B* **1993**, *47*, 558–561.
- (142) Monkhorst, H.; Pack, J. Special Points for Brillouin-Zone Integrations. *Phys. Rev. B* **1976**, *13*, 5188–5192.
- (143) Momma, K.; Izumi, F. VESTA: A Three-Dimensional Visualization System for Electronic and Structural Analysis. *J. Appl. Crystallogr.* **2008**, *41*, 653–658.
- (144) Kudo, T.; Fueki, K. *Solid State Ionics*; Kodansha VCH: Tokyo, Japan Weinheim, F.R.G. New York, NY, USA, 1990.
- (145) Tilley, R. J. D. *Defects in Solids*; John Wiley & Sons, Inc., 2008.
- (146) Kröger, F. A. *The Chemistry of Imperfect Crystals.*; North-Holland Pub. Co.; American Elsevier: Amsterdam, New York, 1973.
- (147) Payne, M. C.; Makov, G. Periodic Boundary Conditions in Ab Initio Calculations. *Phys. Rev. B* **1995**, *51*, 4014–4022.
- (148) Komsa, H.-P.; Rantala, T.; Pasquarello, A. Finite-Size Supercell Correction Schemes for Charged Defect Calculations. *Phys. Rev. B* **2012**, *86*, 045112.

- (149) Taylor, S. E.; Bruneval, F. Understanding and Correcting the Spurious Interactions in Charged Supercells. *Phys. Rev. B* **2011**, *84*, 075155.
- (150) Wang, L.; Maxisch, T.; Ceder, G. Oxidation Energies of Transition Metal Oxides within the GGA+U Framework. *Phys. Rev. B* **2006**, *73*, 195107.
- (151) Kurth, S.; Perdew, J. P.; Blaha, P. Molecular and Solid-State Tests of Density Functional Approximations: LSD, GGAs, and Meta-GGAs. *Int. J. Quantum Chem.* **1999**, *75*, 889.
- (152) Sholl, D. S.; Steckel, J. A. *Density Functional Theory: A Practical Introduction*; Wiley: Hoboken, N.J., 2009.
- (153) Jónsson, H.; Mills, G.; Jacobsen, K. W. Nudged Elastic Band Method for Finding Minimum Energy Paths of Transitions. In *Classical And Quantum Dynamics In Condensed Phase Simulations*; Berne, B. J.; Ciccotti, G.; Coker, D. F., Eds.; World Scientific, 1998; pp. 385–404.
- (154) Königstein, M. Structural Properties of Nonstoichiometric Barium and Strontium Peroxides: BaO<sub>2-x</sub> (1.97≥2-x≥1.72) and SrO<sub>2-x</sub> (1.98≥2-x≥1.90). *J. Solid State Chem.* **1999**, *147*, 478–484.
- (155) Roth, R. S.; Rawn, C. J.; Hill, M. D. Synthesis and Characterization of Phases in the System Ba-Au-Ag-O<sub>2</sub>. *NIST Spec. Publ.* **1991**, *804*, 225–236.
- (156) Kang, J.; Jung, Y. S.; Wei, S.-H.; Dillon, A. Implications of the Formation of Small Polarons in Li<sub>2</sub>O<sub>2</sub> for Li-Air Batteries. *Phys. Rev. B* **2012**, *85*, 035210.
- (157) Timoshevskii, V.; Feng, Z.; Bevan, K. H.; Goodenough, J.; Zaghbi, K. Improving Li<sub>2</sub>O<sub>2</sub> Conductivity via Polaron Preemption: An Ab Initio Study of Si Doping. *Appl. Phys. Lett.* **2013**, *103*, 073901.
- (158) Hummelshøj, J. S.; Blomqvist, J.; Datta, S.; Vegge, T.; Rossmeisl, J.; Thygesen, K. S.; Luntz, A. C.; Jacobsen, K. W.; Nørskov, J. K. Communications: Elementary Oxygen Electrode Reactions in the Aprotic Li-Air Battery. *J. Chem. Phys.* **2010**, *132*, 071101.
- (159) Xu, W.; Viswanathan, V. V.; Wang, D.; Towne, S. a.; Xiao, J.; Nie, Z.; Hu, D.; Zhang, J.-G. Investigation on the Charging Process of Li<sub>2</sub>O<sub>2</sub>-Based Air Electrodes in Li-O<sub>2</sub> Batteries with Organic Carbonate Electrolytes. *J. Power Sources* **2011**, *196*, 3894–3899.
- (160) Song, M.; Zhu, D.; Zhang, L.; Wang, X.; Huang, L.; Shi, Q.; Mi, R.; Liu, H.; Mei, J.; Lau, L. W. M.; et al. Temperature Dependence of Charging Characteristic of C-Free Li<sub>2</sub>O<sub>2</sub> Cathode in Li-O<sub>2</sub> Battery. *J. Solid State Electrochem.* **2013**, *17*, 2061–2069.
- (161) Anandan, V.; Kudla, R.; Drews, A.; Adams, J.; Karulkar, M. Mixed Metal Oxide Catalysts for Rechargeable Lithium-Air Batteries. *ECS Trans.* **2012**, *41*, 167–174.

- (162) Pacchioni, G. Modeling Doped and Defective Oxides in Catalysis with Density Functional Theory Methods: Room for Improvements. *J. Chem. Phys.* **2008**, *128*, 182505.
- (163) Sproul, a. B.; Green, M. a. Improved Value for the Silicon Intrinsic Carrier Concentration from 275 to 375 K. *J. Appl. Phys.* **1991**, *70*, 846.
- (164) Van de Walle, C. G.; Neugebauer, J. First-Principles Calculations for Defects and Impurities: Applications to III-Nitrides. *J. Appl. Phys.* **2004**, *95*, 3851.
- (165) Chen, J.; Hummelshøj, J. S.; Thygesen, K. S.; Myrdal, J. S. G.; Nørskov, J. K.; Vegge, T. The Role of Transition Metal Interfaces on the Electronic Transport in Lithium-Air Batteries. *Catal. Today* **2011**, *165*, 2–9.
- (166) Delacourt, C.; Laffont, L.; Bouchet, R.; Wurm, C.; Leriche, J.-B.; Morcrette, M.; Tarascon, J.-M.; Masquelier, C. Toward Understanding of Electrical Limitations (Electronic, Ionic) in LiMPO<sub>4</sub> (M=Fe, Mn) Electrode Materials. *J. Electrochem. Soc.* **2005**, *152*, A913.
- (167) Serway, R. A.; Jewett, J. W. *Principles of Physics: A Calculus-Based Text*; Brooks/Cole, Cengage Learning: Boston, MA, 2013.
- (168) Capsoni, D.; Bini, M.; Ferrari, S.; Quartarone, E.; Mustarelli, P. Recent Advances in the Development of Li-Air Batteries. *J. Power Sources* **2012**, *220*, 253–263.
- (169) Hardwick, L. J.; Bruce, P. G. The Pursuit of Rechargeable Non-Aqueous Lithium-Oxygen Battery Cathodes. *Curr. Opin. Solid State Mater. Sci.* **2012**, *16*, 178–185.
- (170) Ramprasad, R.; Zhu, H.; Rinke, P.; Scheffler, M. New Perspective on Formation Energies and Energy Levels of Point Defects in Nonmetals. *Phys. Rev. Lett.* **2012**, *108*, 1–5.
- (171) Kraytsberg, A.; Ein-Eli, Y. The Impact of Nano-Scaled Materials on Advanced Metal–air Battery Systems. *Nano Energy* **2013**, *2*, 468–480.
- (172) Zhao, X.; Ceresoli, D.; Vanderbilt, D. Structural, Electronic, and Dielectric Properties of Amorphous ZrO<sub>2</sub> from Ab Initio Molecular Dynamics. *Phys. Rev. B* **2005**, *71*, 085107.
- (173) Nosé, S. A Unified Formulation of the Constant Temperature Molecular Dynamics Methods. *J. Chem. Phys.* **1984**, *81*, 511.
- (174) Ferapontov, Y. a.; Kokoreva, N. V.; Kozlova, N. P.; Ul'yanova, M. a. Thermal Analysis of Lithium Peroxide Prepared by Various Methods. *Russ. J. Gen. Chem.* **2009**, *79*, 891–894.
- (175) Chan, M. K. Y.; Shirley, E. L.; Karan, N. K.; Balasubramanian, M.; Ren, Y.; Greeley, J. P.; Fister, T. T. Structure of Lithium Peroxide. *J. Phys. Chem. Lett.* **2011**, 2483–2486.

- (176) McCloskey, B.; Scheffler, R.; Speidel, A.; Girishkumar, G.; Luntz, A. C. On the Mechanism of Non-Aqueous Li-O<sub>2</sub> Electrochemistry on C and Its Kinetic Overpotentials: Some Implications for Li-Air Batteries. *J. Phys. Chem. C* **2012**, *116*, 23897–23905.
- (177) Schirmacher, W. Theory of Diffusion and Ionic Conduction in Glass. *Solid State Ionics* **1988**, *28-30*, 129–133.
- (178) Haus, J.; Kehr, K. Diffusion in Regular and Disordered Lattices. *Phys. Rep.* **1987**, *150*, 263–406.
- (179) *Engineering Statistics Handbook*; NIST: Gaithersburg, MD, 2003.
- (180) Lorenz, C.; Ziff, R. Precise Determination of the Bond Percolation Thresholds and Finite-Size Scaling Corrections for the Sc, Fcc, and Bcc Lattices. *Phys. Rev. E* **1998**, *57*, 230–236.
- (181) Li, F.; Zhang, T.; Zhou, H. Challenges of Non-Aqueous Li–O<sub>2</sub> Batteries: Electrolytes, Catalysts, and Anodes. *Energy Environ. Sci.* **2013**, *6*, 1125–1141.
- (182) Meini, S.; Tsiouvaras, N.; Schwenke, K. U.; Piana, M.; Beyer, H.; Lange, L.; Gasteiger, H. a. Rechargeability of Li–air Cathodes Pre-Filled with Discharge Products Using an Ether-Based Electrolyte Solution: Implications for Cycle-Life of Li–air Cells. *Phys. Chem. Chem. Phys.* **2013**, *15*, 11478–11493.
- (183) Black, R.; Lee, J.-H.; Adams, B.; Mims, C. a; Nazar, L. F. The Role of Catalysts and Peroxide Oxidation in Lithium-Oxygen Batteries. *Angew. Chem., Int. Ed. Engl.* **2013**, *52*, 392–396.
- (184) Garcia-Araez, N.; Novák, P. Critical Aspects in the Development of Lithium–air Batteries. *J. Solid State Electrochem.* **2013**, *17*, 1793–1807.
- (185) Oh, S.; Black, R.; Pomerantseva, E.; Lee, J.; Nazar, L. Synthesis of a Metallic Mesoporous Pyrochlore as a Catalyst for lithium–O<sub>2</sub> Batteries. *Nat. Chem.* **2012**, *4*, 1004–1010.
- (186) Xu, J.-J.; Wang, Z.-L.; Xu, D.; Zhang, L.-L.; Zhang, X.-B. Tailoring Deposition and Morphology of Discharge Products towards High-Rate and Long-Life Lithium-Oxygen Batteries. *Nat. Commun.* **2013**, *4*, 1–10.
- (187) Xia, C.; Waletzko, M.; Pepler, K.; Janek, J. Silica Nanoparticles as Structural Promoters for Oxygen Cathodes of Lithium–Oxygen Batteries. *J. Phys. Chem. C* **2013**, *117*, 19897–19904.
- (188) Cui, Y.; Wen, Z.; Sun, S.; Lu, Y.; Jin, J. Mesoporous Co<sub>3</sub>O<sub>4</sub> with Different Porosities as Catalysts for the Lithium–oxygen Cell. *Solid State Ionics* **2012**, *225*, 598–603.

- (189) Riaz, A.; Jung, K.-N.; Chang, W.; Lee, S.-B.; Lim, T.-H.; Park, S.-J.; Song, R.-H.; Yoon, S.; Shin, K.-H.; Lee, J.-W. Carbon-Free Cobalt Oxide Cathodes with Tunable Nanoarchitectures for Rechargeable Lithium-Oxygen Batteries. *Chem. Commun. (Camb)*. **2013**, *49*, 5984–5986.
- (190) Giordani, V.; Freunberger, S. a.; Bruce, P. G.; Tarascon, J.-M.; Larcher, D. H<sub>2</sub>O<sub>2</sub> Decomposition Reaction as Selecting Tool for Catalysts in Li–O<sub>2</sub> Cells. *Electrochem. Solid-State Lett.* **2010**, *13*, A180.
- (191) Ryu, W.; Yoon, T.; Song, S. H.; Jeon, S.; Park, Y.; Kim, I. Bifunctional Composite Catalysts Using Co<sub>3</sub>O<sub>4</sub> Nano Fibers Immobilized on Nonoxidized Graphene Nanoflakes for High-Capacity and Long-Cycle Li–O<sub>2</sub> Batteries. *Nano Lett.* **2013**, *13*, 4190–4197.
- (192) Cui, Y.; Wen, Z.; Liu, Y. A Free-Standing-Type Design for Cathodes of Rechargeable Li–O<sub>2</sub> Batteries. *Energy Environ. Sci.* **2011**, *4*, 4727–4734.
- (193) Zhang, K.; Zhang, L.; Chen, X.; He, X.; Wang, X.; Dong, S.; Han, P.; Zhang, C.; Wang, S.; Gu, L.; et al. Mesoporous Cobalt Molybdenum Nitride: A Highly Active Bifunctional Electrocatalyst and Its Application in Lithium-O<sub>2</sub> Batteries. *J. Phys. Chem. C* **2013**, *117*, 858–865.
- (194) Sun, B.; Zhang, J.; Munroe, P.; Ahn, H.-J.; Wang, G. Hierarchical NiCo<sub>2</sub>O<sub>4</sub> Nanorods as an Efficient Cathode Catalyst for Rechargeable Non-Aqueous Li–O<sub>2</sub> Batteries. *Electrochem. Commun.* **2013**, *31*, 88–91.
- (195) Trahey, L.; Karan, N. K.; Chan, M. K. Y.; Lu, J.; Ren, Y.; Greeley, J.; Balasubramanian, M.; Burrell, A. K.; Curtiss, L. a.; Thackeray, M. M. Synthesis, Characterization, and Structural Modeling of High-Capacity, Dual Functioning MnO<sub>2</sub> Electrode/Electrocatalysts for Li–O<sub>2</sub> Cells. *Adv. Energy Mater.* **2012**, *3*, 75–84.
- (196) Thackeray, M. M.; Chan, M. K. Y.; Trahey, L.; Kirklin, S.; Wolverton, C. Vision for Designing High-Energy, Hybrid Li Ion/Li–O<sub>2</sub> Cells. *J. Phys. Chem. Lett.* **2013**, *4*, 3607–3611.
- (197) Gamburg, Y. D.; Zangari, G. *Theory and Practice of Metal Electrodeposition*; Springer Science+Business Media, LLC: New York, NY, 2011.
- (198) Zhang, S. S. A Review on Electrolyte Additives for Lithium-Ion Batteries. *J. Power Sources* **2006**, *162*, 1379–1394.
- (199) Sun, B.; Munroe, P.; Wang, G. Ruthenium Nanocrystals as Cathode Catalysts for Lithium-Oxygen Batteries with a Superior Performance. *Sci. Rep.* **2013**, *3*, 2247.
- (200) Wang, M.; Navrotsky, A. LiMO<sub>2</sub> (M=Mn, Fe, and Co): Energetics, Polymorphism and Phase Transformation. *J. Solid State Chem.* **2005**, *178*, 1230–1240.

- (201) Chevrier, V. L.; Ong, S. P.; Armiento, R.; Chan, M. K. Y.; Ceder, G. Hybrid Density Functional Calculations of Redox Potentials and Formation Energies of Transition Metal Compounds. *Phys. Rev. B* **2010**, *82*, 075122.
- (202) *CRC Handbook of Chemistry and Physics*; Haynes, W. M., Ed.; 93rd ed.; CRC Press: Cleveland, Ohio, 2013.
- (203) Colinge, J.-P.; Colinge, C. A. *Physics of Semiconductor Devices*; Kluwer Academic: Boston, 2002.
- (204) Willock, D. J. *Molecular Symmetry*; John Wiley & Sons: Chichester, UK, 2009.
- (205) Radin, M. D.; Rodriguez, J. F.; Siegel, D. J. Lithium Peroxide Surfaces and Point Defects: Relevance for Li-Air Batteries. In *Proceedings of the Battery Congress*; Uddin, M. N., Ed.; 2011.
- (206) Gallant, B. M.; Kwabi, D. G.; Mitchell, R. R.; Zhou, J.; Thompson, C. V.; Shao-Horn, Y. Influence of Li<sub>2</sub>O<sub>2</sub> Morphology on Oxygen Reduction and Evolution Kinetics in Li-O<sub>2</sub> Batteries. *Energy Environ. Sci.* **2013**, *6*, 2518.
- (207) Khan, A. U.; Mahanti, S. D. Collective Electron Effects of O<sub>2</sub><sup>-</sup> in Potassium Superoxide. *J. Chem. Phys.* **1975**, *63*, 2271.
- (208) Zhang, L.; Macdonald, D. D. On the Transport of Point Defects in Passive Films. *Electrochim. Acta* **1998**, *43*, 679–691.
- (209) Hoang, K.; Johannes, M. D. First-Principles Studies of the Effects of Impurities on the Ionic and Electronic Conduction in LiFePO<sub>4</sub>. *J. Power Sources* **2012**, *206*, 274–281.
- (210) Meethong, N.; Kao, Y.-H.; Speakman, S. a.; Chiang, Y.-M. Aliovalent Substitutions in Olivine Lithium Iron Phosphate and Impact on Structure and Properties. *Adv. Funct. Mater.* **2009**, *19*, 1060–1070.
- (211) Varley, J. B.; Viswanathan, V.; Nørskov, J. K.; Luntz, a. C. Lithium and Oxygen Vacancies and Their Role in Li<sub>2</sub>O<sub>2</sub> Charge Transport in Li-O<sub>2</sub> Batteries. *Energy Environ. Sci.* **2014**, *7*, 720–727.
- (212) Seriani, N. Ab Initio Thermodynamics of Lithium Oxides: From Bulk Phases to Nanoparticles. *Nanotechnology* **2009**, *20*, 445703.
- (213) Reuter, K.; Scheffler, M. Composition, Structure, and Stability of RuO<sub>2</sub>(110) as a Function of Oxygen Pressure. *Phys. Rev. B* **2001**, *65*, 035406.
- (214) Tasker, P. The Stability of Ionic Crystal Surfaces. *J. Phys. C Solid State Phys.* **1979**, *12*, 4977–4984.
- (215) Noguera, C. Polar Oxide Surfaces. *J. Phys. Condens. Matter* **2000**, *12*, R367–R410.

- (216) Jiang, H.; Shen, Y.-C. Ionization Potentials of Semiconductors from First-Principles. *J. Chem. Phys.* **2013**, *139*, 164114.
- (217) Bard, A. J.; Faulkner, L. R. *Electrochemical Methods: Fundamentals and Applications*; Wiley: New York, 2001.
- (218) Trasatti, S. The Absolute Electrode Potential: An Explanatory Note. *Pure Appl. Chem.* **1986**, *58*, 955–966.
- (219) Gallego, S.; Beltrán, J. I.; Cerdá, J.; Muñoz, M. C. Magnetism and Half-Metallicity at the O Surfaces of Ceramic Oxides. *J. Phys. Condens. Matter* **2005**, *17*, L451–L457.
- (220) Song, M.; Zhu, D.; Zhang, L.; Wang, X.; Mi, R.; Liu, H.; Mei, J.; Lau, L. W. M.; Chen, Y. Temperature Characteristics of Nonaqueous Li–O<sub>2</sub> Batteries. *J. Solid State Electrochem.* **2014**, *18*, 739–745.
- (221) Park, J.-B.; Hassoun, J.; Jung, H.-G.; Kim, H.-S.; Yoon, C. S.; Oh, I.-H.; Scrosati, B.; Sun, Y.-K. Influence of Temperature on Lithium-Oxygen Battery Behavior. *Nano Lett.* **2013**.
- (222) Chadwick, A. V.; Flack, K. W.; Strange, J. H.; Harding, J. Defect Structures and Ionic Transport in Lithium Oxide. *Solid State Ionics* **1988**, *28-30*, 185–188.
- (223) Jacobst, P. W. M.; Vernont, M. L. Defect Energies for Magnesium Oxide and Lithium Oxide. *J. Chem. Soc. Faraday Trans.* **1990**, *86*, 1233–1238.
- (224) Ogasawara, T.; Débart, A.; Holzapfel, M.; Novák, P.; Bruce, P. G. Rechargeable Li<sub>2</sub>O<sub>2</sub> Electrode for Lithium Batteries. *J. Am. Chem. Soc.* **2006**, *128*, 1390–1393.
- (225) Lu, Y.-C.; Gasteiger, H. A.; Parent, M. C.; Chiloyan, V.; Shao-Horn, Y. The Influence of Catalysts on Discharge and Charge Voltages of Rechargeable Li-Oxygen Batteries. *Electrochem. Solid-State Lett.* **2010**, *13*, A69.
- (226) Xu, W.; Xu, K.; Viswanathan, V. V.; Towne, S. A.; Hardy, J. S.; Xiao, J.; Nie, Z.; Hu, D.; Wang, D.; Zhang, J.-G. Reaction Mechanisms for the Limited Reversibility of Li-O<sub>2</sub> Chemistry in Organic Carbonate Electrolytes. *J. Power Sources* **2011**, *196*, 9631–9639.
- (227) Sun, Q.; Yang, Y.; Fu, Z.-W. Electrochemical Properties of Room Temperature Sodium-Air Batteries with Non-Aqueous Electrolyte. *Electrochem. Commun.* **2012**, *16*, 22–25.
- (228) Obrovac, M. N.; Dunlap, R. a.; Sanderson, R. J.; Dahn, J. R. The Electrochemical Displacement Reaction of Lithium with Metal Oxides. *J. Electrochem. Soc.* **2001**, *148*, A576.

- (229) Poizot, P.; Laruelle, S.; Grugnon, S.; Dupont, L.; Tarascon, J. M. Nano-Sized Transition-Metal Oxides as Negative-Electrode Materials for Lithium-Ion Batteries. *Nature* **2000**, *407*, 496–499.
- (230) Cohn, G.; Ein-Eli, Y. Study and Development of Non-Aqueous Silicon-Air Battery. *J. Power Sources* **2010**, *195*, 4963–4970.
- (231) Wu, X.; Vanderbilt, D.; Hamann, D. Systematic Treatment of Displacements, Strains, and Electric Fields in Density-Functional Perturbation Theory. *Phys. Rev. B* **2005**, *72*, 035105.
- (232) Newman, J. S. *Electrochemical Systems*; Prentice Hall international series in the physical and chemical engineering sciences; Prentice Hall: Englewood Cliffs, N.J., 1991.